



**INSTITUTO POTOSINO DE INVESTIGACIÓN
CIENTÍFICA Y TECNOLÓGICA, A.C.**

POSGRADO EN CIENCIAS APLICADAS

**“Synthesis and characterization of doped
single-walled carbon nanotubes and graphitic
nanoribbons”**

Tesis que presenta

Jessica Rosaura Campos Delgado

Para obtener el grado de

Doctora en Ciencias Aplicadas

En la opción de

Nanociencias y Nanotecnología

Codirectores de la Tesis:

Dr. Humberto Terrones Maldonado

Dr. Mauricio Terrones Maldonado

San Luis Potosí, S.L.P., 17 de Diciembre 2009



Constancia de aprobación de la tesis

La tesis "**Synthesis and characterization of doped single-walled carbon nanotubes and graphitic nanoribbons**" presentada para obtener el Grado de Doctora en Ciencias Aplicadas en la opción de Nanociencias y Nanotecnología fue elaborada por **Jessica Rosaura Campos Delgado** y aprobada el **17 de diciembre de 2009** por los suscritos, designados por el Colegio de Profesores de la División de Materiales Avanzados del Instituto Potosino de Investigación Científica y Tecnológica, A.C.

Dr. Mauricio Terrones Maldonado
(Codirector de la tesis)

Dr. Humberto Terrones Maldonado
(Codirector de la tesis)



Créditos Institucionales

Esta tesis fue elaborada en las instalaciones y con la infraestructura de la División de Materiales Avanzados para la Tecnología Moderna del Instituto Potosino de Investigación Científica y Tecnológica, A.C. y el Laboratorio de Investigaciones en Nanociencia y Nanotecnología, bajo la co-dirección de los doctores Humberto Terrones Maldonado y Mauricio Terrones Maldonado.

Durante la realización del trabajo el autor recibió una beca académica del Consejo Nacional de Ciencia y Tecnología (202248).



Instituto Potosino de Investigación Científica y Tecnológica, A.C.

Acta de Examen de Grado

El Secretario Académico del Instituto Potosino de Investigación Científica y Tecnológica, A.C., certifica que en el Acta 030 del Libro Primero de Actas de Exámenes de Grado del Programa de Doctorado en Ciencias Aplicadas en la opción de Nanociencias y Nanotecnología está asentado lo siguiente:

En la ciudad de San Luis Potosí a los 17 días del mes de diciembre del año 2009, se reunió a las 09:00 horas en las instalaciones del Instituto Potosino de Investigación Científica y Tecnológica, A.C., el Jurado integrado por:

Dra. Yadira Itzel Vega Cantú	Presidenta	IPICYT
Dr. Humberto Terrones Maldonado	Secretario	IPICYT
Dr. Bobby Gene Sumpter	Sinodal externo	ORNL
Dr. Mauricio Terrones Maldonado	Sinodal	IPICYT
Dra. Mildred Dresselhaus	Sinodal externo	MIT

a fin de efectuar el examen, que para obtener el Grado de:

DOCTORA EN CIENCIAS APLICADAS
EN LA OPCIÓN DE NANOCIENCIAS Y NANOTECNOLOGÍA

sustenta la C.

Jessica Rosaura Campos Delgado

sobre la Tesis intitulada:

Synthesis and characterization of doped single-walled carbon nanotubes and graphitic nanoribbons

que se desarrolló bajo la dirección de

Dr. Humberto Terrones Maldonado
Dr. Mauricio Terrones Maldonado

El Jurado, después de deliberar, determinó

APROBARLA

Dandose por terminado el acto a las 11:38 horas, procediendo a la firma del Acta los integrantes del Jurado. Dando fe el Secretario Académico del Instituto.

A petición de la interesada y para los fines que a la misma convengan, se extiende el presente documento en la ciudad de San Luis Potosí, S.L.P., México, a los 17 días del mes de diciembre de 2009.

Mtra. Ivonne Lizette Cuevas Vélez
Jefa del Departamento de Asuntos Escolares

Dr. Marcial Bonilla Marín
Secretario Académico



Acknowledgments

Sincere thanks to Prof. Mauricio and Prof. Humberto for their support, for believing in my capacity, and for pushing my limits.

Thanks to Millie and Gene for their hospitality at MIT and for spreading their motivation to do flag-less science.

I would like to acknowledge the financial support of the SOMENANO during my stay in Boston and to the SNI for a researcher assistant scholarship (2006-2008).

Thanks to David Smith for hosting me at ASU, and to Ado Jorio and Marcos Pimenta for welcoming me at UFMG.

I am grateful to the colleagues that I met during these years, for sharing with me their knowledge and good laughs inside and outside the labs. In particular to Dave Cullen, Ya-Ping, Xiaoting, Mario, Federico, Alfonso, Hootan, and Indhira.

To Andrés and Lau for their friendship.

Special thanks to Daniel Ramírez, Grisel Ramírez, Gaby Pérez, Karla Gómez, Aaron, Ana Laura, Lalo Cruz, Dr. Fernando, Dr. Flo, Dra. Yadira, Dr. Emilio and technicians working at LINAN.

Thanks to my father and mother for their unconditional support and understanding.

To my little sister who lightened my days in spite of being far, far away (de frontera a frontera).

To my brother Daniel and his amazing family: Nancy, Ale and Carlitos.

To my brother David, my mom's family and my dad's family.

I am deeply grateful to Omar whose understanding, ever-lasting love and support keep me going.

Contents

Constancia de aprobación de la tesis	ii
Créditos institucionales	iii
Acta de examen	iv
Acknowledgements	v
List of tables	viii
List of figures	ix
Appendix	xv
Abbreviations	xvi
Abstract	xvii
Resumen	xviii
1. Introduction	1
1.1 Carbon nanotubes	2
1.1.1 Structure	2
1.1.2 Electronic properties	5
1.1.3 Doped carbon nanotubes	7
1.2 Graphene and carbon nanoribbons	13
1.3 References	19
2. Production of doped single-wall carbon nanotubes using the aerosol pyrolysis technique	29
2.1 Description of the synthesis method, materials and equipment	29
2.2 CVD-production of doped single-wall carbon nanotubes	31
2.3 Characterization of CVD-produced doped SWNTs	35
2.3.1 Electron microscopy characterization	36
2.3.2 Raman spectroscopy characterization	47
2.4 Conclusions	60
2.5 Related Articles	62
2.6 References	63

3. Production of graphitic nanoribbons using the aerosol pyrolysis technique	67
3.1 Description of the synthesis method	68
3.2 Characterization of the pristine material	69
3.3 Annealing treatments of carbon nanoribbons	74
3.3.1 Characterization of the annealed materials	76
3.3.2 Raman spectroscopy study of the annealed materials	82
3.4 Conclusions	93
3.5 Related Articles	94
3.6 References	95
4. In situ reconstruction of graphitic nanoribbons by Joule heating	99
4.1 Conditions of the experiment	107
4.2 Crystallization and sharp edge formation	108
4.3 Loop formation at the edges	116
4.4 Estimation of the achieved temperatures	118
4.5 Conclusions	120
4.6 Related Articles	122
4.7 References	123
5. Conclusions and Perspectives	125
5.1 Future work on doped-SWNTS	128
5.2 Future work on carbon nanoribbons	129
Appendix	
Appendix A Carbon nanotubes synthesis methods and characterization tools	131
Appendix B Raman spectroscopy of sp^2 carbon materials	145

List of Tables

2.1	Precursor compounds used in the doping experiments of SWNTs	33
2.2	Experimental conditions used in the synthesis of doped SWNTs	34

List of figures

1.1	Allotropes of carbon	1
1.2	Symmetry classification of nanotubes	3
1.3	Geometry and unit cell of carbon nanotubes	3
1.4	Electronic density of states of two zigzag nanotubes	6
1.5	Kataura plot	6
1.6	Types of doping in carbon nanostructures	7
1.7	Nitrogen doped MWNTs	9
1.8	Phosphorus doping of SWNTs	10
1.9	Silicon doping of SWNTs	11
1.10	Sulfur doping of SWNTs	12
1.11	Structure of armchair and zigzag graphene nanoribbons	13
1.12	Stability of graphene nanoribbons	14
1.13	Methods of production of graphene	16
1.14	CVD and other production methods of carbon nanoribbons	17
2.1	Diagram of the experimental setting for CVD production of SWNTs	30
2.2	TEM images of CVD-produced pristine SWNTs	30
2.3	SEM and STEM images of materials synthesized with thiophene	36

2.4	TEM images of materials synthesized with thiophene	37
2.5	High resolution EDX point measurements on by-products of thiophene-produced samples	38
2.6	SEM images of nitrogen-doped SWNTs produced with benzylamine	38
2.7	SEM and TEM images of nitrogen-doped SWNTs produced with pyrazine	39
2.8	SEM and STEM images of samples synthesized with triphenylphosphine	40
2.9	SEM and TEM images of phosphorous-doped SWNTs	41
2.10	HRTEM micrographs of SWNTs produced with different concentrations of MTMS	43
2.11	HAADF-STEM and EELS analysis of Si-doped SWNTs produced with 0.1 wt. % of MTMS	44
2.12	HAADF-STEM and EELS analysis of Si-doped SWNTs produced with 0.2 wt. % of MTMS	45
2.13	Raman spectra of material synthesized with 0.1 wt. % of thiophene	48
2.14	RBM spectra of materials synthesized with thiophene	49
2.15	Raman spectra of materials synthesized with thiophene	50
2.16	RBM spectra of the samples doped with N, P, and Si at five laser excitation energies	51
2.17	RBM of N- and Si- doped SWNTs recorded at $E_{\text{laser}}=1.95$ eV	52
2.18	RBM resonance Raman maps of P-doped SWNT samples	54

2.19	RBM and G' band spectra of N-,P-, and Si- doped SWNTs at $E_{\text{laser}}=2.41$ eV	55
2.20	$I_{G'_{\text{Def}}}/I_{G'_{\text{Pris}}}$ ratios as a function of doping atoms (P, N and Si) per carbon atoms	56
2.21	G' band and the corresponding Lorentzian fitting of the samples with maximum $I_{G'_{\text{Def}}}/I_{G'_{\text{Pris}}}$ ratios	57
2.22	G' band splitting of the N-, P- and Si- doped SWNTs	59
3.1	Schematic diagram of the experimental set-up for the production of graphitic nanoribbons	68
3.2	SEM images and EDX line scan of graphitic nanoribbons	70
3.3	TEM images of graphitic nanoribbons	71
3.4	XRD, Raman spectroscopy, TGA, N ₂ absorption and XPS of graphitic nanoribbons	73
3.5	Loop formation at the edges of graphene planes induced by heat treatments in different carbon materials	74
3.6	Raman spectroscopy of heat treated carbon materials	75
3.7	SEM images of heat treated graphitic nanoribbons	76
3.8	TEM images of the side-edges of heat treated graphitic nanoribbons	78
3.9	XRD and TGA of heat treated graphitic nanoribbons	79
3.10	Schematic model for the restructuring process achieved during annealing	81

3.11	Bulk Raman spectra of heat treated nanoribbons at seven laser excitation energies	83
3.12	Example of the Lorentzian fitting of Raman spectra	84
3.13	Band positions and I_D/I_G ratios as a function of E_{laser}	85
3.14	FWHM of the G band and I_G/I_G ratios of HT nanoribbons	87
3.15	SEM and AFM imaging of isolated nanoribbons	89
3.17	Raman spectroscopy line scans of individual nanoribbons at $E_{\text{laser}}=2.33$ eV	91
3.18	D and D' band intensities vs. distance in the individual measurements	92
4.1	Wall-by-wall breakdown of MWNTs under Joule heating	99
4.2	In situ observation of wall-by-wall breakdown	100
4.3	Superplasticity of carbon nanotubes	101
4.4	Crystallization of a disordered nanotube by Joule heating	103
4.5	Vacancy migration in carbon nanotubes	104
4.6	Schematic diagram of the TEM-STM system used during Joule heating experiments	107
4.7	IV curve during Joule heating of graphitic nanoribbons	109
4.8	TEM images at different stages of the Joule heating experiment	110
4.9	TEM images of the Joule heating experiment at an applied bias voltage of 1.6 V	111

4.10	Crystallization and edge formation in graphitic nanoribbons by Joule heating	112
4.11	Edge motion under Joule heating	113
4.12	Transport on graphene nanoribbons with different edge configurations	114
4.13	Edge arrays and their time evolution	115
4.14	TEM images of the edges of graphitic nanoribbons annealed in furnace	117
4.15	TEM images showing loop formation by Joule heating	118
4.16	Sequence of TEM images showing Pt nanoparticles on the nanoribbon surface	119
A1	Diagram of an arc-discharge chamber	131
A2	TEM images of arc-discharge produced SWNTs	132
A3	Diagram of a laser ablation set-up	133
A4	SEM and TEM images of SWNTs produced by laser ablation	133
A5	CVD-derived SWNTs	134
A6	X-ray diffraction profiles of graphite and SWNTs	138
A7	C1s XPS signal of MWNTs	139
A8	EELS spectra of carbon allotropes	140
A9	Representative Raman spectra of HOPG, SWNTs and graphene	141

B1	Phonon dispersion of graphene	146
B2	Resonance Raman spectral processes	148
B3	Schematic of the RBM and tangential nanotube vibrations	150
B4	D- and D'- bands double resonance processes	153
B5	Electronic bands of 2D graphite and phonon dispersion curves of 2D graphite	154
B6	G' band features of CVD-grown SWNTs before and after annealing treatments	157
B7	G' band of sp^2 carbon materials	158

Appendix

Appendix A	130
Carbon nanotubes synthesis methods and characterization tools	
Appendix B	143
Raman spectroscopy of sp^2 carbon materials	

Abbreviations

Å	Angstroms (10^{-10} m)
Cp	Cyclopentadienyl (C_5H_5)
CVD	Chemical vapor deposition
EDX	Energy dispersive X-ray analysis
EELS	Electron energy loss spectroscopy
e-beam	Electron beam
eV	Electron volts
HOPG	Highly oriented pyrolytic graphite
HRTEM	High resolution transmission electron microscopy
HT	Heat treatment or heat treated
K	Kelvin degrees
MTMS	Methoxytrimethylsilane
MWNT	Multi-wall carbon nanotube
nm	Nanometers (10^{-9} m)
RBM	Radial breathing mode
SEM	Scanning electron microscopy
STEM	Scanning transmission electron microscopy
SWNT	Single-walled carbon nanotube
TEM	Transmission electron microscopy
TGA	Thermo gravimetric analysis
TPP	Triphenylphosphine
µm	Micrometers (10^{-6} m)
XPS	X-ray photoelectron spectroscopy
XRD	X-ray diffraction

Synthesis and characterization of doped single-walled carbon nanotubes and graphitic nanoribbons

Abstract

An aerosol-assisted chemical vapor deposition technique was used to produce doped SWNTs and graphitic nanoribbons.

The doping elements were introduced to the system by means of precursor compounds, added to ferrocene ($\text{Fe}(\text{C}_5\text{H}_5)_2$) – ethanol ($\text{C}_2\text{H}_6\text{O}$) solutions at different concentrations. Thiophene ($\text{C}_4\text{H}_4\text{S}$), triphenylphosphine ($(\text{C}_6\text{H}_5)_3\text{P}$), benzylamine ($\text{C}_7\text{H}_7\text{NH}_2$), pyrazine ($\text{C}_4\text{H}_4\text{N}_2$) and methoxytrimethylsilane ($\text{CH}_3\text{OSi}(\text{CH}_3)_3$) were the precursors used in this work. The materials thus produced were analyzed with SEM, TEM, EDX, EELS and Raman spectroscopy.

Our experiments with low concentrations of thiophene triggered the synthesis of a new carbon nanostructure: graphitic nanoribbons. Such pristine nanoribbons have been carefully characterized by SEM, TEM, XRD, XPS, TGA, EDX and Raman spectroscopy. The nanoribbons were annealed up to 2800 °C in graphitic furnaces. Characterization of the heat treated samples includes TEM and SEM observation, XRD, TGA and bulk and individual nanoribbon Raman spectroscopy. Our TEM observations revealed that under heat treatments a crystallization process occurs, and above 1500 °C, the adjacent graphitic sheets find a more stable configuration by forming loops. Single, double and multiple loops are formed at different stages of the heat treatments.

Joule heating experiments were also carried out. Our results show that an intense irradiation of the electron beam, prior to the experiment, results in the formation of sharp zigzag and armchair edges; while the experiment of an as-produced nanoribbon results in multiple-loop formation due to the high temperatures that are achieved in the experiment.

KEY WORDS. CVD, doped SWNTs, nanoribbons, loop formation, sharp edges

Síntesis y caracterización de nanotubos de carbono de pared sencilla dopados y de nanolistones gráficos

Resumen

Este trabajo concentra resultados experimentales de la síntesis de nanotubos de carbono de pared sencilla (SWNTs) y de nanolistones gráficos, así como una extensiva caracterización de los mismos. El método de síntesis de SWNTs utilizado consiste en la deposición química de vapores (CVD) asistido por aerosol con catalizador flotante. Para el dopaje de SWNTs se eligieron compuestos precursores que contienen al elemento dopante y se agregaron en diferentes concentraciones a soluciones de ferroceno ($\text{Fe}(\text{C}_5\text{H}_5)_2$) y etanol ($\text{C}_2\text{H}_6\text{O}$). Los precursores con los que se trabajó son: tiofeno ($\text{C}_4\text{H}_4\text{S}$), trifenilfosfina ($(\text{C}_6\text{H}_5)_3\text{P}$), bencilamina ($\text{C}_7\text{H}_7\text{NH}_2$), pirazina ($\text{C}_4\text{H}_4\text{N}_2$) y metoxitrimetilsilano ($\text{CH}_3\text{OSi}(\text{CH}_3)_3$). Los nanotubos de pared sencilla y los co-productos obtenidos fueron estudiados por SEM, TEM, EELS, EDX y espectroscopia Raman.

Nuestros experimentos con bajas concentraciones de tiofeno nos condujeron a la síntesis de nanolistones de carbono. Una completa caracterización mediante las técnicas SEM, TEM, EDX, XPS, XRD, TGA, y espectroscopia Raman se realizó para el material puro, es decir sin tratamientos posteriores a la síntesis.

Se realizaron tratamientos térmicos en hornos de grafito hasta temperaturas de 2800 °C. Los materiales tratados térmicamente fueron evaluados mediante SEM, TEM, XRD, TGA y espectroscopia Raman en bulto y a nivel individual. Se encontró que el material sufre un proceso de cristalización y, arriba de 1500 °C, las orillas de las hojas gráficas adyacentes encuentran una configuración más estable al formar uniones. También se realizaron experimentos de calentamiento de Joule (Joule heating), los resultados prueban que esta técnica permite formar tanto uniones como terminaciones armchair y zigzag dependiendo de las condiciones del experimento.

PALABRAS CLAVE. Dopaje de SWNTs, nanolistones de carbono, uniones

1. Introduction

Carbon is one of the most abundant elements in nature. For a long time, only three allotropes of carbon were known: amorphous carbon, graphite and diamond. The crystalline forms (graphite and diamond) vary in physical properties due to their atomic structure.

The reason why carbon assumes many structural forms is that a carbon atom can form distinct types of valence bonds, where the chemical bonds refer to the *hybridization* of orbitals by physicists¹.

In sp^2 hybridization, the carbon atoms are arranged hexagonally in honeycomb lattices parallel to each other, each of these hexagonally arranged carbon sheets is called graphene (Figure 1.1e). In graphite, the graphene sheets are stacked in an ABAB... sequence with $P6_3/mmc$ symmetry (Figure 1.1a). Accepted values of the lattice constants are $a_0=0.2462$ nm and $c_0=0.6707$ nm at room temperature, so that the in-plane bond length is 0.1421 nm and the interplanar separation is 0.3354 nm. Alternative stacking sequences (AA, ABCABC...) can occur for carbon, as well as the random stacking of graphene layers (turbostratic carbon).²

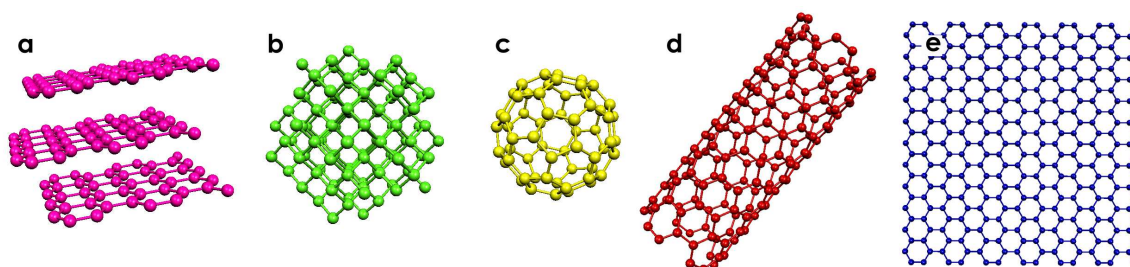


Figure 1.1 Allotropes of carbon, a) AB graphite, b) diamond, c) C_{60} , d) armchair (5,5) carbon nanotube³ and e) graphene sheet.

This layered configuration makes graphite a dark, soft material, where as diamond is transparent and is one of the hardest known materials. In diamond the carbon atoms are bonded tetrahedrally, in this configuration the atoms exhibit sp^3 hybridization (Figure 1.1b).

The first observation of graphene goes back to the early 60's, by Boehm⁴, later in the 70's Oberlin⁵ reported the growth of filamentous carbon where images of hollow carbon nanotubes were published. In 1985 the discovery of C₆₀ (buckminsterfullerene, a molecule constituted of 60 carbon atoms arranged in a truncated icosahedral structure⁶, see Figure 1.1c) triggered the revolution of carbon nanostructures, leading to numerous reports of the synthesis and observation of single-wall carbon nanotubes⁷, nano-onions⁸, nanocones⁹, nanoribbons¹⁰ and more recently, graphene¹¹.

In the following pages a detailed description of the structure and properties of carbon nanotubes, graphene and carbon nanoribbons will be presented.

1.1 Carbon nanotubes

1.1.1 Structure

A single-wall carbon nanotube can be described as a graphene sheet rolled into a cylindrical shape so that the structure is one-dimensional with axial symmetry¹.

Three examples of single-wall carbon nanotubes (SWNTs) are shown in Figure 1.2. From this figure, it can be seen that the direction of the hexagon can be taken almost arbitrarily.

The primary symmetry classification of a carbon nanotube is as either being achiral or chiral. An achiral carbon nanotube is defined by a carbon nanotube whose mirror image has an identical structure to the original one.

There are only two cases of achiral nanotubes; armchair (Figure 1.2a) and zigzag (Figure 1.2b) nanotubes. The names of armchair and zigzag arise from the shape of the cross-sectional ring, as is shown at the edge of the nanotubes in Figure 1.2. Chiral nanotubes exhibit a spiral symmetry whose mirror image cannot be superposed on to the original one. In Figure 1.3, the unrolled honeycomb lattice of the nanotube is shown, in which \overrightarrow{OB} is the direction of the nanotube axis, and the direction \overrightarrow{OA} corresponds to the equator. By considering the crystallographically equivalent sites O , A , B , and B' , and by rolling the honeycomb sheet so that points

O and A coincide (and points B and B' coincide), a paper model of a carbon nanotube can be constructed. The vectors \overrightarrow{OA} and \overrightarrow{OB} define the chiral vector C_h and the translational vector T of a carbon nanotube, respectively.

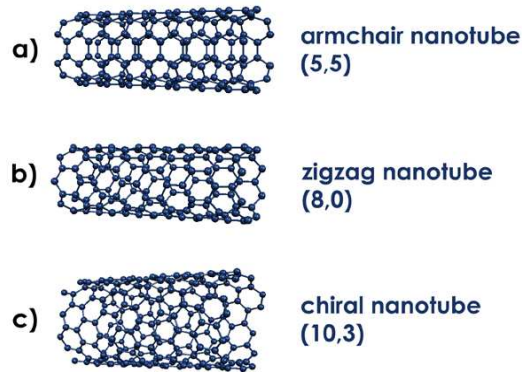


Figure 1.2 Symmetry classification of nanotubes, a) armchair, b) zigzag and c) chiral nanotubes⁸

The chiral vector can be expressed by the real space unit vectors \mathbf{a}_1 and \mathbf{a}_2 (see Figure 1.3) of the hexagonal lattice defined in Equation 1

$$C_h = n\mathbf{a}_1 + m\mathbf{a}_2 \equiv (n, m) \quad (n, m \text{ are integers, } 0 \leq |m| \leq n) \quad (1)$$

The chiral vector C_h shown in Figure 1.3a is (4,2). An armchair nanotube corresponds to the case of $n=m$, that is $C_h=(n,n)$, and a zigzag nanotube corresponds to the case of $m=0$, or $C_h=(n,0)$. All other (n,m) chiral vectors correspond to chiral nanotubes.

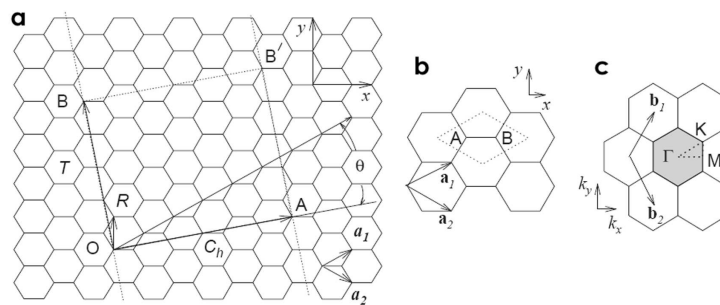


Figure 1.3 a) The unrolled honeycomb lattice of a nanotube. The figure corresponds to $C_h=(4,2)$, b) the unit cell (dotted rhombus), containing sites A and B where carbon atoms are located, and c) the Brillouin zone (shaded hexagon) of a graphene or 2D graphite layer. \mathbf{a}_i and \mathbf{b}_i ($i=1,2$) are basis vectors and reciprocal lattice vectors respectively. The high symmetry points, Γ , K , and M are indicated.¹²

The diameter of the carbon nanotube, d_t , is given by L/π , in which L is the circumferential length of the carbon nanotube:

$$d_t = L/\pi, \quad L = |C_h| = \sqrt{C_h \cdot C_h} = a\sqrt{n^2 + m^2 + mn} \quad (2)$$

where the a is the lattice constant of two dimensional graphite $a = 1.42 \text{ \AA} \times \sqrt{3} = 2.49 \text{ \AA}$. The C-C bond length of graphite is 1.42 \AA . In the case of carbon nanotubes, the C-C- length is known to be slightly larger than graphite; 1.44 \AA .¹

The chiral angle θ is defined as the angle between the vectors C_h and \mathbf{a}_1 , with values of θ in the range $0 \leq |\theta| \leq 30^\circ$, because of the hexagonal symmetry of the honeycomb lattice. The chiral angle θ denotes the tilt angle of the hexagons with respect to the direction of the nanotube axis, and the angle θ specifies the spiral symmetry. The chiral angle θ is defined by taking the inner product of C_h and \mathbf{a}_1 , to yield an expression for $\cos \theta$:

$$\cos \theta = \frac{C_h \cdot a_1}{|C_h||a_1|} = \frac{2n + m}{2\sqrt{n^2 + m^2 + nm}} \quad (3)$$

thus relating θ to the integers (n,m) defined in Equation (1). In particular, zigzag and armchair nanotubes correspond to $\theta=0^\circ$ and $\theta=30^\circ$, respectively.

In Figure 1.3 we show b) the unit cell in real space and c) the Brillouin zone in reciprocal space of 2D graphite as a dotted rhombus and shaded hexagon, respectively, where \mathbf{a}_1 and \mathbf{a}_2 are basis vectors in real space, and \mathbf{b}_1 and \mathbf{b}_2 are reciprocal lattice basis vectors. In the x, y coordinate system shown in Figure 1.3, the real space basis vectors \mathbf{a}_1 and \mathbf{a}_2 of the hexagonal lattice are expressed as $\mathbf{a}_1 = (\sqrt{3}a/2, a/2)$ and $\mathbf{a}_2 = (\sqrt{3}a/2, -a/2)$, where $a = |\mathbf{a}_1| = |\mathbf{a}_2| = 1.42 \times \sqrt{3} = 2.46 \text{ \AA}$ is the lattice constant of a graphene or 2D graphite layer. Correspondingly, the basis vectors of the \mathbf{b}_1 and \mathbf{b}_2 of the reciprocal lattice are given by $\mathbf{b}_1 = (2\pi/\sqrt{3}a, 2\pi/a)$ and $\mathbf{b}_2 = (2\pi/\sqrt{3}a, -2\pi/a)$ corresponding to the graphene lattice constant of $4\pi/\sqrt{3}a$ in reciprocal space. The direction of the basis vectors \mathbf{b}_1 and \mathbf{b}_2 of the reciprocal hexagonal lattice are rotated by 30° from the basis vectors \mathbf{a}_1 and \mathbf{a}_2 of the hexagonal lattice in real space, as shown in Figure 1.3 b) and c). The three high symmetry points, Γ , K , and M of the Brillouin zone are shown as the center,

the corner and the center of the edge, respectively, of the shaded hexagon that corresponds to the Brillouin zone of 2D graphite.

1.1.2 Electronic properties

The electronic structure of a carbon nanotube can be obtained from its parent material, graphite, accounting for quantum confinement of the electronic states in these 1D materials. The electronic σ bands are responsible for the strong in-plane covalent bonds with the 2D graphene sheets, while the π bands are responsible for weak van der Waals interactions between such sheets in graphite.¹³ In 1992 the Japanese group of Hamada and co-workers¹⁴ published a report on tight binding calculations of carbon nanotubes, predicting three classes of transport: metallic nanotubes, semiconducting ones with narrow band gaps and semiconducting nanotubes with moderate band gaps, with the band gap being tunable by choosing the nanotube structure. In the same year Prof. M.S. Dresselhaus's group published a theoretical study of the electronic structure of carbon nanotubes¹⁵, in Figure 1.4 we show an image extracted from that document. In figure 1.4a and 1.4b, the density of states (DOS) of two zigzag nanotubes with $(n,m) = (10,0)$ and $(9,0)$, respectively, are plotted in units of states per unit cell of 2D graphite.

The corresponding DOS of 2D graphite (dotted lines) is also plotted in both figures for comparison. The density of states of the π band becomes singular by folding the two-dimensional energy bands of the graphene layer into the one-dimensional bands of the carbon nanotube, and these singularities are known as van-Hove singularities.¹

In Figure 1.4a, there is an energy gap at the Fermi level ($E=0$), while we have a finite density of states for Figure 1.4b. Thus, we can have both semiconducting (Fig. 1.4a) and metallic (Fig. 1.4b) nanotubes by merely changing the nanotube diameter. The energy gap for the semiconducting nanotubes decreases with increasing diameter d_t and in the limit of $d_t \rightarrow \infty$, we obtain the 2D case of a zero-gap semiconductor.

The condition for a fiber to be metallic is:

$$2n + m = 3q \quad \text{or} \quad |n - m| = 3q \quad (4)$$

where q is an integer. In particular, all armchair fibers are metallic, and zigzag fibers are metallic when n is a multiple of three¹³.

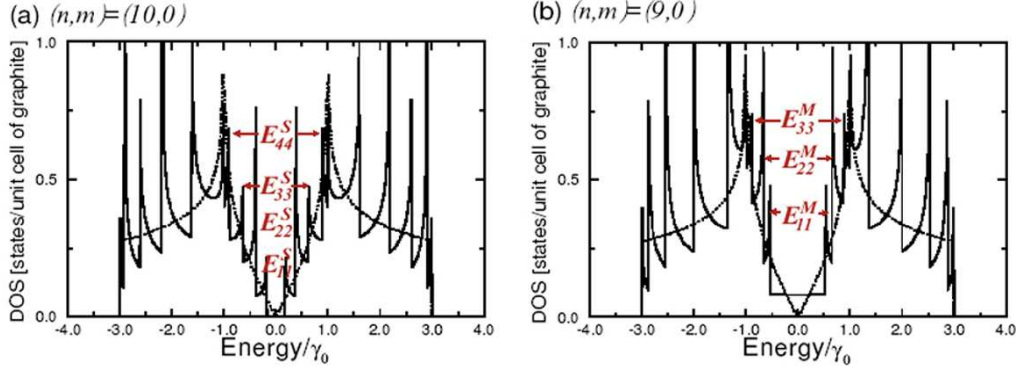


Figure 1.4 Electronic density of states for two (n,m) zigzag fibers: (a) $(10,0)$ and (b) $(9,0)$ ¹⁵

Each nanotube chirality has a corresponding electronic structure, the van-Hove singularities in the density of states of a carbon nanotube give rise to a unique set of transition energies from the valence to the conduction bands for each (n,m) value, denoted as E_{ii} ($ii= 11, 22, 33, \dots$).

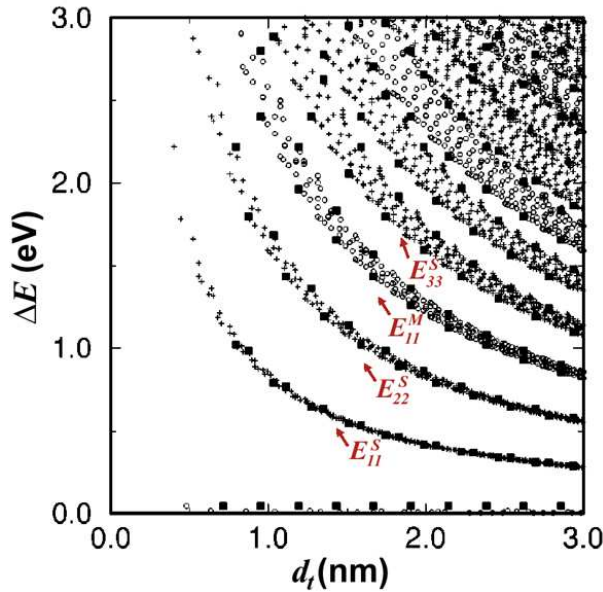


Figure 1.5 Calculation of the energy separations $E_{ii}(d_t)$ for all (n,m) values as a function of nanotube diameter between $0.7 < d_t < 3.0$ nm. The energy transitions were calculated using the tight binding model for carbon nanotubes. The crosses and open circles denote the peaks of semiconducting and metallic nanotubes, respectively. Filled squares denote $E_{ii}(d_t)$ values for zigzag nanotubes which determine the width of each $E_{ii}(d_t)$ curve. Note the points for zero gap metallic nanotubes along the abscissa¹⁶.

In figure 1.4 we can see such

transitions pointed out for the semiconductor and the metallic cases, the S and M labels stand for semiconductor and metallic, respectively.

The interpretation of the interband transitions between van Hove singularities for zigzag nanotubes and chiral nanotubes can be understood by plotting the energies

for the transitions between the van Hove singularities and the valence and conduction bands $E_{ii}(d_i)$ of all possible (n,m) nanotubes¹⁷. Such a plot of $E_{ii}(d_i)$ vs. d_i is shown in figure 1.5 and is known as Kataura plot, this figure is used extensively to interpret resonance Raman spectra in carbon nanotubes.

1.1.3 Doped carbon nanotubes

In materials science we find three approaches of doping: endohedral, exohedral and substitutional, each of them is illustrated in Figure 1.6 in relation to carbon nanostructures.

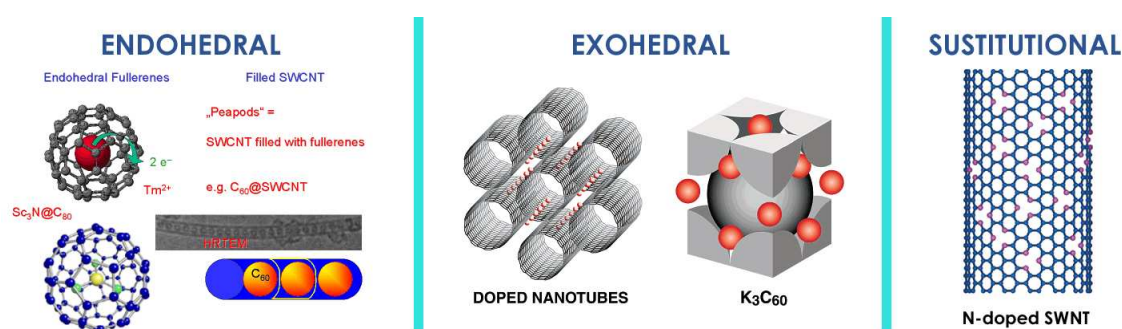


Figure 1.6 Endohedral²⁰, exohedral²³ and substitutional doping³⁴ of carbon nanostructures

Endohedrally doped (filled) nanostructures display a doping method unique to cage molecules and cylinders in which an ion (or ions) are engaged inside the carbon framework of a fullerene molecule or a nanotube. These hybrid-systems represent a completely new type of matter. They are described by the symbol for the encapsulated atom and the fullerene molecule's formula separated by the @ sign, which signals the endohedral nature of the complex, for example La@C₈₂. Endohedral fullerenes containing metal ions (so-called metallofullerenes) could act as vehicles to transport poisonous atoms, can be used as MRI markers in medicine and can be used to stabilize and passivate reactive species. Metal filled nanotubes can act as nonreactive passivated nanomagnets.¹⁸ Last but not least, the so-called peapods (fullerenes filled into SWNT, e.g. C₆₀@SWNT) represent a hybrid system of fullerenes and single wall carbon nanotubes with intriguing new properties.^{19,20}

Exohedral doping of carbon nanostructures consists on the intercalation of certain atoms into available “free” spaces of the carbon arrangement. The intercalation of lithium in between graphitic layers has been studied for a long time.²¹ A few years after the observation of SWNTs by Iijima⁷, Smalley’s group²² found that the single-wall variety (SWNT) self-assembled during growth into partially ordered two-dimensional bundles, or “ropes” with a triangular arrangement. The large one-dimensional trigonal channels between tubes immediately suggested the possibility that ropes might afford a new carbon host lattice for intercalation (see Figure 1.6 Exohedral), and that the reaction would likely be accompanied by charge exchange between host and guest.^{23,24}

It appeared that the crystal chemistry of such phases would be similar to that of graphite intercalation compounds and alkali fullerides.^{23,25}

Substitutional doping of carbon nanostructures happens when foreign atoms replace carbon atoms in the ordered network. Hetero-doping refers to the replacement of C atoms by more than one atom specie. These substitutions alter the electronic properties of the material.

Tailoring the electronic structure of materials by adding impurities is a long-known technique for the semiconductor industry.

P-type and n-type doping of carbon nanotubes is possible if we substitute carbon atoms in the honey-comb lattice with other atomic species with less or more electrons, respectively.

The most common dopants of carbon nanotubes are boron^{26, 27, 28, 29, 30} and nitrogen,^{31,32} which are first neighbors of carbon in the periodic table, in the III and V groups, respectively.

Nitrogen atoms bond in two fashions to carbon atoms, either double-bonded or triple-bonded. Triple bonding of nitrogen corresponds to highly coordinated N atoms replacing C atoms in the graphene sheets; double bonding of nitrogen atoms is commonly referred to as pyridine-like nitrogen (see Figure 1.6 and 1.7C).

For pyridine-like N, it is envisaged that C vacancies are formed within a predominantly hexagonal graphene network, thus leading to stable N-rich cavities

similar to those predicted in C_3N_4 -layered structures. These vacancies also may well be responsible for the formation of irregular graphene sheets.³³

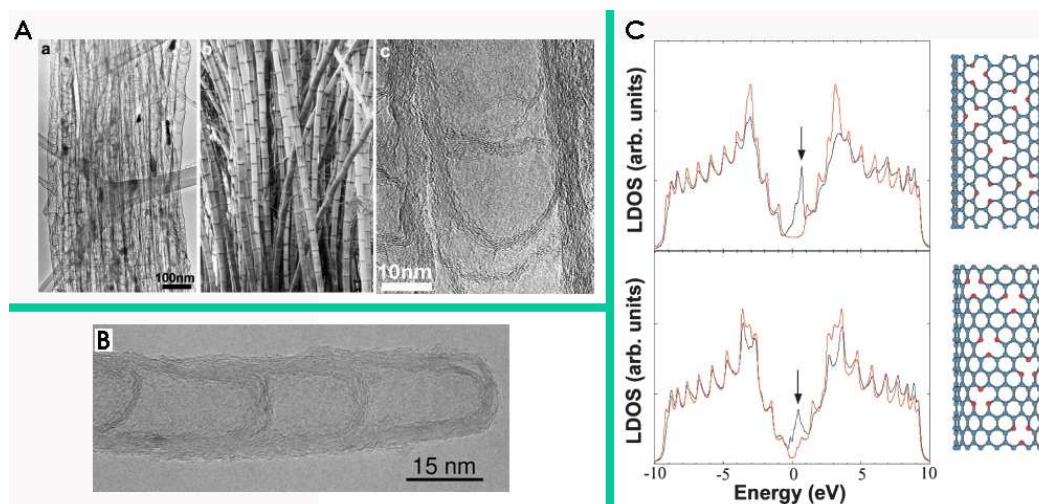


Figure 1.7 Nitrogen doped MWNTs (CNx). (A) a)TEM image of a typical region exhibiting CNx produced by pyrolysis of ferrocene-melamine solutions, b) picture of bamboos, c) HRTEM image of an aligned CNx exhibiting corrugation, interlinkage and compartments.³⁴ (B) HRTEM image of a CNx produced by aerosol pyrolysis.³⁷ (C) Theoretical LDOS associated with a pyridine-like structure with N-doping carbon nanotubes displaying an armchair (10,10) (upper panel) and a zigzag (17,0) (lower panel) configurations. The LDOS of doped (black curve) and pure (red curve) carbon nanotubes are compared.³⁴

The introduction of nitrogen atoms into multi-wall carbon nanotubes (MWNTs) induces the so-called “bamboo-like” morphologies^{34,35,36,37} (see Figure 1.7 A and B). As mentioned before, impurities in the carbon network alter the electronic structure of carbon nanotubes. Terrones *et al.*³⁴ analyzed the DOS associated with the N atoms arranged in a pyridinic fashion, randomly distributed within armchair and zigzag carbon nanotubes. The corresponding DOS for both types of chiralities are depicted in Figure 1.7C. It is clear that pyridine-like sites are responsible for the prominent donor-like features (shown by arrows in the conduction band) just above the Fermi energy.

The production of N-doped SWNTs has been achieved by arc discharge³⁸ and through the pyrolysis of ferrocene-benzylamine solutions in 2005 by Villalpando-Paez and co-workers³⁹. We have reproduced these results and we have achieved

the synthesis of N-doped SWNTs using a different nitrogen precursor, namely, pyrazine.⁴⁰

Although P atoms are larger than C atoms, it has been shown that phosphorus can form substitutional defects in diamond sp^3 thin films⁴¹. In the case of carbon nanotubes, P behaves as an *n*-type donor and modifies the electronic and optical properties. In Figure 1.8a we show the optimized structure of a zigzag (10,0) nanotube with a single substitutional phosphorus atom,⁴² it is evident that due to the larger size of the doping atom, it lies outside the cylindrical wall of the nanotube (consequence of the longer P-C bonds).

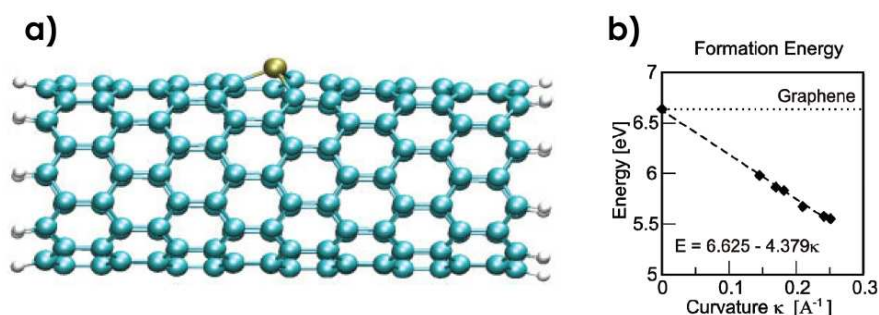


Figure 1.8 a) Optimized structure of a hydrogen passivated (10,0) carbon nanotube with a single P substitutional defect (179 C, 1 P, and 20 H atoms).⁴² b) Plot of defect formation energy vs. curvature. Dotted line represents the formation energy for a planar graphene sheet, as the limit for large nanotubes.⁴³

Maciel and co-authors⁴³ computed the defect formation energy for carbon nanotubes from DFT, considering $\Delta E = E_D - E_{\text{Pris}} - \mu_P - \mu_C$ where E_D (E_{Pris}) is the total energy for the P-doped (pristine) SWNT, and μ_P (μ_C) is the total energy of isolated P (C) atoms. These energies are plotted in Figure 1.8b, showing that the formation energy decreases as the curvature κ (inverse of the nanotube radius) increases, with a fitted relation ΔE (eV) $\sim 6.625 - 4.379\kappa$. This reduction reflects the lower strain in the carbon network required to accept the trigonal bonds of the phosphorus ion when the nanotube diameter decreases. Therefore, phosphorus doping is more likely to occur in small diameter nanotubes and in fact can induce the formation of thinner nanotubes when doping occurs during growth (similar results have been found for nitrogen doping⁴⁴).

In the literature we can find experimental reports of phosphorous-nitrogen hetero-doping of multi-wall carbon nanotubes⁴⁵. We have been able to synthesize for the first time, phosphorus-doped SWNTs.⁴³ A full description of the synthesis procedure and materials is given in Chapter II.

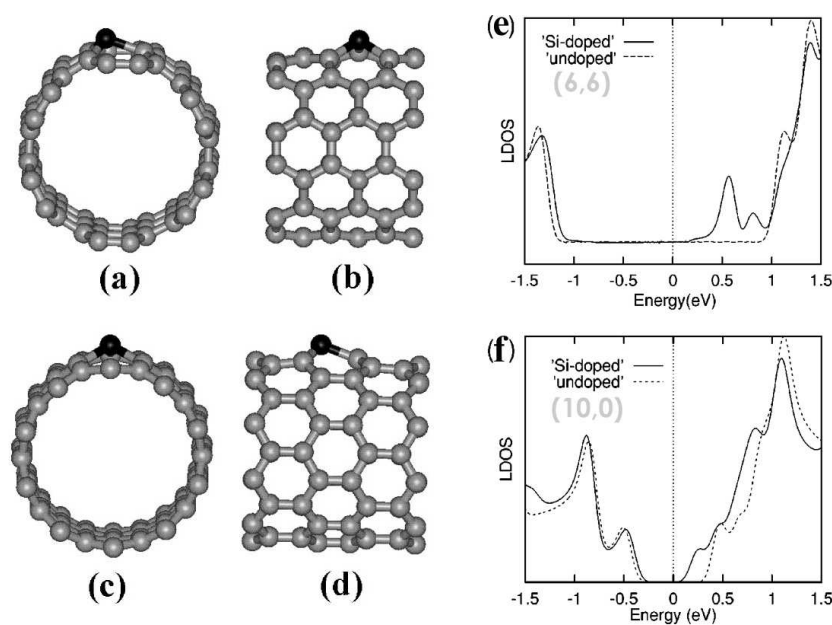


Figure 1.9 Two different views of nanotubes with one substitutional Si atom: a) (6,6) frontal, b) (6,6) lateral, c) (10,0) frontal, and d) (10,0) lateral. Electronic density of states for the doped (filled line) and undoped (dashed line) nanotubes: e) (6,6) nanotube and f) (10,0) nanotube.⁴⁸

Silicon doping of fullerenes⁴⁶ and fullerene-like⁴⁷ nanostructures has been achieved experimentally and was reported in the late 90's. The incorporation of silicon species into the hexagonal lattice of SWNTs was proposed theoretically by Baierle *et al.* in 2001.⁴⁸ These calculations showed that Si-doping of SWNTs introduces donor-like states above the Fermi level (silicon acts as an electron donor), as pictured in Figure 1.9 e) and f). To this date the synthesis of Si-doped SWNTs has not yet been reported.

Sulfur had been demonstrated to play a key role in the synthesis of carbon nanostructures since 1981, when Katsuki *et al.*^{49,50} reported that sulfur exerts an excellent catalytic effect to produce carbon fibers, it has also been reported in the synthesis of DWNTs⁵¹ and nanotube fibers⁵².

However, it was only very recently that the incorporation of S into the sp^2 carbon lattice was experimentally demonstrated⁵³. From electronic structure calculations, we note that the inclusion of S into CNT has similar effects as what was found for

P. S is also a larger atom than C and tends to induce large corrugation when incorporated into sp^2 -like graphitic, fullerene, and nanotube structures.

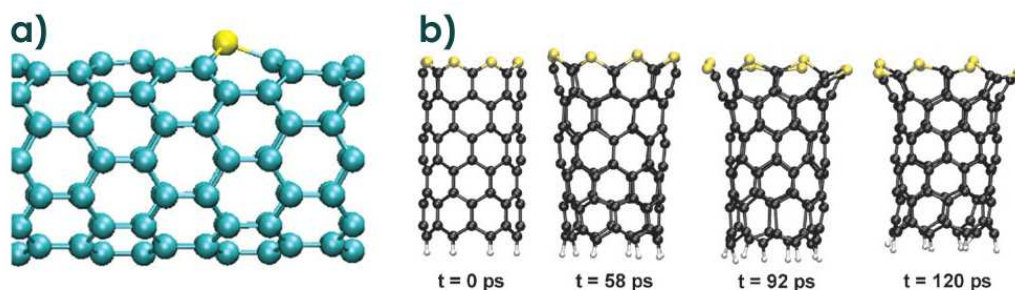


Figure 1.10 a) Optimized geometry for a (8,0) nanotube with a single S substitutional defect.⁴² b) Snapshots from quantum molecular dynamics simulations, showing the effect of widening the CNT diameter in the presence of sulfur.⁵³

Figure 1.10a shows the optimized structure for a single S substitutional defect in a (8,0) nanotube at $T = 1000$ K. The sulfur atoms promote the formation of a small bump when they go out of the sp^2 carbon lattice plane. This system becomes unstable at higher temperatures (2,500 K) and bond dissociation occurs at the site of the S substitution. Addition of a full ring of S atoms into a (8,0) nanotube is stable at relatively high temperatures (up to 2,500 K) but the substitution causes a significant widening of the nanotube, as pictured in Figure 1.10b. This widening can be directly correlated with the formation of heptagonal rings (negative curvature) and could be caused by the so-called cone-stacked structure and branching usually observed in carbon fibers when sulfur is present during synthesis.⁵³

The interesting properties of doped SWNTs have motivated us to work with an aerosol assisted CVD technique with floating catalyst to produce single-wall carbon nanotubes in the presence of sulphur, nitrogen, phosphorus and silicon using compound precursors for each of the listed elements.

A careful description of the experiments, synthesized materials and characterization results will be given in Chapter II.

1.2 Graphene and carbon nanoribbons

Graphene is the name given to a flat monolayer of carbon atoms tightly packed into a two dimensional (2D) honey-comb lattice, and is a basic building block for graphitic materials of all other dimensionalities.⁵⁴

Whether a strictly 2D crystal can exist, was first raised theoretically more than 70 years ago by Peierls and Landau.⁵⁵ They showed that, in the standard harmonic approximation, thermal fluctuations should destroy long-range order, resulting in the melting of a 2D lattice at any finite temperature.

However, although theory does not allow perfect crystals in 2D space, it does not forbid nearly perfect 2D crystals in 3D space.

Indeed, a detailed analysis of the 2D crystal problem beyond the harmonic approximation has led to the conclusion that the interaction between bending and stretching long-wavelength phonons could in principle stabilize atomically thin membranes through their deformation in the third dimension.^{54,56}

In 1996 Nakada *et al.*⁵⁷ calculated the electronic properties of graphene nanoribbons, with different edge configurations and widths using a tight binding (TB) approximation.

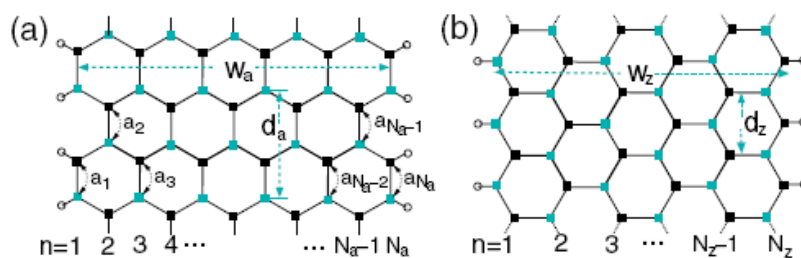


Figure 1.11 a) Schematic of an armchair nanoribbon with $N_a=11$. The empty circles denote hydrogen atoms passivating the edge carbon atoms, and the black and blue rectangles represent atomic sites belonging to different sublattices in the graphene structure. The 1D unit cell distance and ribbon width are represented by d_a and w_a , respectively. (b) Schematic of a $N_z=6$ zigzag nanoribbon.⁵⁸

Such graphite networks have an electronic structure which is somewhat different from that of bulk graphite, since quite a large fraction of the carbon atoms sit on the

edge. There are two basic shapes for graphite edges, namely, armchair and zigzag edges. The graphene nanoribbons with armchair shaped edges on both sides are classified by the number of dimer lines (N_a) across the ribbon width (Figure 1.11a). Likewise, ribbons with zigzag shaped edges on both sides are classified by the number of the zigzag chains (N_z) across the ribbon width (Figure 1.11b).

Their TB results showed that in armchair edge configurations, the ribbon width can determine the metallic or semiconductor behavior, whereas pure zigzag configurations or mixtures of zigzag-armchair configurations result in special localized states near the Fermi level, regardless of the nanoribbon width.

More recent calculations by Louie and co-workers⁵⁸ based on a first-principles approach, demonstrated that both types of edges have non-zero and direct band gaps. In the case of armchair nanoribbons, a semiconductor behavior was found, with energy gaps decreasing as a function of increasing ribbon widths (w_a). The variations in energy gap however exhibit three distinct family behaviors.

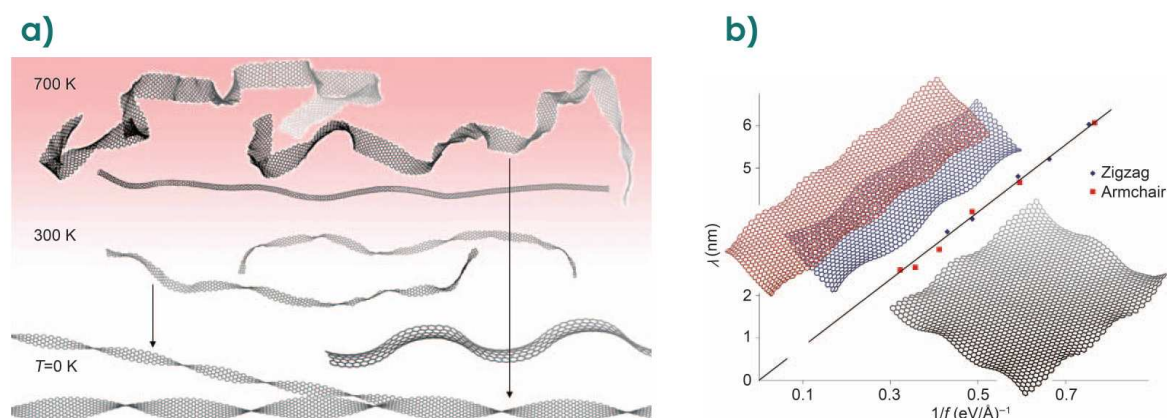


Figure 1.12 a) Representative configurations of graphene nanoribbons (GNRs) from MD (molecular dynamics) simulations at different temperatures, T . At $T=700$ K, two samples of 13-AGNRs and one of a (6,0) nanotube, for comparison are shown. At $T=300$ K, two samples of 7-AGNRs are shown. Ground state configurations, at $T=0$ K, of the GNRs display a saddle-shape chain and periodic twist configurations. b) The twist of GNRs disappears for wider ribbons (here zigzag in dark red and armchair in dark blue) and is replaced by the near-edge undulations, a large pristine graphene sheet in equilibrium displays a near-edge “frills” pattern; the computed period λ of the edge-ripple is plotted as a function of inverse edge force, $1/f$. (Extracted from Reference 59).

When the nanoribbons are terminated with zigzag edges, the first-principles results predict also direct band gaps which decrease with increasing width (w_z). However, when spins are considered, the zigzag nanoribbons are predicted to have a magnetic insulating ground state with ferromagnetic ordering at each zigzag edge and antiparallel spin orientation between the two edges.⁵⁸

In pristine graphene ribbons, disruption of the aromatic bond network results in depopulation of covalent orbitals and tends to elongate the edge, with an effective force of $f_e \sim 2 \text{ eV/\AA}$ (larger for armchair edges than for zigzag edges, according to calculations by Yakobson⁵⁹). This force can have quite striking macroscopic manifestations in the case of narrow ribbons, as it favors their spontaneous twisting, resulting in the parallel edges forming a double helix, resembling DNA, with a pitch λ_t of about 15 - 20 lattice parameters, see Figure 1.12a. Through atomistic simulations, Yakobson investigated how the torsion $\tau \sim 1/\lambda_t$ decreases with the width of the ribbon, and observed its bifurcation: the twist of wider ribbons abruptly vanishes and instead the corrugation localizes near the edges (see Figure 1.12b).

Monolayer graphene was presumed not to exist in the free state, although it was observed in 1962 by Boehm⁴, unfortunately this work was not widely known. Graphene was for long described as an 'academic' material and was believed to be unstable with respect to the formation of curved structures such as soot, fullerenes and nanotubes.

Suddenly, the model turned into reality, when free-standing graphene was unexpectedly found in 2004 by Novoselov and Geim's group.^{11,54}

The importance of graphene is attributed to its amazing electronic properties showing ambipolar electric field effect, quantum hall effect at room temperature, and the fact that its charge carriers are described by the Dirac equation as massless fermions.⁵⁴

A significant draw-back in this graphene revolution is the lack of control of the dimensions and the edge structure (either zigzag or armchair) of the crystals, since both characteristics are crucial on the determination of the electronic properties.

Novoselov's preparation method¹¹ consists on the production of monolayer and few-layer graphene flakes by micro-mechanical exfoliation of HOPG, being worldwide known as the "scotch-tape" method; this friendly production technique put graphene on the spot light by making it available to any research lab around the world (see Figure 1.13A).

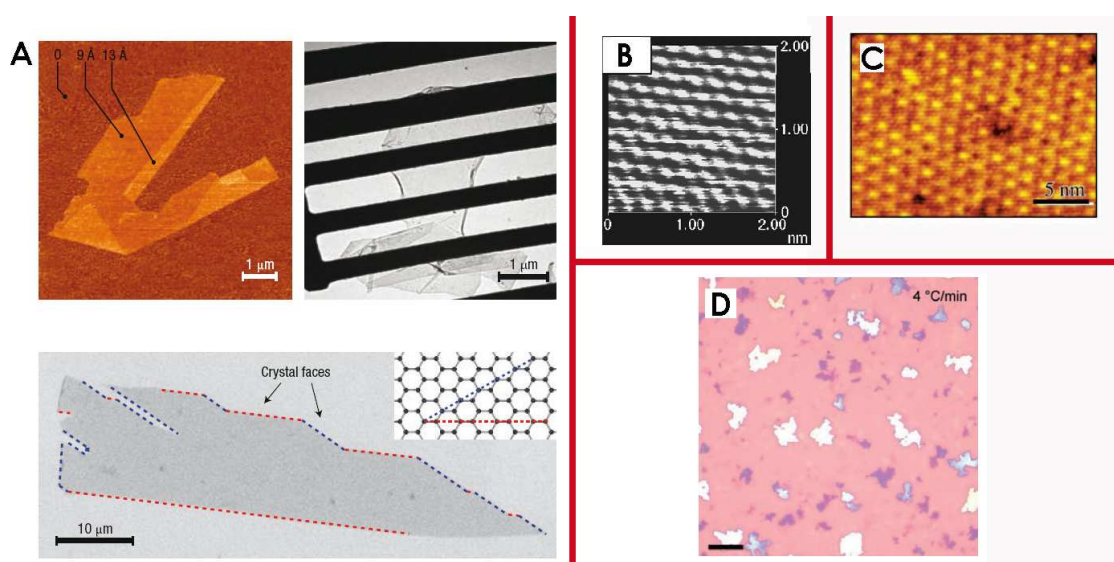


Figure 1.13 Methods of production of graphene. A) Novoselov graphene flakes obtained by micro-mechanical cleavage,⁵⁴ B) high temperature heat treatments of diamond nano-particles⁶⁰, C) epitaxial growth of graphene over SiC substrates^{60,61}, D) CVD grown graphene films over Ni thin layers (scale bar = 25 μ m)⁶².

Apart from Novoselov's micro mechanical cleavage of HOPG to produce graphene, there are other available methods: high temperature heat treatments of diamond nano-particles⁶¹, the epitaxially grown graphene sheets over SiC substrates⁶² and the CVD production of graphene films^{63,64,65} (Figure 1.13 B-D).

In the literature are reported several ways to obtain carbon nanoribbons: temperature and pressure treatments of carbon nanotubes⁶⁶, heat treatment of

diamond nanoparticles deposited on HOPG⁶⁷, chemical treatments of graphite⁶⁸, pyrolysis of hydrocarbons^{8, 69, 70, 71}, using hydrothermal processes^{72, 73}, STM lithography⁷⁴, and more recently by unfolding^{75, 76} or etching carbon nanotubes⁷⁷, see Figure 1.14.

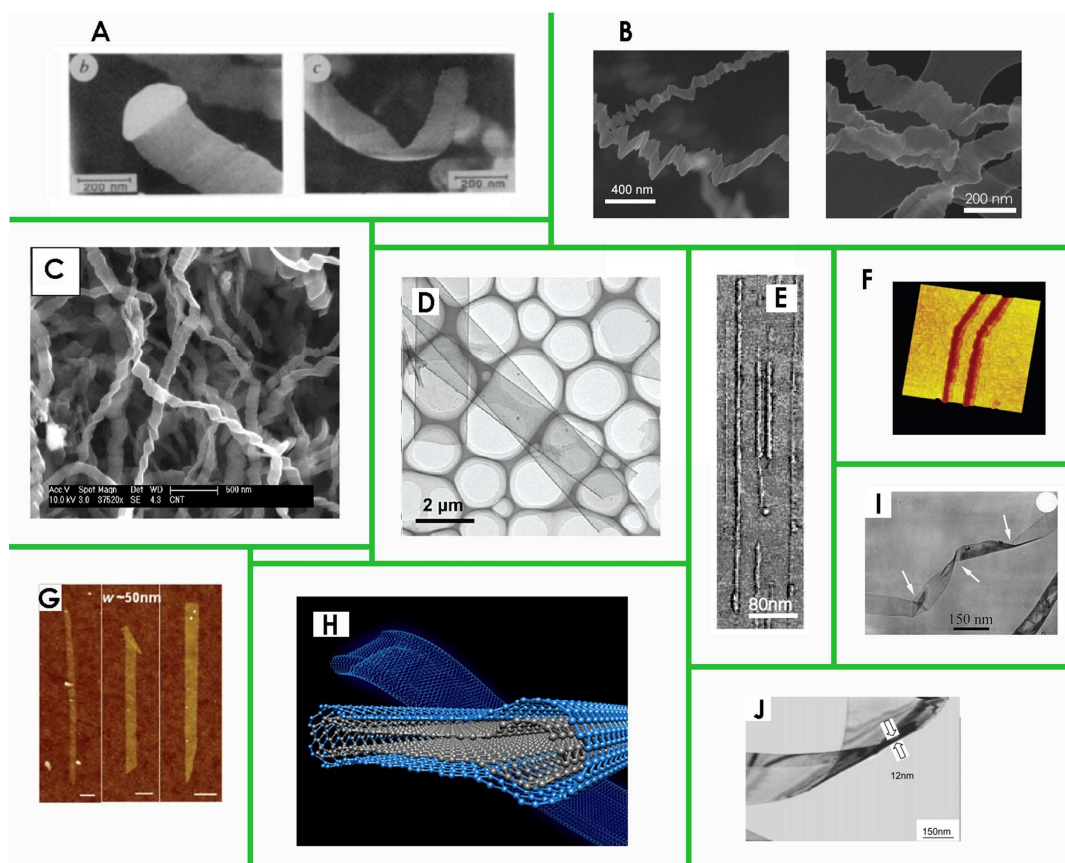


Figure 1.14 CVD and other production methods of carbon nanoribbons. A) Scanning electron micrographs of Maruyama's filamentous graphite, where iron particles at the ends of the structures were found¹⁰, B) SEM images of the graphitic nanoribbons produced by pyrolysis of ethanol-ferrocene-thiophene solutions⁶⁹, C) SEM image of the nanoribbons produced by pyrolysis of THF and ferrocene solutions⁶⁸, D) low magnification TEM image of the nanoribbons produced by the ZnS template method⁷⁰, E) AFM image of the nanoribbons obtained through high temperature treatments of diamond nano-particles⁶⁶, F) 3D STM image of an 8-nm-wide graphene nanoribbon patterned by STM lithography⁷³, G) AFM image of chemically derived nanoribbons from graphite (scale bars = 100 nm)⁶⁷, H) scheme illustrating the structure of a collapsed nanotube⁷⁹, I) and J) TEM images of an amorphous carbon nanoribbon and graphitic nanobelt, respectively, produced by hydrothermal processes^{71, 72}.

Besides the attempts to synthesize carbon nanoribbons, it has been observed that collapsed nanotubes result in nanobelts or nanoribbons with closed edges as reported since 1995 (see Figure 1.14H).^{78,79,80,81,82}

Despite the production methods listed above, the synthesis of nanoribbons is still a challenge, due to drawbacks like the low yield production of the material, high pressure and temperature required for the synthesis, specific equipment and high purity materials involved in the processes and most of all, lack of control on the final structure of the nanoribbons.

The third chapter of this work is devoted to the CVD synthesis of graphitic nanoribbons. A detailed description of the synthesis technique, complete characterization and heat treatment results induced by furnace heating will be presented.

The fourth chapter of this thesis is devoted to the presentation of results of Joule heating experiments on pristine graphitic nanoribbons.

1.3 References

- ¹ R. Saito, G. Dresselhaus, M.S. Dresselhaus. *Physical Properties of Carbon Nanotubes*. Imperial College Press. London, 1998
- ² M.S. Dresselhaus, G. Dresselhaus, K. Sigihara, I.L. Spain, H.A. Goldberg. *Graphite fibers and filaments*. Springer series in Materials Science 5. Springer-Verlag, New York, Berlin, Heidelberg. 1988
- ³ Coordinates generated with S. Maruyama's free software "Wrapping", downloaded from the site <http://www.photon.t.u-tokyo.ac.jp/~maruyama/wrapping3/wrapping.html>
- ⁴ H. P. Boehm, A. Clauss, G. Fischer, U. Hofmann. *Surface properties of extremely thin graphite lamellae*. Proceedings of the Fifth Conference on Carbon. Pergamon Press, Oxford/London/New York/Paris, 1962
- ⁵ A. Oberlin, M. Endo, T. Koyama. *Filamentous growth of carbon through benzene decomposition*. Journal of Crystal Growth 32, 335-349, 1976
- ⁶ H.W. Kroto, J.R. Heath, S.C. O'Brien, R.F. Curl, R.E. Smalley. *C₆₀: Buckminsterfullerene*. Nature 318, 162-163, 1985
- ⁷ S. Iijima. *Helical microtubules of graphitic carbon*. Nature 354, 56-58, 1991
- ⁸ D. Ugarte. *Curling and closure of graphitic networks under electron-beam irradiation*. Nature 359, 707-709, 1992
- ⁹ A. Krishnan, E. Dujardin, M.M.J. Treacy, J. Huggdahl, S. Lynum, T.W. Ebbesen. *Graphitic cones and the nucleation of curved carbon surfaces*. Nature 388, 451-454, 1997
- ¹⁰ H. Murayama, T. Maeda. *A novel form of filamentous graphite*. Nature 345, 792-793, 1990
- ¹¹ K.S. Novoselov, A.K. Geim, S.V. Morozov, D. Jiang, Y. Zhang, S.V. Dubonos, I.V. Grigorieva, A.A. Firsov. *Electric field effect in atomically thin carbon films*. Science 306, 666-669, 2004

-
- ¹² M.S. Dresselhaus, G. Dresselhaus, R. Saito, A. Jorio. *Raman spectroscopy of carbon nanotubes*. Physics Reports 409, 47, 2005
- ¹³ A. Jorio, R. Saito, G. Dresselhaus, M.S. Dresselhaus. *Determination of nanotubes properties by Raman spectroscopy*. Phil. Trans. R. Soc. Lond. A 362, 2311-2336, 2004
- ¹⁴ N. Hamada, S. Sawada, A. Oshiyama. *New one-dimensional conductors: graphitic microtubules*. Phys. Rev. Lett. 68, 10, 1579-1581, 1992
- ¹⁵ R. Saito, M. Fujita, G. Dresselhaus, M.S. Dresselhaus. *Electronic structure of chiral graphene tubules*. Appl. Phys. Lett. 60, 18, 1992
- ¹⁶ R. Saito, G. Dresselhaus, M.S. Dresselhaus. *Trigonal warping effect of carbon nanotubes*. Phys. Rev. B 61, 4, 2981-2990, 2000
- ¹⁷ M.S. Dresselhaus, P.C. Eklund. *Phonons in carbon nanotubes*. Advances in Physics 49, 6, 705-814, 2000
- ¹⁸ K. Lafdi, A. Chin, N. Ali, J.F. Despres. *Cobalt-doped carbon nanotubes: preparation, texture, and magnetic properties*. J. Appl. Phys. 79, 8, 6007-6009, 1996
- ¹⁹ B. W. Smith, M. Monthieux, D. E. Luzzi. *Encapsulated C₆₀ in carbon nanotubes*. Nature 396, 323-324, 1998
- ²⁰ Extracted from : www.ifw-dresden.de/institutes/iff/research/Carbon/CNT/electronic-and-optical-properties/doped/filling
- ²¹ M.S. Dresselhaus, G. Dresselhaus, J.E. Fischer. *Graphite intercalation compounds: electronic properties in the dilute limit*. Phys. Rev. B 15, 3180-3191, 1977
- ²² A. Thess, R. Lee, P. Nikolaev, H. Dai, P. Petit, J. Robert, C. Xu, Y. H. Lee, S.G. Kim, A.G. Rinzler, D.T. Colbert, G.E. Scuseria, D. Tománek, J.E. Fischer, R.E. Smalley. *Crystalline ropes of metallic carbon nanotubes*. Science 273, 483-487, 1996

-
- ²³ J. E. Fischer. *Chemical doping of single-wall carbon nanotubes*. Acc. Chem. Res. 35, 1079-1086, 2002
- ²⁴ J. Kong, C. Zhou, E. Yenilmez, H. Dai. *Alkaline metal-doped n-type semiconducting nanotubes as quantum dots*. Appl. Phys. Lett. 77, 24, 3977-3979, 2000
- ²⁵ T. Kanigaki, T.W. Ebbesen, S. Saito, J. Mizuki, J.S. Tsai, Y. Kubo, S. Kuroshima. *Superconductivity at 33 K in $Cs_xRb_yC_{60}$* . Nature 352, 222-223, 1991.
T. Yildirim, O. Zhou, J.E. Fischer, N. Bykovetz, R.A. Strongin, M.A. Cichy, A.B. Smith III, C.L. Lin, R. Jelinek. *Intercalation of sodium heteroclusters into the C_{60} lattice*. Nature 360, 568-571, 1992
- ²⁶ B.C. Satishkumar, A. Govindaraj, K.R. Harikumar, J.-P. Zhang, A.K. Cheetham, C.N.R. Rao. *Boron-carbon nanotubes from the pyrolysis of C_2H_2 - B_2H_6 mixtures*. Chem. Phys. Lett. 300, 473-477, 1999
- ²⁷ X. Blase, J.-C. Charlier, A. De Vita, R. Car, Ph. Redlich, M Terrones, W.K. Hsu, H. Terrones, D.L. Carroll, P.M. Ajayan. *Boron-mediated growth of long helicity-selected carbon nanotubes*. Phys. Rev. Lett. 83, 24, 5078- 5081, 1999
- ²⁸ W. Han, Y. Bando, K. Kurashima, T. Sato. *Boron-doped carbon nanotubes prepared through a substitution reaction*. Chem. Phys. Lett. 299, 368-373, 1999
- ²⁹ D. Goldberg, Y. Bando, W. Han, K. Kurashima, T. Sato. *Single-walled B-doped carbon, B/N-doped carbon and BN nanotubes synthesized from single-walled carbon nanotubes through a substitution reaction* Chem. Phys. Lett. 308, 337-342, 1999
- ³⁰ K. MacGuire, N. Gothard, P.L. Gai, M.S. Dresselhaus, G. Sumanasekera, A.M. Rao. *Synthesis and Raman characterization of boron-doped single-walled carbon nanotubes*. Carbon 43, 219-227, 2005

-
- ³¹ O. Stephan, P.M. Ajayan, C. Colliex, Ph. Redlich, J.M. Lambert, P. Bernier, P. Lefin. *Doping graphitic and carbon nanotube structures with boron and nitrogen*. Science 266, 5191, 1683, 1994
- ³² M. Terrones, N. Grobert, J. Olivares, J.P. Zhang, H. Terrones, K. Kordatos, W.K. Hsu, J.P. Hare, P.D. Townsend, K. Prassides, A.K. Cheetham, H.W. Kroto, D.R.M. Walton. *Controlled production of aligned-nanotube bundles*. Nature 388, 52, 1997
- ³³ M. Terrones, P. Redlich, N. Grobert, S. Trasobares, W.-K. Hsu, H. Terrones, Y.-Q. Zhu, J. P. Hare, C. L. Reeves, A. K. Cheetham, Manfred Rühle, H. W. Kroto, D.R. M. Walton. *Carbon nitride nanocomposites: formation of aligned C_xN_y nanofibers*. Advanced Materials 11, 8, 655, 1999
- ³⁴ M. Terrones, P.M. Ajayan, F. Banhart, X. Blase, D.L. Carroll, J.C. Charlier, R. Czerw, B. Foley, N. Brobert, R. Kamalakaran, P. Kohler-Redlich, M. Rühle, T. Seeger, H. Terrones. *N-doping and coalescence of carbon nanotubes: synthesis and electronic properties*. Appl. Phys. A 74, 355-361, 2002
- ³⁵ R. Sen, B.C. Satishkumar, A. Govindaraj, K.R. Harikumar, G. Raina, J.-P. Zhang, A.K. Cheetham, C.N.R. Rao. *B-C-N, C-N, and B-N nanotubes produced by the pyrolysis of precursor molecules over Co catalysts*. Chem. Phys. Lett. 287, 671-676, 1998
- ³⁶ R. Droppa Jr., P. Hammer, A.C.M. Carvalho, M.C. dos Santos, F. Alvarez. *Incorporation of nitrogen in carbon nanotubes*. Journal of Non-Crystalline Solids 299-302, 874-879, 2002
- ³⁷ M. Glerup, M. Castignolles, M. Holzinger, G. Hug, A. Loiseau, P. Bernier. *Synthesis of highly nitrogen-doped multi-walled carbon nanotubes*. Chem. Commun. 2542-2543, 2003
- ³⁸ M. Glerup, J. Steinmetz, D. Samaille, O. Stéphane, S. Enouz, A. Loiseau, S. Roth, P. Bernier. *Synthesis of N-doped SWNT using the arc-discharge procedure*. Chem. Phys. Lett. 238, 193-197, 2004

-
- ³⁹ F. Villalpando-Paez, A. Zamudio, A.L. Elias, H.Son, E.B. Barros, S.G. Chou, Y.A. Kim, H. Muramatsu, T. Hayashi, J. Kong, H. Terrones, G. Dresselhaus, M. Endo, M. Terrones, M.S. Dresselhaus. *Synthesis and characterization of long strands of nitrogen-doped single-walled carbon nanotubes*. Chem. Phys. Lett. 424, 345-352, 2006
- ⁴⁰ J. Campos-Delgado, I.O. Maciel, D. A. Cullen, D. Smith, A. Jorio, M.A. Pimenta, H. Terrones, M. Terrones. *Chemical vapor deposition synthesis of N-, P- and Si-doped single-wall carbon nanotubes*. (Submitted to ACS Nano in November 2009)
- ⁴¹ H. Sternschulte, K. Thonke, R. Sauer, S. Koizumi. *Optical evidence for 630-meV phosphorus donor in synthetic diamond*. Phys. Rev. B 59, 20 , 12924-12927, 1999
- ⁴² B. G. Sumpter, J. Huang, V. Meunier, J. M. Romo-Herrera, E. Cruz-Silva, H. Terrones, M. Terrones. *A theoretical and experimental study on manipulating the structure and properties of carbon nanotubes using substitutional dopants*. Int. J. of Quant. Chem. 109, 97-118, 2009
- ⁴³ I.O. Maciel, J. Campos-Delgado, E. Cruz-Silva, M.A. Pimenta, B.G. Sumpter, V. Meunier, F. López-Urías, E. Muñoz-Sandoval, H. Terrones, M. Terrones, A. Jorio. *Synthesis, electronic structure, and Raman scattering of phosphorus-doped single-wall carbon nanotubes*. Nanoletters 9,6, 2267-2272, 2009
- ⁴⁴ B. G. Sumpter, V. Meunier, J.M. Romo-Herrera, E. Cruz-Silva, D.A. Cullen, H. Terrones, D.J. Smith, M. Terrones. *Nitrogen-mediated carbon nanotube growth: diameter reduction, metallicity, bundle dispersability, and bamboo-like structure formation*. ACS Nano 1, 4, 369-375, 2007
- ⁴⁵ E. Cruz-Silva, D.A. Cullen, L. Gu, J.M. Romo-Herrera, E. Muñoz-Sandoval, F. López-Urías, B.G. Sumpter, V. Meunier, J.-C. Charlier, D. J. Smith, H. Terrones, M. Terrones. *Heterodoped nanotubes: theory, synthesis, and characterization*

-
- of phosphorus-nitrogen doped multiwalled carbon nanotubes*. ACS Nano 2, 3, 441-448, 2008
- ⁴⁶ T. Kimura, T. Sugai, H. Shinohara. *Production and characterization of boron- and silicon-doped carbon clusters*. Chem. Phys. Lett. 256, 269-273, 1996
- ⁴⁷ C. Ray, M. Pellarin, J.L. Lermé, J.L. Vialle, M. Broyer, X. Blase, P. Mélinon, P. Kéghélian, A. Perez. *Synthesis and structure of silicon-doped heterofullerenes*. Phys. Rev. Lett. 80, 24, 5365, 1998
- ⁴⁸ R.J. Baierle, S. B. Fagan, R. Mota, A. J. R. da Silva, A. Fazzio. *Electronic and structural properties of silicon-doped carbon nanotubes*. Phys. Rev. B 64, 085413, 2001
- ⁴⁹ H. Katsuki, K. Matsunaga, M. Egashira, S. Kawasumi. *Formation of carbon fibers from naphthalene on some sulfur-containing substrates*. Carbon 19, 148-150, 1981
- ⁵⁰ G. Tibbetts, C.A. Bernardo, D. W. Gorkiewicz, R.L. Alig. *Role of sulfur in the production of carbon fibers in the vapor phase*. Carbon 32, 4, 569-576, 1994
- ⁵¹ L.Ci, Z. Rao, Z. Zhou, D. Tang, X. Yan, Y. Liang, D. Liu, H. Yuan, W. Zhou, G. Wang, W. Liu, S. Xie. *Double wall carbon nanotubes promoted by sulfur in a floating iron catalyst CVD system*. Chem. Phys. Lett. 359, 63-67, 2002
- ⁵² Y.-L. Li, I.A. Kinloch, A.H. Windle. *Direct spinning of carbon nanotube fibers from chemical vapor deposition synthesis*. Science 304, 276-278, 2004, and M. Motta, Y.-L. Li, I. Kinloch, A. Windle. *Mechanical properties of continuously spun fibers of carbon nanotubes*. Nanoletters 5, 8, 1529-1533, 2005
- ⁵³ J. M. Romo-Herrera, B.G. Sumpter, D.A. Cullen, H. Terrones, E. Cruz-Silva, D. J. Smith, V. Meunier, M. Terrones. *An atomistic branching mechanism for carbon nanotubes: sulfur as the triggering agent*. Angew. Chem. Int. Ed. 47, 2948-2953, 2008

-
- ⁵⁴ A.K. Geim, K.S. Novoselov. *The rise of graphene*. Nature Materials 6, 183-191, 2007
- ⁵⁵ J.C. Meyer, A.K. Geim, M.I. Katsnelson, K.S. Novoselov, T.J. Booth, S. Roth. *The structure of suspended graphene sheets*. Nature 446, 60-63, 2007, and references therein.
- ⁵⁶ V.B. Shenoy, C.D. Reddy, A. Ramasubramaniam, Y.W. Zhang. *Edge-stress-induced warping of graphene sheets and nanoribbons*. Phys. Rev. Lett. 101, 245501, 2008
- ⁵⁷ K. Nakada, M. Fujita, G. Dresselhaus, M.S. Dresselhaus. *Edge state in graphene ribbons: nanometer size effect and edge shape dependence*. Phys. Rev. B. Vol. 54, 24, 1996
- ⁵⁸ Y.-W. Son, M.L. Cohen, S. G. Louie. *Energy gaps in graphene nanoribbons*. Phys. Rev. Lett. 97, 216803, 2006
- ⁵⁹ K.V. Bets, B.I. Yakobson. *Spontaneous twist and intrinsic instabilities of pristine graphene nanoribbons*. Nano Research 2, 161-166, 2009
- ⁶⁰ C. Berger, Z. Song, X. Li, X. Wu, N. Brown, C. Naud, D. Mayou, T. Li, J. Hass, A. N. Marchenkov, E. H. Conrad, P.N. First, W. A. de Heer. *Electronic confinement and coherence in patterned epitaxial graphene*. Science 312, 1191, 2006
- ⁶¹ A.M. Affoune, B.L.V. Prasad, A.H.Sato, T. Enoki, Y. Kaburagi, Y. Hishoyama. *Experimental evidence of a single nano-graphene*. Chem. Phys. Lett. 348, 17, 2001
- ⁶² C. Berger, Z. Song, T. Li, X. Li, A.Y. Ogbazghi, R. Feng, Z. Dai, A. N. Marchenkov, E.H. Conrad, P.N. First, W. A. de Heer. *Ultrathin epitaxial graphite: 2D electron gas properties and a route toward graphene-based nanoelectronics*. J. Phys. Chem. B 108, 19912-19916, 2004

-
- ⁶³ A. Reina, S. Thiele, X. Jia, S. Bhaviripudi, M.S. Dresselhaus, J. A. Schaefer, J. Kong. *Growth of large-area single- and bi-layer graphene by controlled carbon precipitation on polycrystalline Ni surfaces*. Nano Research 2, 509-516, 2009
- ⁶⁴ A. Reina, X. Jia, J. Ho, D. Nezich, H. Son, V. Bulovic, M.S. Dresselhaus, J. Kong. *Large area, few-layer graphene films on arbitrary substrates by chemical vapor deposition*. Nanoletters 9, 1, 30-35, 2009
- ⁶⁵ K.S. Kim, Y. Zhao, H. Jang, S.Y. Lee, J.M. Kim, K.S. Kim, J.-H. Ahn, P. Kim, J.-Y. Choi, B.H. Hong. *Large-scale pattern growth of graphene films for stretchable transparent electrodes*. Nature 457, 706, 2009
- ⁶⁶ M. Zhang, D.H. Wu, C.L. Xu, Y.F. Xu, W.K. Wang. *Ribbon-like nanostructures transformed from carbon nanotubes at high temperature and pressure*. Nano Structured Materials 10, 7, 1145-1152, 1998
- ⁶⁷ L.G. Cançado, M.A. Pimienta, B.R.A. Neves, G. Medeiros-Ribeiro, T. Enoki, Y. Kobayashi, K. Takai, K. Fukui, M.S. Dresselhaus, R. Saito, A. Jorio. *Anisotropy of the Raman spectra of nanographite ribbons*. Phys. Rev. Lett. 93, 4, 2004
- ⁶⁸ X. Li, X. Wang, L. Zhang, S. Lee, H. Dai. *Chemically derived, ultrasmooth graphene nanoribbon semiconductors*. Science 319, 1229, 2008
- ⁶⁹ P. Mahanandia, K.K. Nanda, V. Prasad, S.V. Subramanyam. *Synthesis and characterization of carbon nanoribbons and single crystal iron filled carbon nanotubes*. Materials Research Bulletin 43, 3252-3262, 2008
- ⁷⁰ J. Campos-Delgado, et. al. *Bulk production of a new form of sp^2 carbon: crystalline graphene nanoribbons*. Nanoletters 8, 9, 2773-2778, 2008
- ⁷¹ D. Wei, Y. Liu, H. Zhang, L. Huang, B. Wu, J. Chen, G. Yu. *Scalable synthesis of few-layer graphene ribbons with controlled morphologies by a template method and their applications in nanoelectromechanical switches*. J. Am. Chem. Soc. 131, 11147-11154, 2009

-
- ⁷² Y. Xiong, Y. Xie, X. Li, Z. Li. *Production of novel amorphous carbon nanostructures from ferrocene in low-temperature solution*. Carbon 42, 1447-1453, 2004
- ⁷³ Z. Kang, E. Wang, B. Mao, Z. Su, L. Gao, S. Lian, L. Xu. *Controllable fabrication of carbon nanotube and nanobelt with a polyoxometalate-assisted mild hydrothermal process*. J. Am. Chem. Soc. 127, 6534-6535, 2005
- ⁷⁴ L. Tapasztó, G. Dobrik, P. Lambin, L. P. Biró. *Tailoring the atomic structure of graphene nanoribbons by scanning tunneling microscope lithography*. Nature Nanotechnology 3, 397, 2008
- ⁷⁵ A. G. Cano-Márquez, F. J. Rodríguez-Macías, J. Campos-Delgado, C.G. Espinosa-González, F. Tristán-López, D. Ramírez-González, D. A. Cullen, D.J. Smith, M. Terrones, Y.I. Vega-Cantú. *ExMWNTs: graphene sheets and ribbons produced by lithium intercalation and exfoliation of carbon nanotubes*. Nanoletters 9, 4, 1527-1533, 2009
- ⁷⁶ D. V. Kosynkin, A.L. Higginbotham, A. Sinitskii, J.R. Lomeda, A. Dimiev, B.C. Price, J.M. Tour. *Longitudinal unzipping of carbon nanotubes to form graphene nanoribbons*. Nature 458, 2009
- ⁷⁷ L. Jiao, L. Zhang, X. Wang, G. Diankov, H. Dai. *Narrow graphene nanoribbons from carbon nanotubes*. Nature 458, 2009
- ⁷⁸ N.G. Chopra, L.X. Benedict, V.H. Crespi, M.L. Cohen, S.G. Louie, A. Zettl. *Fully collapsed carbon nanotubes*. Nature 377, 135-138, 1995
- ⁷⁹ M.-F. Yu, O. Lourie, M.J. Dyer, K. Moloni, T.F. Kelly, R.S. Ruoff. *Strength and breaking mechanism of multiwalled carbon nanotubes under tensile load*. Science 287, 637-640, 2000
- ⁸⁰ H.R. Gutiérrez, U.J. Kim, P.C. Eklund. *Thermal conversion of bundled carbon nanotubes into graphitic ribbons*. Nanoletters 5, 11, 2195-2201, 2005

- ⁸¹ C.-T. Lin, T.-H. Chen, T.-S. Chin, C.-Y. Lee, H.-T. Chiu. *Quasi two-dimensional carbon nanobelts synthesized using a template method*. Carbon 46, 741-746, 2008
- ⁸² M. Motta, A. Moisala, I.A. Kinloch, A.H. Windle. *High performance fibres from 'dog bone' carbon nanotubes*. Advanced Materials 19, 3721-3726, 2007

2. Production of doped single-wall carbon nanotubes using the aerosol pyrolysis technique

The synthesis of carbon nanostructures, in particular single-wall carbon nanotubes, has been achieved through different techniques, the most popular are: arc discharge, laser ablation, and pyrolysis of hydrocarbons (see Appendix A).

Thermolysis or pyrolysis of hydrocarbons (e.g. methane, benzene, acetylene, naphthalene, ethylene, etc.) and of carbon monoxide in the presence of metal catalysts (e.g. Co, Ni, Fe, Pt, and Pd deposited on substrates such as silicon, graphite or silica) at high temperatures (>600 °C) yields graphite filaments, carbon nanofibers and nanotubes. The hydrocarbon pyrolysis process is also known as chemical vapor deposition (CVD)¹.

The growth of single-wall carbon nanotubes (SWNTs) requires a catalytic particle present during the synthesis; some groups have developed methods to deposit catalytic nanoparticles over substrates for CVD production of SWNTs.

However, an alternative method of providing metal particles as catalysts during the CVD reaction is through the floating-catalyst-method, in which organometallic compounds (nickelocene (NiCp₂), cobaltocene (CoCp₂), ferrocene (FeCp₂)) are mixed with alcohols or hydrocarbons^{2,3}. This method allows the production of SWNTs in a single-step process, although it presents disadvantages too, like the low yield and by-products (metal nanoparticles) embedded in the SWNT material.

2.1 Description of the synthesis method, materials and equipment

At IPICYT, the technique used to produce SWNTs is aerosol-assisted-CVD at atmospheric pressure, based on the decomposition of ferrocene-ethanol solutions (where the decomposition of ferrocene provides the catalytic iron particles).

The equipment used for aerosol production is an ultrasonic sprayer, which consists of a glass container where the solution is placed; it contains a piezoelectric plugged into a variable frequency power supply that enables us to tune the

2.1 Description of the synthesis method, materials and equipment

frequency of vibration in order to generate a vapor cloud of the solution. A special piece of glass connects the glass container to an end of a quartz tube placed inside a tubular furnace (as depicted in Figure 2.1), the other end of the quartz tube is connected to a condenser and an acetone trap for gas release.

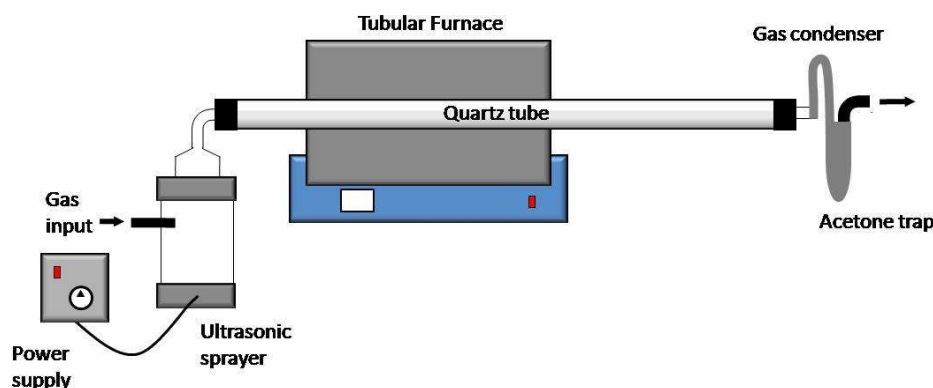


Figure 2.1 Diagram of the experimental setting used in the synthesis of single-wall carbon nanotubes

During the experiment the furnace is set to the desired temperature and an inert atmosphere is maintained by flowing Ar gas or an Ar-H (95 % - 5 %) gas mixture.

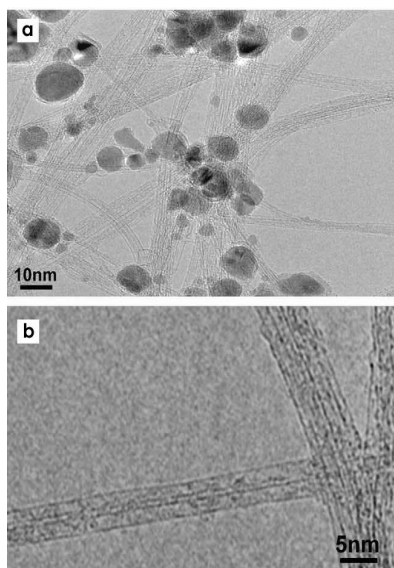


Figure 2.2 a) and b) representative TEM images of CVD-produced pristine SWNTs at IPICYT. Adapted from Reference 3.

Intense research carried out at IPICYT by preceding peers allowed us to know the optimal parameters for SWNTs production. A concentration of 1.25 wt. % of ferrocene in ethanol at 950 °C in an argon atmosphere (1.2 l/min) for 30 minutes, yields the best sample according to Lupu and co-workers³ (see Figure 2.2).

The SWNTs are deposited in the zone outside the furnace, where an important temperature gradient is found.

After the synthesis, the quartz tube is carefully disconnected and taken out of the tubular furnace; a metal tool is used to extract the material from the tube walls, as illustrated in Reference 3.

2.2 CVD production of doped single-wall carbon nanotubes

Tailoring the electronic structure of materials by adding impurities is long known by the semiconductor industry. P-type and n-type doping of carbon nanotubes is possible if we substitute carbon atoms with other atomic species containing less or more electrons, respectively.

The most common dopants of carbon nanotubes have been boron^{4,5,6,7} and nitrogen^{8,9,10,11,12,13}, which are first neighbors of carbon, in the III and V groups in the periodic table, respectively.

Nitrogen doping in multi-wall carbon nanotubes (MWNTs) induces the so-called “bamboo-like” morphologies⁵⁻¹⁰ and theoretical calculations of substitutional nitrogen doping in single-wall carbon nanotubes (SWNTs) have revealed a different electronic structure, by introducing donor-like features into the conduction band⁹. The production of N-doped SWNTs has been achieved by arc discharge¹¹ and through CVD by adding benzylamine to a ferrocene-ethanol solution¹³. In this work we demonstrate the use of an alternative precursor (pyrazine) to synthesize nitrogen-doped SWNTs.

In the literature we can find experimental reports related to phosphorous-nitrogen hetero-doping of multi-wall carbon nanotubes¹⁴. Theoretically, the substitutional doping of SWNTs by phosphorous atoms is energetically possible¹⁵ and in this section we will describe the experimental conditions to synthesize phosphorous-doped SWNTs¹⁶.

Silicon doping of fullerenes¹⁷ and hetero-fullerene¹⁸ structures was reported experimentally in the late 90's. The incorporation of silicon species in the hexagonal lattice of SWNTs was proposed theoretically by Baierle *et. al.* in 2001¹⁹. These calculations showed that substitutional silicon-doping of SWNTs introduces

donor-like states above the Fermi level. To the best of our knowledge, the synthesis of Si-doped SWNTs has not been reported hitherto.

The role of sulfur in the CVD synthesis of carbon structures has been investigated and it seems to have a major effect on the catalytic activity of iron. It increases the production of carbon fibers²⁰, enhances the synthesis of DWNTs²¹ and it is extremely important in the production of carbon nanotube fibers produced by A.H. Windle and co-workers^{22,23}.

In this section we will describe the CVD-synthesis of SWNTs in the presence of sulfur, nitrogen, phosphorous and silicon as doping species.

We will present the results of an electron microscopy characterization, which allowed us to image the produced SWNTs and by-products, and of Raman spectroscopy characterization, which through the RBM signal confirmed the presence of SWNTs in each of the experiments performed. Some chemical analysis techniques were used, like electron energy loss spectroscopy (EELS), energy dispersive X-ray analysis (EDX).

Although the expected doping level in our samples is below the detection limit of most elemental analysis techniques (e.g. <1 at. %), we will use the sensitivity of Raman spectroscopy to probe electronic changes induced by the introduction of foreign atoms in the hexagonal carbon network through the careful inspection of the G' band spectra of the synthesized materials. The appearance of the G'_{Def} peak, induced by negatively charged defects, and its relative intensity compared to the G'_{Pris} peak ($I_{G'_{Def}}/I_{G'_{Pris}}$) will provide an insight into the effect of the doping atoms within the samples²⁴. A comparative detailed analysis will indicate the effects of the different doping precursors in SWNTs.

We use an aerosol-assisted CVD method with a floating catalyst based on ferrocene (Fe(C₅H₅)₂), ethanol (C₂H₅OH) solutions; and we introduce the doping element by means of an organic compound containing it (hereafter such compound will be called the precursor compound).

We designed several experiments motivated by the work of Villalpando-Paez *et al.*¹³ and we have also reproduced their results of nitrogen-doped SWNTs using benzylamine as a precursor.

The precursors were chosen based on their physical properties (melting point and most of all, good solubility in ethanol). Table 2.1 describes the chemical structure and physical properties of the precursors that we worked with.

For each of the specific doping elements a solution of ferrocene ($\text{Fe}(\text{C}_5\text{H}_5)_2$), ethanol ($\text{C}_2\text{H}_5\text{OH}$) and the precursor compound was prepared, and for each precursor several concentrations were tried.

The concentration of ferrocene (as source of iron) was kept constant for all of the experiments reported here, at 1.25 % by weight. An aerosol of the solution was generated using the ultrasonic sprayer.

Argon (or an Ar 95 % - H 5 % mixture) was used as a carrier gas inside a quartz tube to direct the aerosol to the hot zone of a tubular furnace operated at 950 °C (during heating and cooling down the gas flow rate was set to 0.2 l/min). The flow rate for each experiment is specified in Table 2.2.

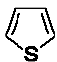
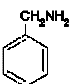
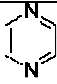
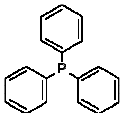
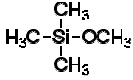
Compound name	Chemical Structure	Formula	Physical form	m.p.	b.p.
Thiophene		$\text{C}_4\text{H}_4\text{S}$	liquid	-38°C	84°C
Benzylamine		$\text{C}_7\text{H}_7\text{NH}_2$	liquid	10°C	185°C
Pyrazine		$\text{C}_4\text{H}_4\text{N}_2$	solid	50-56 °C	115-116 °C
Triphenylphosphine		$(\text{C}_6\text{H}_5)_3\text{P}$	solid	79-81°C	377°C
Methoxytrimethylsilane		$\text{CH}_3\text{OSi}(\text{CH}_3)_3$	liquid		57-58°C

Table 2.1 Chemical structure, formula and physical properties of the precursor compounds used in the doping experiments (Data extracted from the MSDS at www.sigmaaldrich.com)

After 30 minutes the aerosol generator was turned off, the system was allowed to cool down to room temperature and the quartz tube was taken out of the furnace. A web-like material containing SWNTs and by-products was collected from the zone outside the furnace.

Nitrogen-doped (N-doped) SWNTs were synthesized reproducing the results reported by Villalpando-Paez and co-workers¹³ using benzylamine ($C_7H_7NH_2$) as N precursor in the solution at concentrations of 7 wt. % and 11 wt. %. Pyrazine ($C_4H_4N_2$) was also used as N precursor at concentrations of 0.5 wt. %, 1 wt. %, 1.5 wt. % and 2.5 wt. %.

Phosphorous was inserted to the system using triphenylphosphine ($P(C_6H_5)_3$) at concentrations of 0.1 wt. %, 0.15 wt. %, 0.2 wt. % and 0.25 wt. %.

The production of SWNTs in the presence of silicon was achieved by adding different concentrations of methoxytrimethylsilane ($CH_3OSi(CH_3)_3$) as Si precursor. The concentrations used were 0.05 wt. %, 0.1 wt. % and 0.2 wt. %.

In the case of sulfur, we used thiophene (C_4H_4S) as precursor compound at concentrations of 0.1 wt. %, 0.12 wt. %, 0.15 wt. % and 0.25 wt. %.

The conditions (temperature, carrier gas and flow rate) for the different experiments are summarized in Table 2.2.

Doping element	Precursor compound	Concentration (% by weight)	Synthesis temperature	Duration	Carrier gas	Flow rate
S	Thiophene C_4H_4S	0.1, 0.12, 0.15, 0.25	950 °C	30 min	Ar	1.2 l/min
N	Benzylamine $C_7H_7NH_2$	3, 7, 11	950 °C	30 min	Ar	1.2 l/min
N	Pyrazine $C_4H_4N_2$	0.5, 1, 1.5, 2.5	950 °C	30 min	Ar-H	1.2 l/min
P	Triphenylphosphine $P(C_6H_5)_3$	0.1, 0.15, 0.2, 0.25	950 °C	30 min	Ar-H	0.8 l/min
Si	Methoxytrimethylsilane $CH_3OSi(CH_3)_3$	0.05, 0.1, 0.2	950 °C	30 min	Ar	0.6 l/min

Table 2.2 Summary of the precursor compounds and experimental conditions used in the synthesis of SWNTs in the presence of sulfur, nitrogen, phosphorous and silicon

It is worth mentioning that the incorporation of thiophene (even at the lowest concentration) changed radically the macroscopic appearance of the collected material. For pristine nanotubes, the web-like material containing SWNTs is blackish and very fragile, and its extraction from the quartz tube is a delicate task. When we add thiophene to the ethanol-ferrocene solution, the resulting material is darker, more abundant and less fragile.

We point out that the nitrogen- and phosphorous- doped materials did not show remarkable macroscopic differences from their pristine counterparts.

On the contrary, the collected materials that resulted from MTMS addition, showed a very different appearance. The overall color changed to gray tones and the material became more flake-like and less web-like.

2.3 Characterization of CVD-produced doped SWNTs

The electron microscopy characterization of the materials was carried out using a scanning electron microscope (FEI XL-30 SFEG-STEM) operated at 10-15 kV and a transmission electron microscopy (TEM) was performed on a FEI TECNAI F30 STWIN operated at 300 kV and a (ASU microscope).

The samples were mounted on carbon tape for SEM observation and prepared on copper grids for STEM and TEM observation. Elemental composition techniques, such as energy dispersive X-ray analysis (EDX) and electron energy loss spectroscopy (EELS), were also used to supplement the electron microscopy characterization.

Micro-Raman spectroscopy measurements of the bulk samples were recorded at room temperature using a Renishaw InVia equipment. The spectra were recorded with an Ar line $\lambda=514.5$ nm ($E_{\text{laser}}=2.41$ eV) and a He-Ne $\lambda=633$ nm ($E_{\text{laser}}=1.95$ eV) at a power ~ 0.3 mW in a back-scattering geometry using a 100x objective lens to focus the laser beam, using the facilities at LINAN. Analysis of spectra recorded with many laser excitation energies was carried out at the Raman Laboratory of Carbon Nanotubes at MIT facilities ($\lambda=532$ nm, $\lambda=647$ nm and $\lambda=676$ nm), and at the Raman Laboratory of the Universidade Federal de Minas Gerais (UFMG) in

Brazil (mapping of the RBMs of the phosphorous-doped samples). No less than three measurements were recorded per sample, the spectra shown here are the resulting averages. The sample was mounted on a double-sided scotch tape fixed on corning glass, and no further preparation of the sample was required.

2. 3. 1 Electron microscopy characterization

Sulfur case

Our microscopy characterization revealed that experiments with low concentration of thiophene (0.1 - 0.25 wt. %) produced arrays of SWNTs entangled with short, twisted multi-wall nanotube-like nanostructures, see Figures 2.3 a-d.

In Figure 2.3e, a high magnification SEM image of the by-products is shown. The high-angle annular dark-field scanning transmission electron microscopy (HAADF-STEM) image of the same area, depicted in Figure 2.3f, reveals a high contrast at the tips, suggesting a metallic nature of nanoparticles present at the tips of the short tubes.

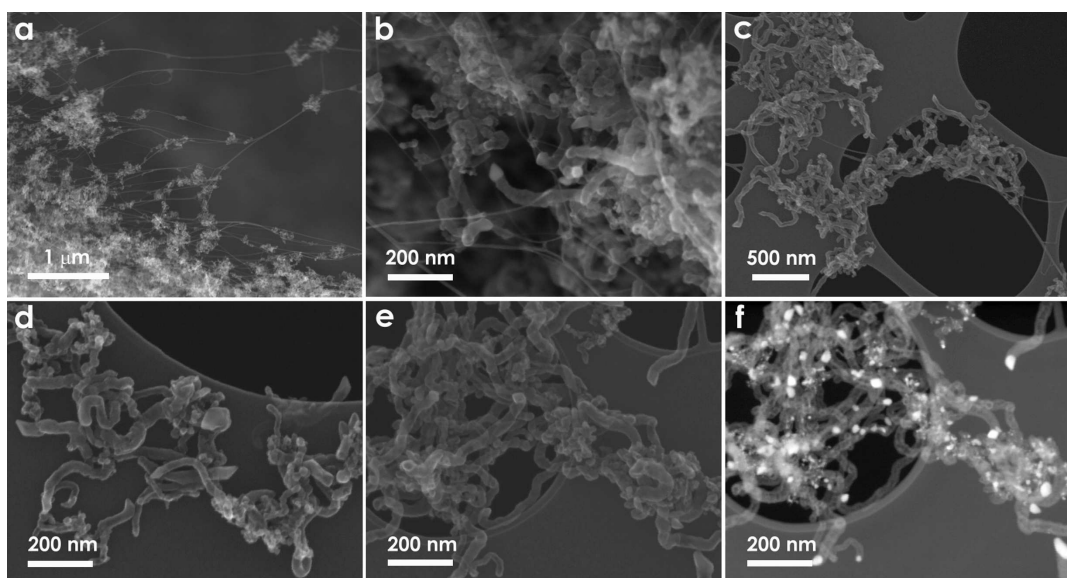


Figure 2.3 SEM images of the material synthesized with thiophene at a) 0.15 wt. % and b) - f) 0.1 wt. %. In figures a), b) and c), single-wall nanotubes appear like threads accompanied by short, twisted MWNT-like nanostructures. These by-products are imaged at higher resolution in d) and e). A HAADF-STEM image of e) is shown in f).

In order to investigate the structure of the by-products we performed HRTEM of the materials. We can find a low magnification TEM image in Figure 2.4a, where we confirm the metallic nature of the nanoparticles at the tips of the short tubes by a higher contrast image.

In Figure 2.4b an image of two SWNTs and by-products is presented. A multi-wall nanotube is shown at high magnification in Figure 2.4c, we can see that the body of the tube is constituted of graphitic layers (not very crystalline) arranged in a compartment bamboo-like structure catalyzed by the metallic particle at the tip. A better resolved image of the walls of a different short tube is shown in Figure 2.4d.

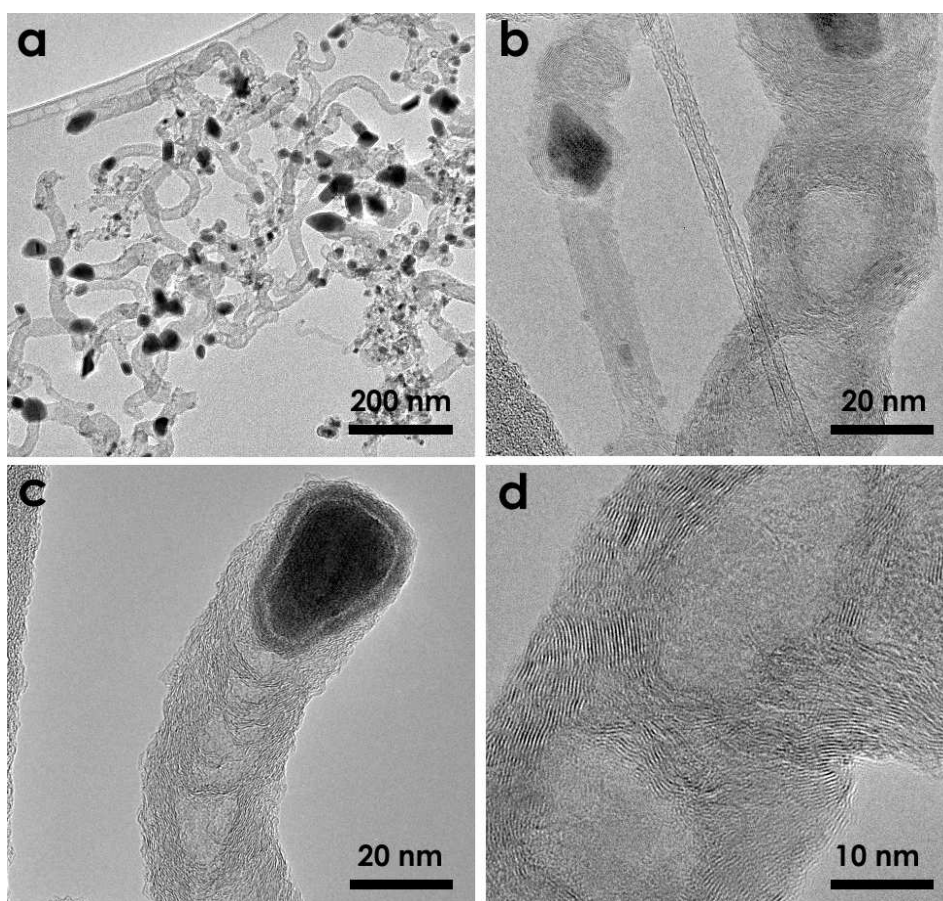


Figure 2.4 TEM images of the material synthesized with thiophene. 0.12 wt. % thiophene (a and c) and 0.25 wt. % of thiophene (b and d).

The carbon composition of the walls was confirmed by high resolution energy dispersive X-rays (EDX) point measurements on the wall of the tubes, see Figure

2.5. In this figure we can also see an EDX point measurement at the metallic tip, the signal reveals that the nanoparticle is composed of Fe, S and O. The Cu signal detected comes from the copper grid that the sample was mounted on.

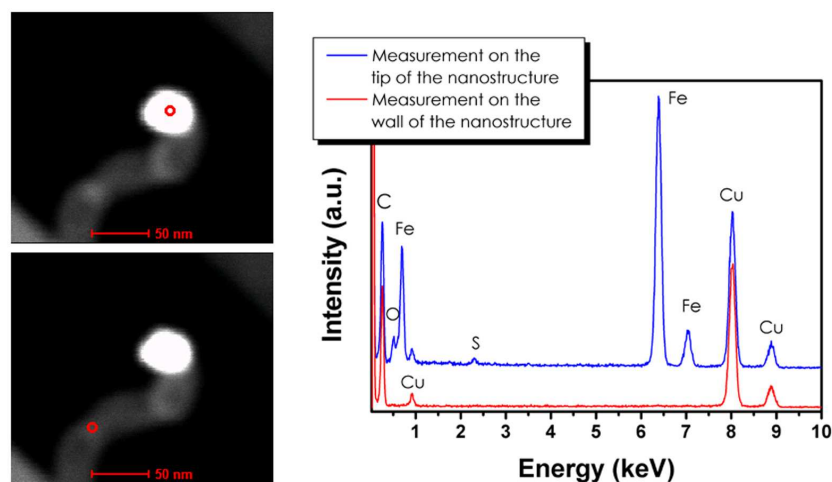


Figure 2.5 High resolution EDX point measurements of a short multi-wall nanotube. At the left, HAADF-STEM images depicting the zone of measurement by a small-red circle; at the right, the plot of the corresponding recorded spectra.

Nitrogen case

We reproduced the results published by Villalpando and co-workers¹³, where benzylamine was used as precursor compound for nitrogen-doped SWNTs.

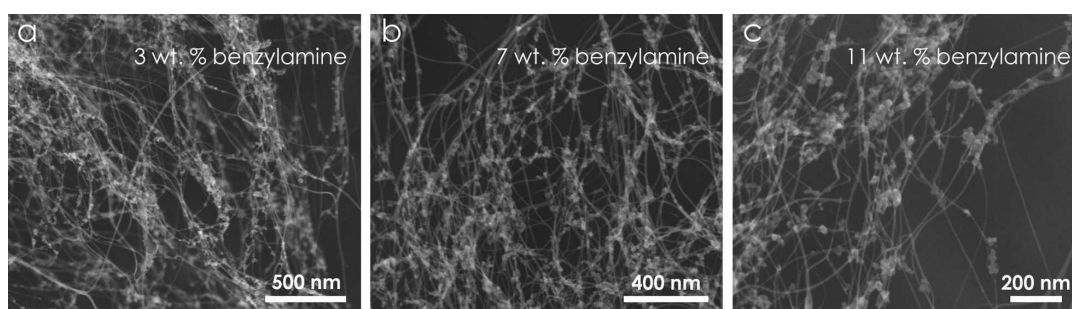


Figure 2.6 SEM images of nitrogen-doped SWNTs produced with benzylamine at concentrations of a) 3 wt. %, b) 7 wt. %, and c) 11 wt. %.

Our SEM observations (Figure 2.6) show that the materials synthesized with benzylamine contain arrays of SWNTs and small metallic nanoparticles, the

amount of these metallic nanoparticles present in the sample increase with increasing benzylamine concentration and the yield of the produced SWNT decreases.

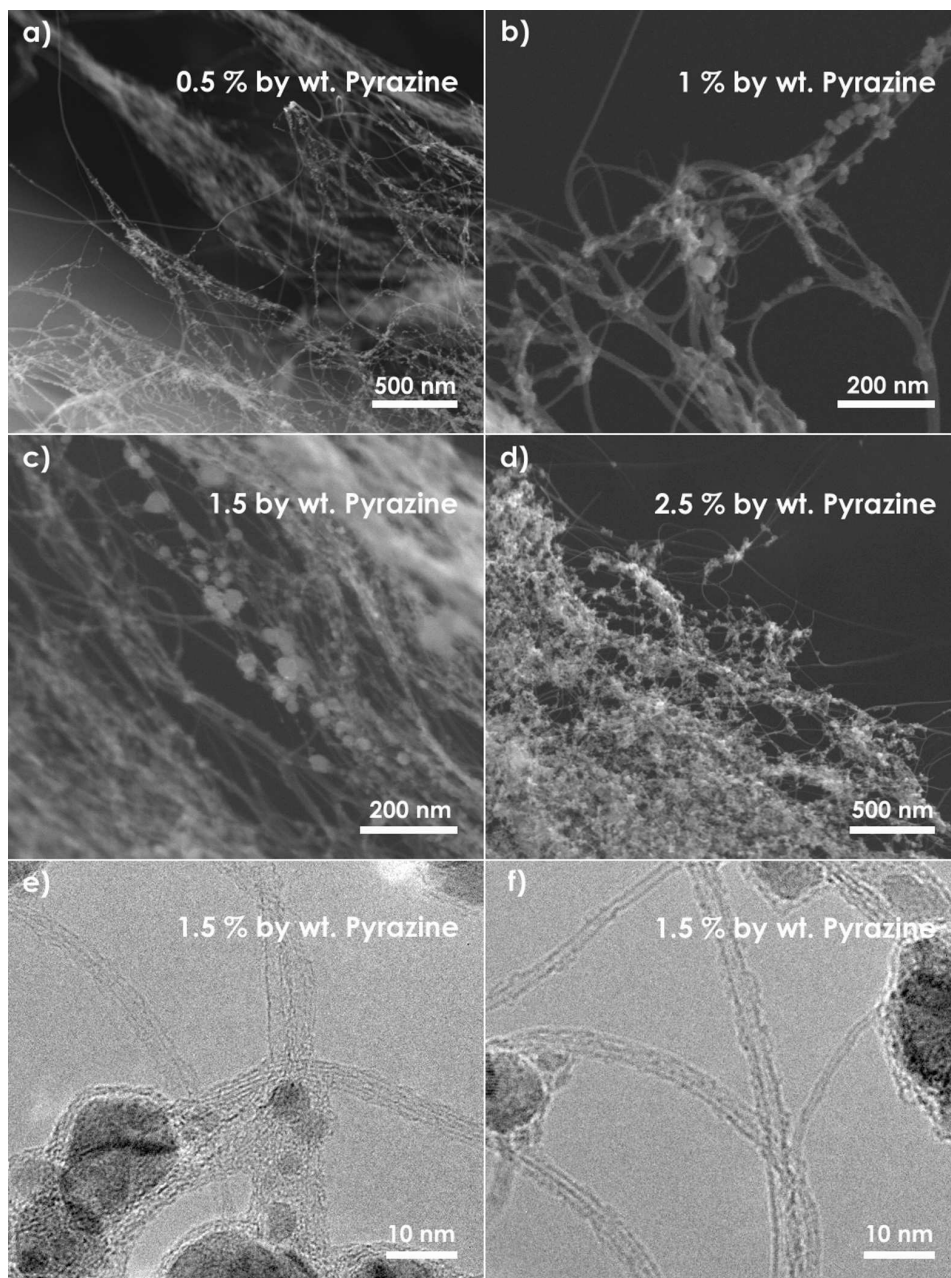


Figure 2.7 a), b), c) and d) SEM images of SWNTs synthesized in the presence of pyrazine at concentrations of 0.5, 1, 1.5 and 2.5 % by wt., respectively. e) and f) two different spots on the material at 1.5 % by wt. of pyrazine imaged by HRTEM.

Recent extensive characterization of these samples through X-ray photoelectron spectroscopy (XPS)²⁵ has revealed that the synthesized N-doped nanotubes exhibit a maximum concentration at 0.3 at. % of N. Therefore, EDX or EELS are not able to detect such low concentrations and Raman characterization becomes the most sensitive tool to observe the doping effects in SWNTs.

For the production of N-doped SWNTs another precursor was used: pyrazine. The chemical formula of pyrazine (see Table 2.1) indicates that it contains two atoms of nitrogen per molecule; we believe that the doping of SWNTs could be more effective due to this immediate availability of N atoms during the synthesis; see Figure 2.20. The introduction of this compound in the synthesis of SWNTs led to the production of nanotubes and iron nanoparticles very similar to the un-doped counterpart (see Figure 2.2 and 2.7).

Although elemental analysis techniques were used to try to detect N traces in the walls of the tubes, we failed to find a N signal in any of the samples. However Raman spectroscopy will prove the tubes were doped.

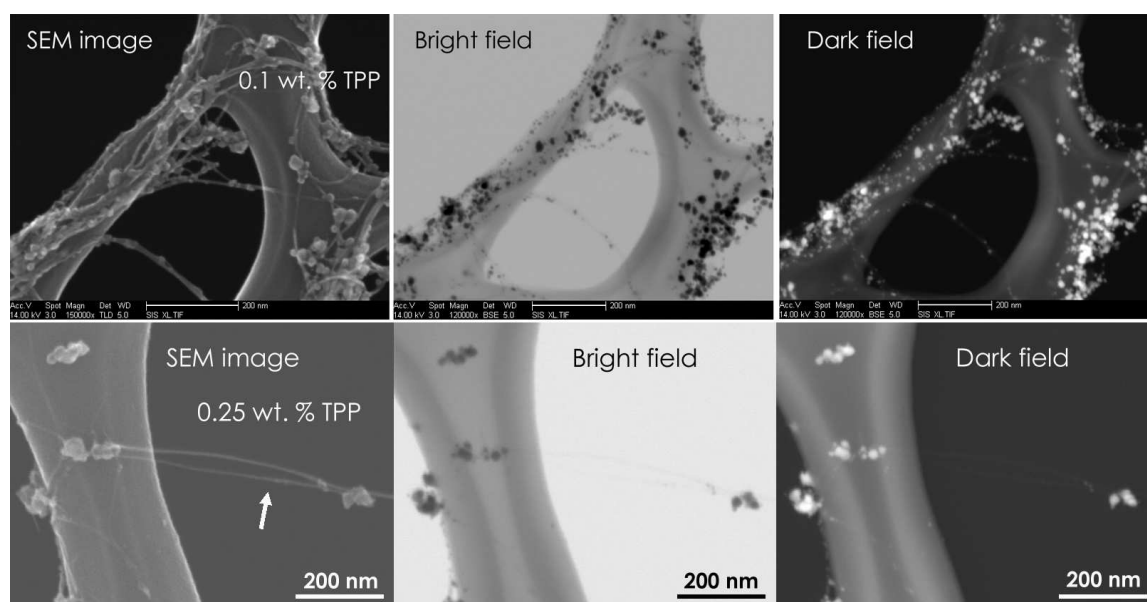


Figure 2.8 SEM images (left panels), and bright and dark field STEM images (center and right panels) of the samples synthesized with triphenylphosphine.

Phosphorus case

The introduction of triphenylphosphine (TPP) led to the synthesis of SWNTs and nanoparticles as depicted in Figure 2.8, where SEM and STEM images of the samples synthesized with 0.1 % by wt. (top panels) and 0.25 % by wt. (bottom panels) of TPP are presented.

The nanoparticles entangled with the nanotubes, observed in the SEM images (left panels of Figure 2.8) are clearly heavier when imaged by bright field and HAADF STEM (center and left panels in figure 2.8, respectively), showing more contrast than the nanotubes composed of only carbon.

The metallicity of the particles was further confirmed by the observation of lattice fringes during TEM observation (images not shown here).

A high proportion of SWNTs present in this sample confirms the catalytic nature of the present metallic nanoparticles.

More details on the morphology of the synthesized materials at the four different concentrations can be observed on Figure 2.9, where SEM and TEM images of the materials are presented.

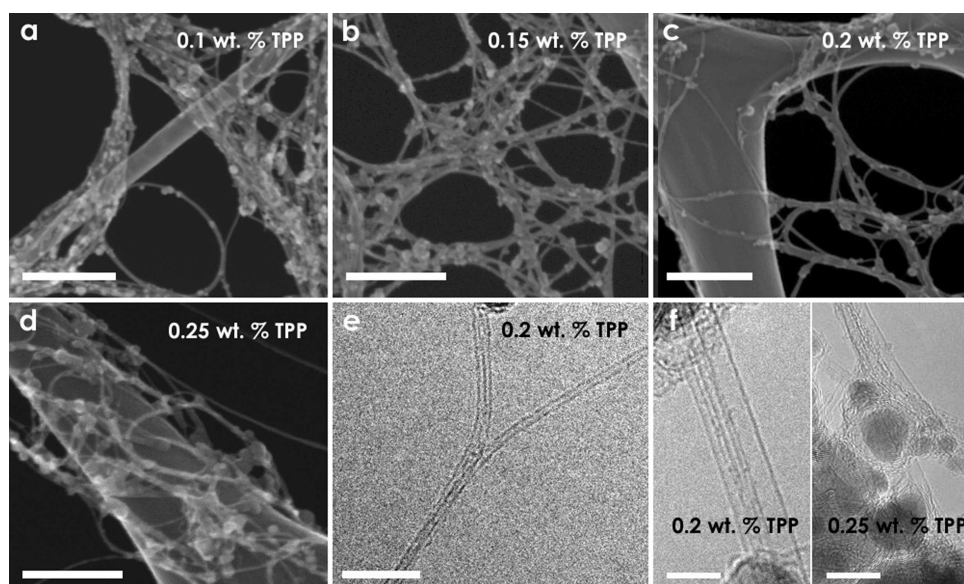


Figure 2.9 SEM images of SWNTs and by-products deposited over copper grids synthesized with a) 0.1 % by wt., b) 0.15 % by wt., c) 0.2 % by wt. and d) 0.25 % by wt. of TPP; d) and e) TEM images of the material synthesized with 0.2 and 0.25 % by weight. Scale bars in a) - d) represent 200 nm. Scale bars in e) and f) represent 10 nm and 5 nm, respectively.

SEM images of the different concentrations are included in Figure 2.9 a-d, a good quality of the material and a low proportion of by-products are observed in all of these cases. Figures 2.9 e and f show HRTEM images of the 0.2 wt. % and 0.25 wt. % samples, we can confirm a good quality and crystallinity of the produced nanotubes.

Silicon case

Experiments with methoxytrimethylsilane (MTMS) resulted in the formation of SWNT bundles mixed with by-products, which were further analyzed to determine their morphology and composition.

Figure 2.10 shows representative TEM images of the nanostructures produced. At the lowest concentration of MTMS (0.05 % by wt.) catalytic Fe nanoparticles were present, embedded in the SWNT bundles, very similar to the pristine material (see Figure 2.2 and Figures 2.10 a and b).

Figure 2.10c shows the material synthesized at 0.1 % by wt. of MTMS, the upper panel depicts a low magnification image and the lower one a higher magnification image. Using this MTMS concentration, the SWNTs appear with spherical nanoparticles clearly embedded in a dense matrix, our elemental composition analysis helped to investigate the nature of the matrix and spherical nanostructures.

EELS and HAADF STEM (high-angle annular dark-field scanning transmission electron microscopy) analysis were performed on this sample. The single-wall carbon nanotubes and bundles were very difficult to image in the HAADF mode. They have very low contrast compared to the SiO_2 and Fe in the matrix. The contrast had to be minimized in order to see the tubes, which is why the matrix material appears washed out in the images of Figure 2.11. The point spectra shown on the left panels of Figure 2.11 confirm the tubes are carbon (284 eV). Linescans were not possible due to nanotube movement. We gathered EELS spectra from single points on several tubes and never found a Si signal (99 eV). If there is any Si in the tubes, it is below the detectable limit of EELS.

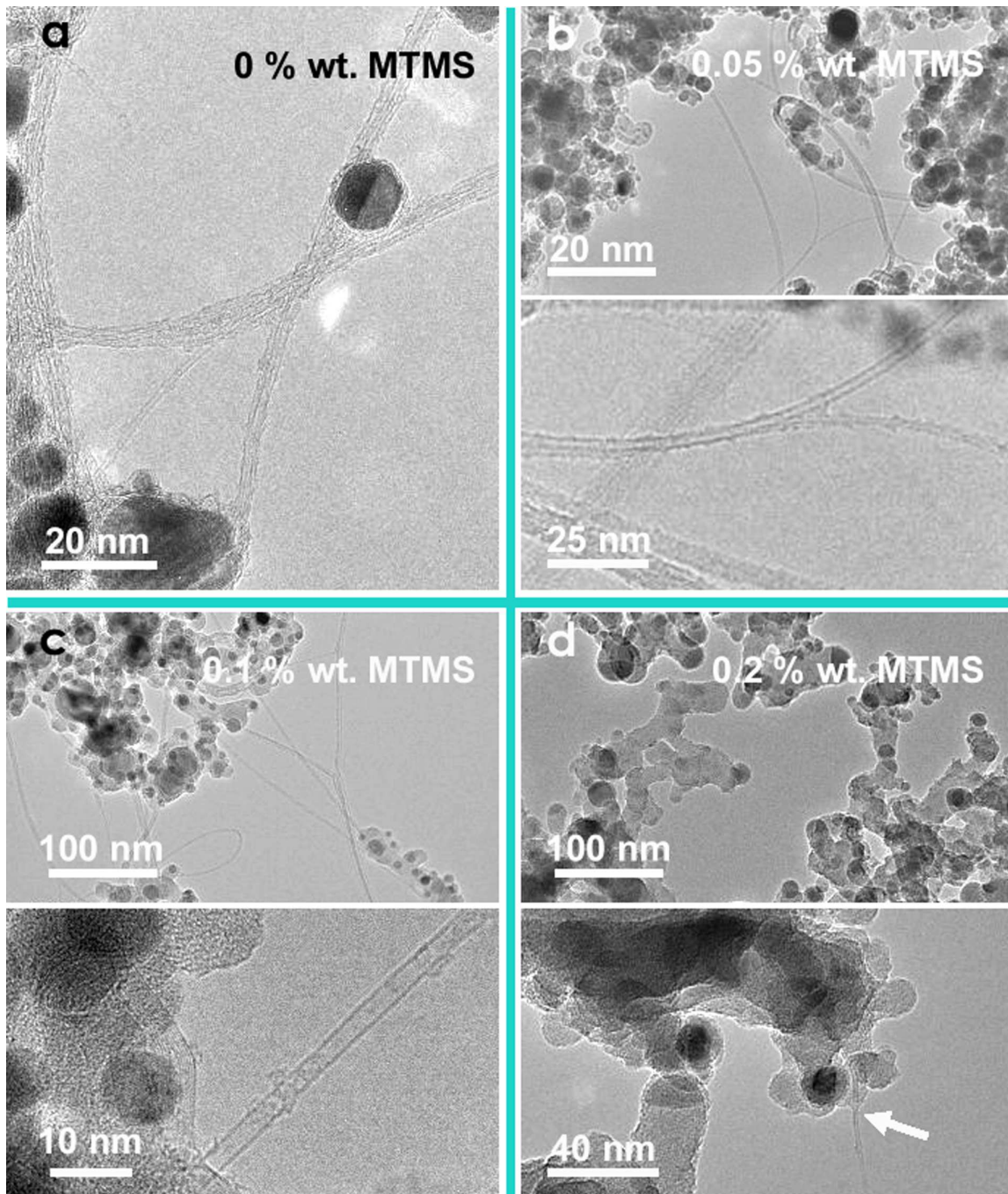


Figure 2.10 High Resolution Transmission Electron Micrographs of SWNTs produced with different concentrations of methoxytrimethylsilane, a) pristine SWNTs, b) 0.05 % by weight, c) 0.1 % by weight and d) 0.2 % by weight, the arrow in the low panel points to a SWNT embedded in the by-products. In b), c) and d) the upper panels contain low magnification images and the lower panels contain higher magnification images, picturing the carbon nanotubes and the morphology of the accompanying by-products.

Analysis of the matrix material is also shown in Figure 2.11. The top spectrum at the right of the image covers the range for Si (99 eV) and C (284 eV). The bottom spectrum covers the range for O (532 eV) and Fe (708 eV). As the spectra show, the matrix is primarily Si and O. We periodically found C in the matrix, which probably belongs to carbonaceous by-products also present in the sample.

Point spectra from the bright, round particles in the matrix confirm that they are Fe. Usually weak O, Si, and C peaks also appear in the spectra, but only because the particle is sitting on or embedded in the silicon oxide matrix.

0.1 wt. % of MTMS

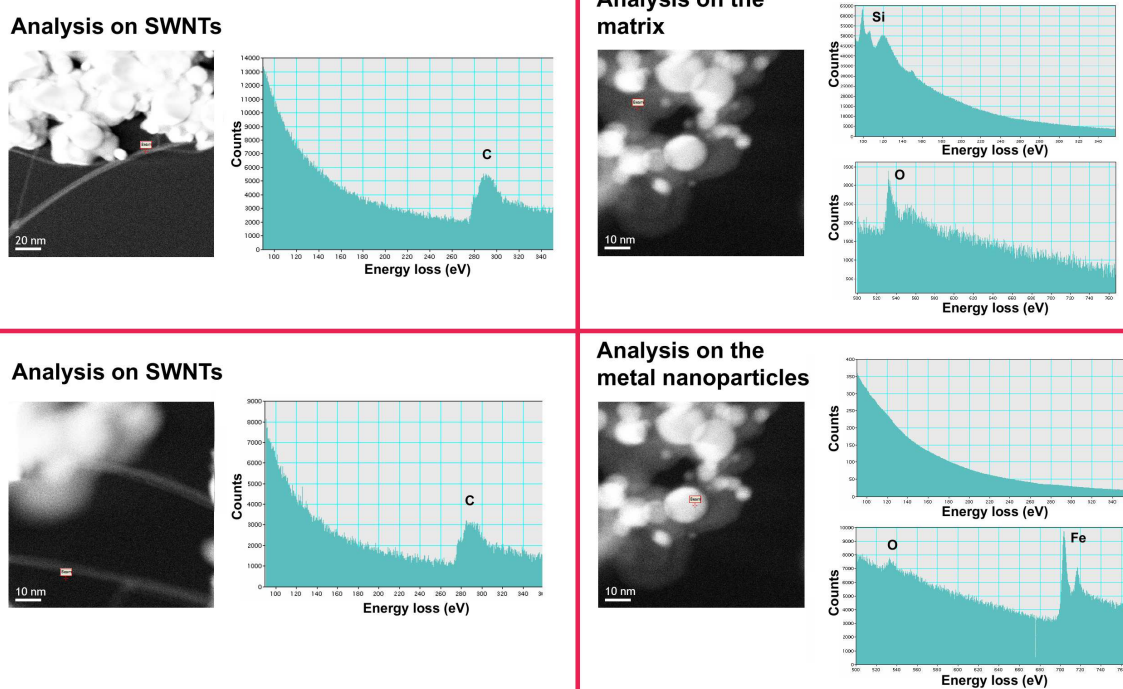


Figure 2.11 HAADF-STEM images and EELS point spectra of the sample synthesized with 0.1 wt. % of MTMS. Left panels correspond to point measurements on SWNTs. Top right panel, point measurement on the matrix, and bottom right panel, point measurement on a metal nanoparticle.

In the Fe-O spectrum below, there is also a weak O signal. There were also weak Si and C signals at this same point, but we were able to make them disappear by moving the beam to a region of the particle that wasn't over the matrix. We thus conclude that these are pure Fe particles embedded in the Si-O matrix. This is

important because for the sample synthesized with a higher MTMS concentration (0.2 wt. %), the nature of the Fe particles change.

A higher concentration of silicon (0.2 % by wt. of MTMS), promotes the formation of strikingly different nanostructures and SWNTs. In this sample, short nanorods with metallic hemi-spherical tips can be found (see Figure 2.10d). In these samples, it was difficult to find numerous SWNTs, nevertheless, in the lower panel of Figure 2.10d an individual SWNT can be observed (pointed to by an arrow) along with the by-products synthesized for this MTMS concentration. We believe that the formation of pure Fe particles, which serve as SWNT catalysts during the growth, was not favored at these experimental conditions. The formation of binary Fe-Si alloys is highly probable at this synthesis temperature; hence, the catalytic activity of Fe was reduced and thus the formation of nanotubes was not abundant.

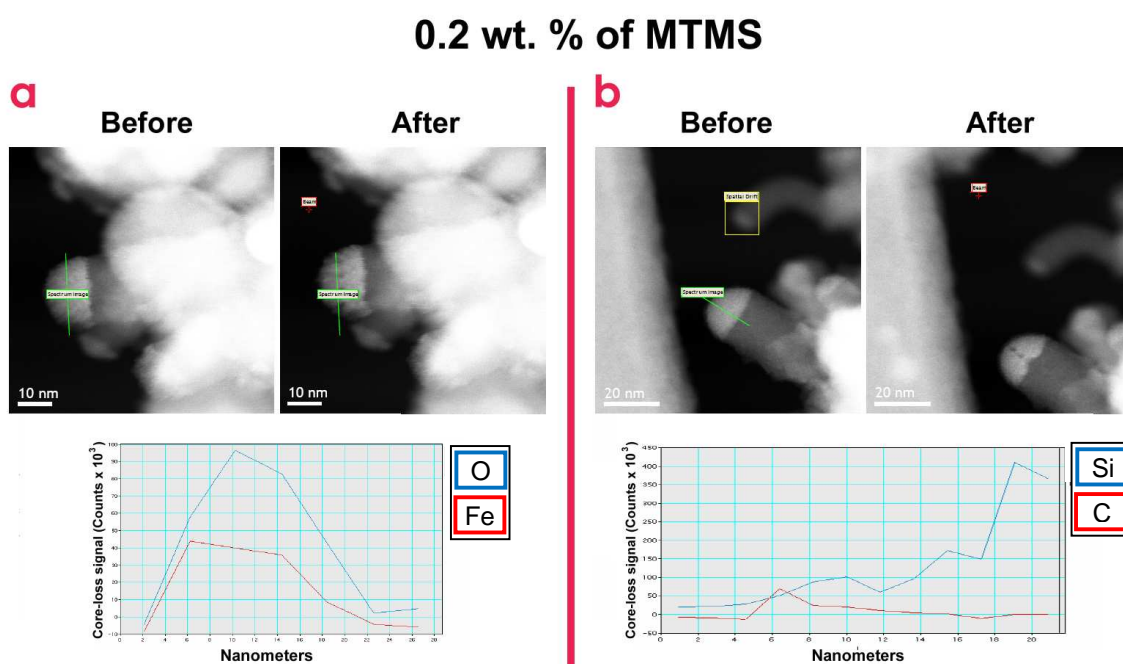


Figure 2.12 HAADF-STEM images and EELS line scans on tips of the nanorods, a) Fe-O EELS profile with before and after images, the tips are primarily Fe but they also contain a significant portion of O. b) Si-C EELS profile with before and after images. The Si signal gets progressively stronger as the beam moves from vacuum, through the metal tip, and into the matrix material. The C signal from the front of the tip is a contamination artifact and not typical of tip chemistry. The profile shows that the Fe tips contain a significant amount of Si.

However, due to the high sensitivity of Raman spectroscopy to identify SWNTs, their presence was confirmed by the observation of a RBM signal (see Figures 2.17 and 2.19).

While doing EELS and HAADF imaging, the sample was very unstable but we found a region that was relatively stable under the beam. We still observed some drift, but tried to compensate for it with the spatial drift correction in the Digital Micrograph. The matrix material is similar to that of a sample synthesized with 0.1 wt. % MTMS, except for the presence of the small rods with hemispherical tips.

We performed a few line scans on the tips; see Figure 2.12, which were marginally successful. Because of the drift, we could only do 5-8 points per scan, so the profiles are pretty rough but they still make the point. Due to the width of the EELS window, we were not able to capture the Fe and Si signals simultaneously; so on some tips we scanned for Fe and O (Figure 2.12a) , and on others we scanned for Si and C (Figure 2.12b).

The sets of images in Figure 2.12 contain EELS profiles with before and after images. The image taken after the EELS profile was captured to show drift (which in the last two cases we attempted to correct) and beam damage.

It is clear from both the image contrast and the EELS spectra that the tips contain Fe. But the tips also contain a significant amount of Si and O, and we never found a tip that was pure Fe.

Note in the images of Figure 2.12 how the beam drilled through the semi-spherical Fe particles. From our experience with imaging metals, pure Fe is relatively stable under the beam. This damage suggests intermixing of the Fe with Si and/or O.

In general, from our electron microscopy characterization two things are worth mentioning. First of all, the experiments carried out, successfully produced SWNT material synthesized in the presence of S, N, P and Si for all the concentrations reported in Table 2.2. Our second conclusion is related to the nature of the by-products. The presence of sulfur and silicon dramatically modified the morphology

and structure of the accompanying materials; while phosphorous and nitrogen did not induce changes in the morphology of the nanoparticles when comparing them to the by-products obtained in the production of pristine SWNTs.

2.3.2 Raman spectroscopy characterization

Raman spectroscopy is a technique very sensitive to the electronic structure of carbon materials. A complete appendix to the Raman spectroscopy of carbon materials is included in this work (Appendix B), in such pages the reader will find a description of the double resonance process, first and second order Raman scattering, characteristic nanotube vibrations (radial breathing mode and tangential modes), disorder induced modes and information related to the Raman analysis that will be discussed in future paragraphs.

Sulfur case

We have performed Raman scattering measurements with $E_{\text{laser}} = 2.41 \text{ eV}$ ($\lambda = 514.5 \text{ nm}$). As mentioned before, in a typical routine of Raman spectroscopy, two or three measurements are recorded per sample and the average of the spectra is reported. When doing the analysis of these samples we recorded several spectra per sample. We noticed that for the same sample the shape of the signal changed from one spot to the other. Figure 2.13 depicts spectra recorded at two different spots of the sample synthesized with 0.1 wt. % of thiophene.

In Figure 2.13a we show the spectrum of a zone where the carbon-related signal was found above 1000 cm^{-1} (D, G, D', G' and D+G bands). It is worth mentioning that at low-frequencies other modes are clearly present (see inset in Figure 2.13a). Care should be taken when assigning these modes. Since we are dealing with SWNTs, a first impulse would be to interpret them as RBM peaks. Nevertheless in the spectrum there are no other SWNT-related Raman features. For example, the high intensity of the disorder-related modes (D, D' and D+G bands) is not characteristic of SWNTs (compare to cyan line in Figure 2.13b), and we do not observe a multi-peak feature around $\sim 1580 \text{ cm}^{-1}$ originating from the quantum

confinement of the wavevector along the circumferential direction (see Appendix B). Figure 2.14a contains a plot of the RBM region with spectra of all the different concentrations of thiophene. The yellow lines are guides to the eye to show that the two main peaks are located at the same frequencies for all the concentrations ($\sim 219 \text{ cm}^{-1}$ and $\sim 285 \text{ cm}^{-1}$).

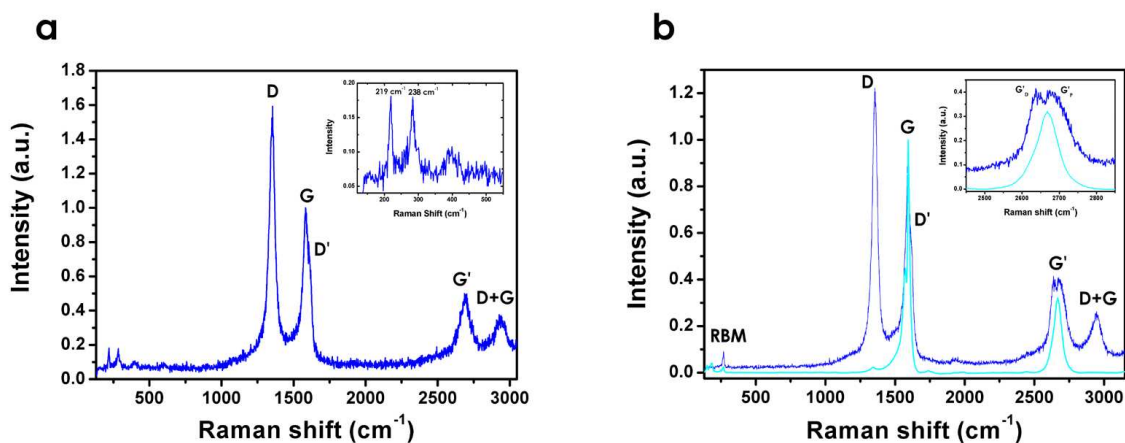


Figure 2.13 Raman spectra of material synthesized with 0.1 wt. % of thiophene. a) spectrum showing sulfur-related low frequency features (see inset) and carbon-related features (D, G, D', G' and D+ G bands). b) spectrum of nanotubes present in the sample (blue line) showing RBM signal, a detail on the G' band region is depicted in the inset. We include the spectrum of pristine SWNTs heat treated at 400 °C (cyan line) for comparison

When we analyze the RBM signal frequencies in relation to the laser excitation energy used (E_{laser}), we should be able to assign the ω_{RBM} to a certain (n,m) chirality (see Introduction). However, it is clear from Figure 2.14b that the intersection points between the green and yellow lines are deserted, indicating that no chirality is excited at this energy at those particular frequencies; hence the signal can not be attributed to resonance with carbon nanotubes.

When we correlate these results with the information obtained from the elemental composition characterization (Figure 2.5), we find that the signal at low frequencies belongs to sulfur^{26,27} (peaks around 216 cm^{-1} and 285 cm^{-1}), which is indeed present in the by-products. Thus, we conclude that the spectrum shown in Figure 2.13a has a contribution primarily from the bamboo-like multi-wall nanotubes with

metallic tips. The low crystallinity of the walls (Figure 2.4d) is responsible for the high intensity of the disorder induced modes (D, D' bands) and the sulfur content is responsible for the features found at low-frequencies.

In Figure 2.13b we plot the spectrum of a zone were contributions of SWNT and by-products can be identified from the sample with 0.1 wt. % of thiophene. Again, contribution from the carbonaceous by-products is associated with the high intensity of the D band and the presence of the D' band. However, in this spectrum a single RBM peak was found, which denotes the presence of SWNTs; besides, the splitting of the G' band (G'_{Def} and G'_{Pris} bands, see Appendix B) implies n-doping due to the presence of electron-donor substitutional sulfur atoms. Unfortunately this last conclusion can not be confirmed because we were not able to reproduce such a spectrum in other spots of the sample.

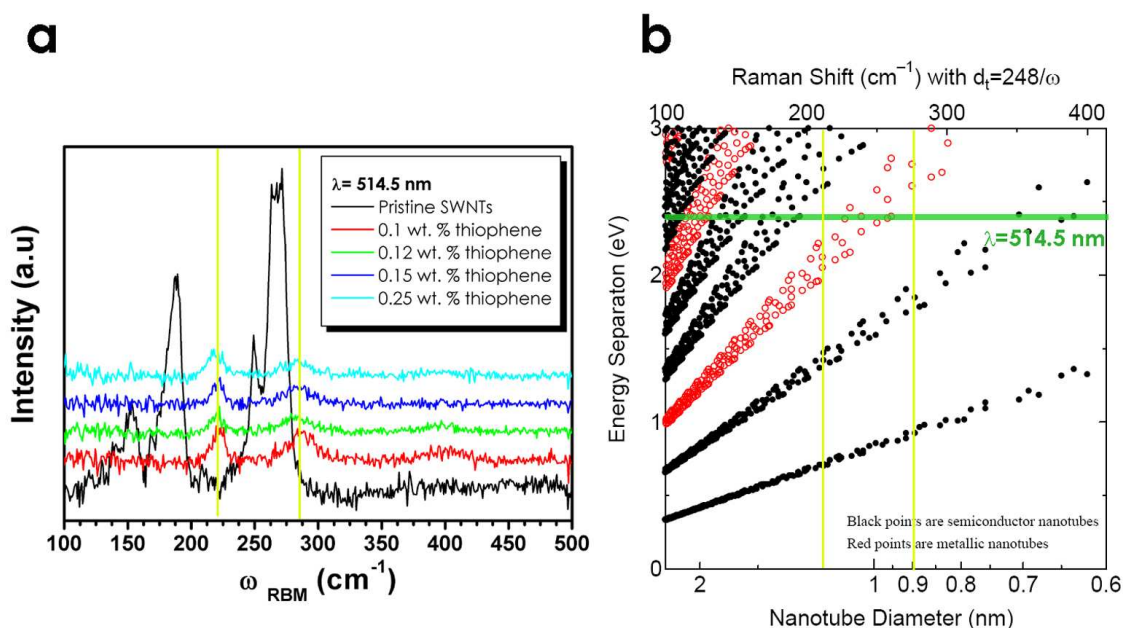


Figure 2.14 a) RBM region showing spectra of materials synthesized with thiophene, the spectrum of pristine SWNTs is also included. In this plot, the yellow lines at 219 cm^{-1} and 285 cm^{-1} highlight the position of the peaks present for all the concentrations of thiophene. b) Katarua plot²⁸, the green line is placed at 2.41 eV (energy corresponding to laser $\lambda=514.5 \text{ nm}$), the yellow lines are placed at the same frequencies as in a).

The stories for the samples with higher content of thiophene (0.12, 0.15 and 0.25 wt. %) are very similar. The gray line in Figure 2.15 represents a typical spectrum

of the 0.15 wt. % sample, where no RBM signal was found and the existing features are attributed to the other sp^2 carbons present in the sample. Note the shape of the G band, isolated in the inset, no multi-peak features are present and the D' band intensity is high, while in the pristine SWNT spectrum we find a G^- and G^+ splitting of the G band and the D' band is absent.

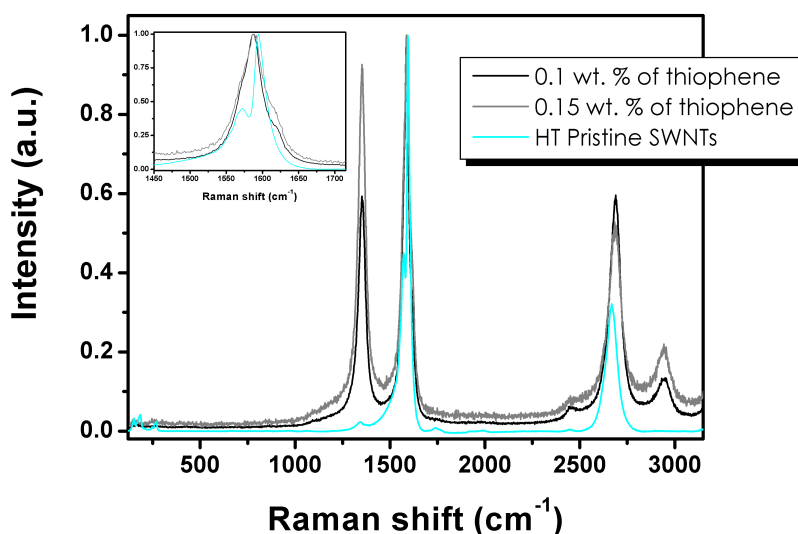


Figure 2.15 Plot of Raman spectroscopy of materials synthesized with thiophene (black and gray lines). The spectrum of pristine nanotubes is included for comparison (cyan line). A detail on the G band region is pictured in the inset.

We can conclude from the Raman analysis of the thiophene-produced samples that, although the microscopy characterization showed clearly and abundantly the presence of single-wall nanotube species, the recorded spectra did not show predominant features of SWNTs. On the contrary, the by-products signal overcame the nanotube signal, making it difficult to extract information on the effect of substitutional sulfur-doping of the single-wall carbon nanotubes.

The discussion of the Raman characterization of the rest of the doped-nanotube samples (synthesized with TPP, benzylamine, pyrazine and MTMS) will be done as a whole, since in all the cases we were able to record good Raman spectra.

The presence of SWNTs in all our materials was positively proved by electron microscopy images (see Figures 2.3 - 2.11) and by Raman spectroscopy traces, through the RBM signal.

Nitrogen, phosphorus and silicon

In Figure 2.16 we include a plot of the RBM of the samples synthesized with TPP, pyrazine, benzylamine, MTMS recorded with five different laser excitation energies: 2.41 eV ($\lambda=514$ nm), 2.33 eV ($\lambda=532$ nm), 1.96 eV ($\lambda=633$ nm), 1.91 eV ($\lambda=647$ nm), and 1.83 eV ($\lambda=676$ nm).

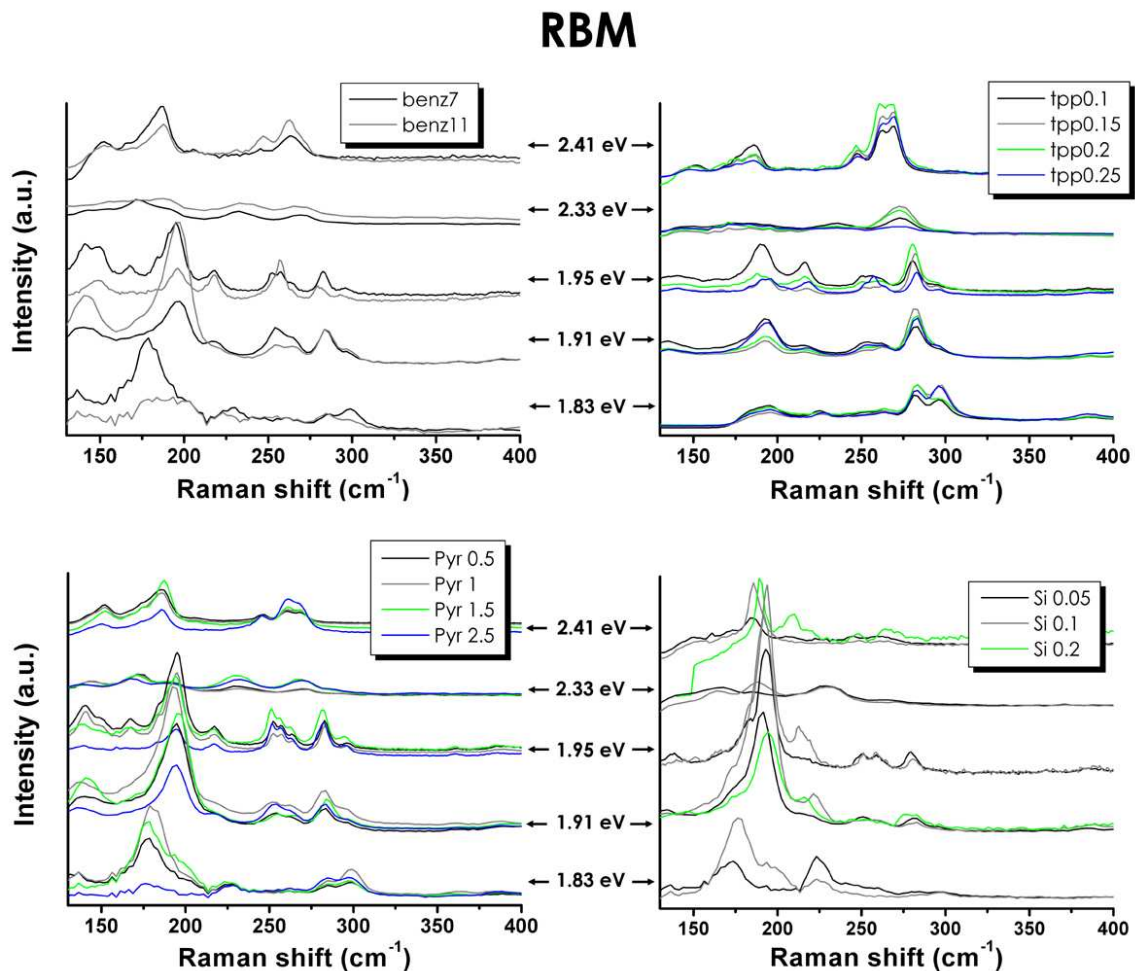


Figure 2.16 Raman radial breathing mode (RBM) spectra of the different doped samples recorded with five laser excitation energies: 2.41 eV ($\lambda=514$ nm), 2.33 eV ($\lambda=532$ nm), 1.95 eV ($\lambda=633$ nm), 1.91 eV ($\lambda=647$ nm), 1.83 eV ($\lambda=676$ nm)

It has been theoretically and experimentally demonstrated that the incorporation of heavier elements in the hexagonal carbon lattice is energetically favored in narrower nanotubes which exhibit higher radii of curvature.^{15,16,29}

In our experiments, the production of narrower nanotubes when N and Si atoms are substitutionally doping the SWNTs is illustrated in Figure 2.17, where the RBM region of the Raman spectra recorded at $E_{\text{laser}}=1.96$ eV is plotted. The red arrows help to visualize the RBM features that significantly decrease in intensity as the precursor concentration in the ferrocene-ethanol solution is increased. We could correlate this decrease to the absence of large diameter doped SWNTs.

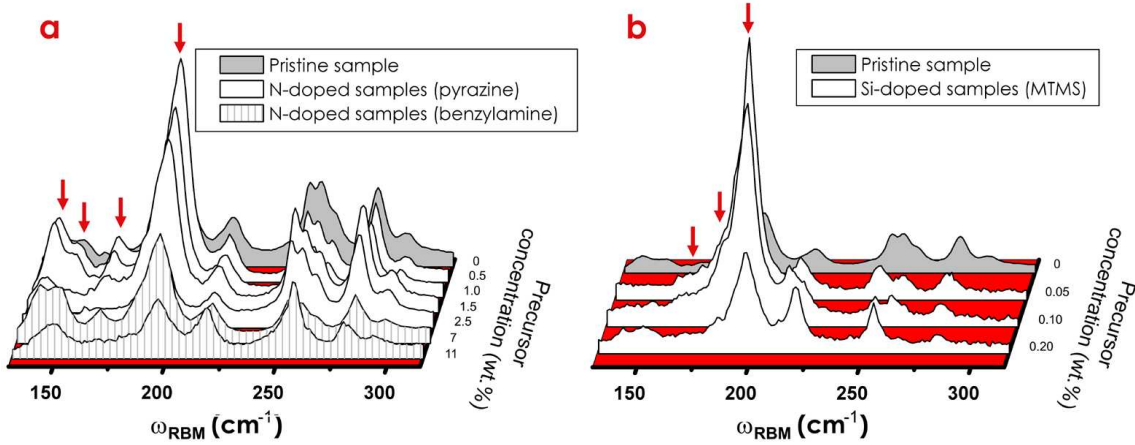


Figure 2.17 RBM spectra recorded at $E_{\text{laser}}=1.96$ eV of a) N-doped SWNTs synthesized with different concentrations of benzylamine and pyrazine and b) Si-doped SWNTs synthesized with different concentrations of MTMS. The spectra were normalized to the G band and the red arrows point to the RBM features that decrease as the precursor concentration is increased.

We carried out a many laser excitation energies study of the phosphorous-doped SWNT samples. Mapping of the RBMs as a function of the excitation laser energy was performed with excitation energies ranging from 1.61 to 2.71 eV. An Ar-Kr laser (1.91, 2.18, 2.33, 2.41, 2.47, 2.49, 2.53, 2.60, 2.62 and 2.71 eV) and a dye tunable laser (16 lines from 1.80 to 2.01 eV, 16 lines from 2.03 to 2.19 eV and 5 lines from 2.23 to 2.29 eV) were used. The RBM peak position is related to the tube diameter by

$$\omega_{\text{RBM}} = \frac{227}{d_t} \sqrt{1 + Cd_t^2} \quad (1)$$

where ω_{RBM} is the RBM frequency shift in cm^{-1} , d_t is the tube diameter in nanometers, and C is a constant factor accounting for environmental effects. By measuring the RBMs with different laser energies, it is possible to build a two-dimensional map of the RBM profiles as a function of the excitation laser energy. Figure 2.18 shows such maps in the 1.9-2.3 eV energy range for the 0, 0.1, 0.15, 0.2 and 0.25 wt. % of P-doped SWNT samples. The maps show the resonance patterns related to different $(2n+m)=\text{constant}$ families belonging to the E_{22}^{S} , E_{11}^{M} , E_{33}^{S} , transition energies, (n,m) being the nanotube indices. No ω_{RBM} or optical transition energies (E_{ii}) shift can be seen from the maps for different doping levels, thus indicating that the local nature of P doping does not change either ω_{RBM} or E_{ii} of the SWNTs.

Although the RBM Raman cross section depends on (n,m) and E_{ii} , a qualitative description of the diameter distribution of the samples can be obtained by adding all the RBM spectra for each sample, as shown in Figure 2.18f. The diameters vary from 0.7 to 2.2 nm for the different samples. However, the samples with higher doping levels (0.2 wt. % and 0.25 wt. %) have larger RBM intensities with higher RBM frequencies, meaning that either the presence of phosphorous induces the formation of tubes with smaller diameters or the relative Raman scattering of narrower tubes has been enhanced by doping.

In both cases, this result and the two-peak G' feature (see G' band analysis in future paragraphs), confirm substitutional phosphorous doping.

Finally, this accurate information on the diameter distribution, based on the ω_{RBM} analysis, was used to analyze the $\omega_{\text{G}'}$ peaks and we can rule out any diameter or resonance effects as responsible for the behavior of the $\omega_{\text{G}'_{\text{Pris}}} - \omega_{\text{G}'_{\text{Def}}}$ splitting.

The change in the RBM intensity toward high ω_{RBM} frequencies above 0.15 wt. % of TPP indeed confirms the effect shown by the $\omega_{\text{G}'}$ analysis, where doping seems to be more effective above this doping level.

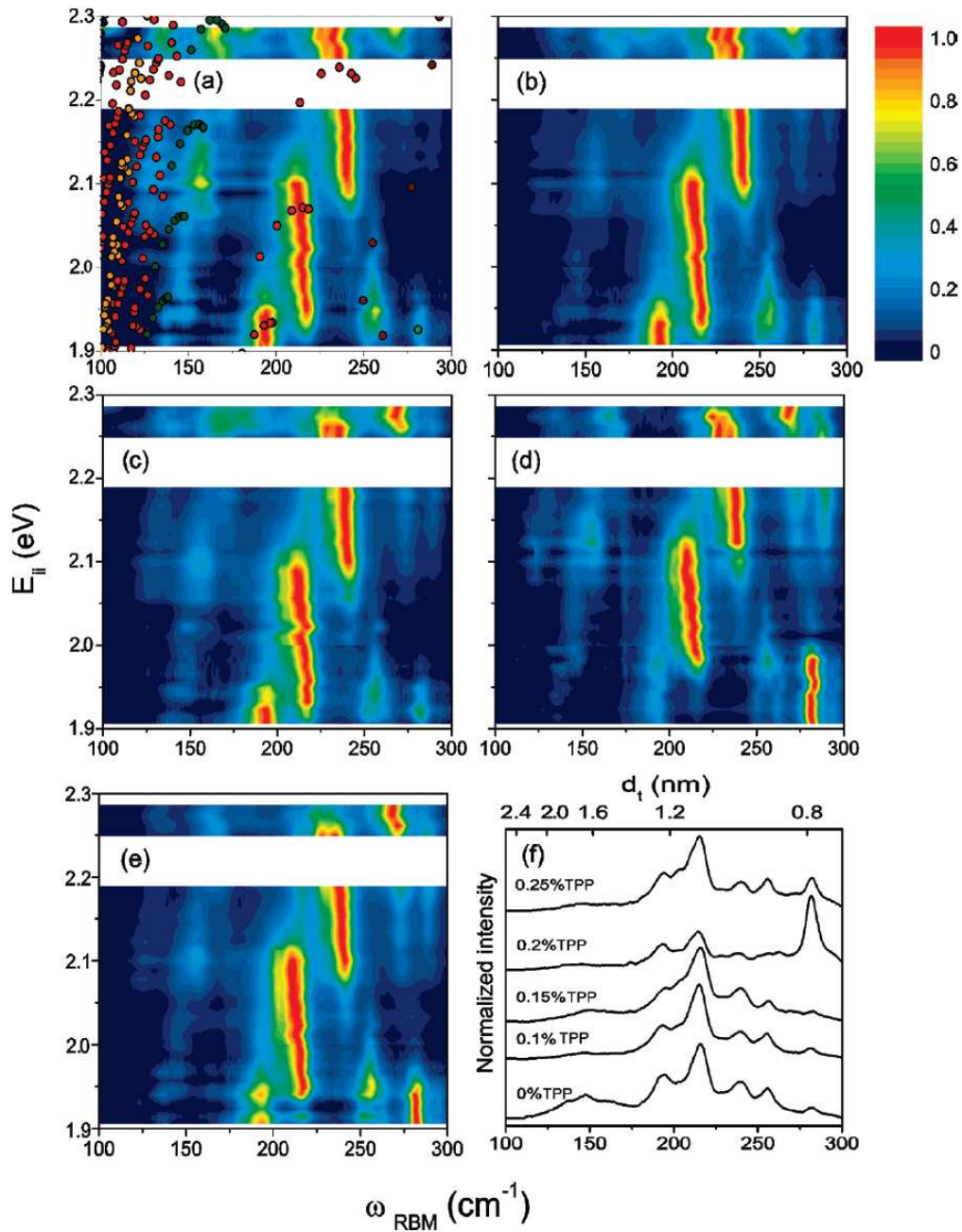


Figure 2.18 (a-e) Radial breathing mode (RBM) resonance Raman maps of the phosphorous-doped SWNT samples with 0, 0.1, 0.15, 0.2, 0.25 wt. % of TPP, respectively. The optical transmission energies (E_{ii}) were inserted on the map of the undoped sample a) to indicate the (n,m) -dependent RBM resonances by using equation (1), with the best fit to our data given by $C=0.035$. f) Diameter distribution of the samples obtained by summing all the RBM spectra measured with the different excitation laser lines. The upper x-axis was obtained by the inverse of the $\omega_{RBM}-d_t$ relation cited above.

In Figure 2.19 we include a plot of the RBM and G'-band regions, recorded at $E_{\text{laser}}=2.41$ eV, of the samples synthesized with TPP, pyrazine, benzylamine, MTMS and of pristine SWNTs annealed at 400 °C (HT Pristine). This plot reveals that SWNTs were successfully grown in the different environments and at every single concentration used. We can also note the evolution of the G'_{Def} peak as the precursor concentration is increased. This increase in intensity is quantified by means of the $I_{G'_{\text{Def}}}/I_{G'_{\text{Pris}}}$ relative intensity.

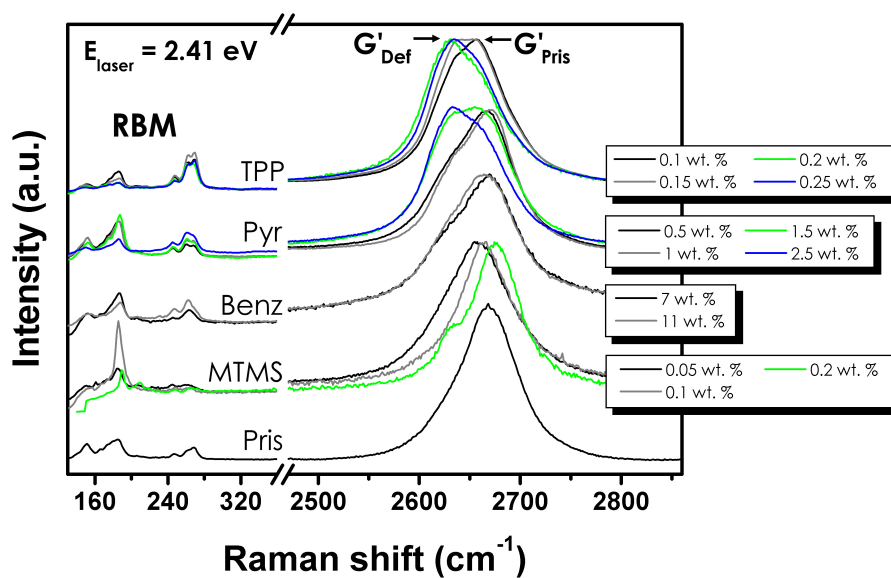


Figure 2.19 Raman spectra of the synthesized materials, acquired with $E_{\text{laser}} = 2.41$ eV, showing the RBM and G' band regions. The spectrum of pristine SWNTs annealed at 400 °C as described in Reference 15 is included for comparison

We have performed a Raman spectroscopy comparative analysis, based on the $I_{G'_{\text{Def}}}/I_{G'_{\text{Pris}}}$ relative intensity, to quantify the effect of doping on the electronic and vibrational structure of SWNTs, relatively among the different precursors.

A two-peak Lorentzian fitting of the G' band of all the spectra recorded at $E_{\text{laser}}=2.41$ eV was carried out, according to previous studies^{16,30}. This procedure has to be made with care, since the G'_{Pris} frequency depends on tube diameter, which changes upon doping. The ratio of the relative intensities of the G'_{Def} band

and G'_P band ($I_{G'_{Def}}/I_{G'_{Pris}}$) was computed, the resulting values are plotted in Figure 2.20 as a function of doping atoms available per carbon atom during the synthesis in the precursor-ferrocene-ethanol solution.

For all of the precursors, an increase in the number of doping atoms per carbon atom available in the synthesis results in the increase of the $I_{G'_{Def}}/I_{G'_{Pris}}$ relative intensity, suggesting higher doping levels as we increase the precursor concentration.

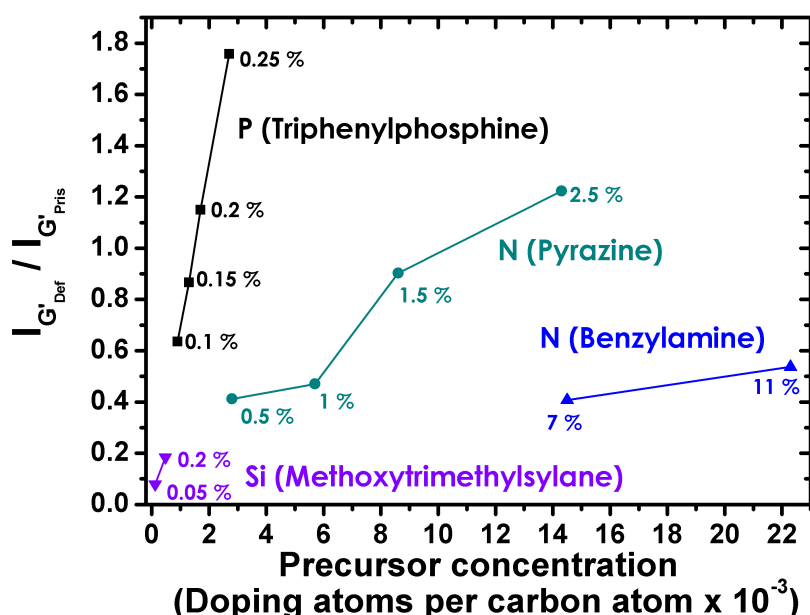


Figure 2.20 Plot of the $I_{G'_{Def}}/I_{G'_{Pris}}$ relative intensities as a function of doping atoms (P, N and Si) per carbon atoms introduced in the synthesis environment (calculated from the precursor concentration. Such concentrations are also included next to each corresponding symbol), the solid squares represent the set of P-doped samples synthesized with triphenylphosphine, the solid circles and solid triangles represent the N-doped samples synthesized with pyrazine and benzylamine, respectively, and the solid inverse-triangles stand for the Si-doped materials synthesized using methoxytrimethylsilane as a precursor.

The lowest $I_{G'_{Def}}/I_{G'_{Pris}}$ relative intensity values were obtained for the Si-doped samples. However, these are also the samples synthesized with the lowest amount of doping atoms per carbon atom. We are confident that higher Si doping will

result from the use of higher concentrations of MTMS during the synthesis. However, other experimental conditions should be varied to avoid the suppression of the catalytic effect of Fe when Fe-Si alloys are formed. We believe that the increase of flow rates and temperatures could speed up the reactions and promote the SWNT formation while the catalyst particle is active.

On the contrary, although the highest concentration of benzylamine used in this work (11 wt. %) provided the highest number of doping atoms per carbon atom during the synthesis, the $I_{G'_{Def}}/I_{G'_{Pris}}$ relative intensity values are below those of 1.5 wt. % and 2.5 wt. % of pyrazine, which proves a more efficient N-doping when pyrazine is used as the nitrogen precursor.

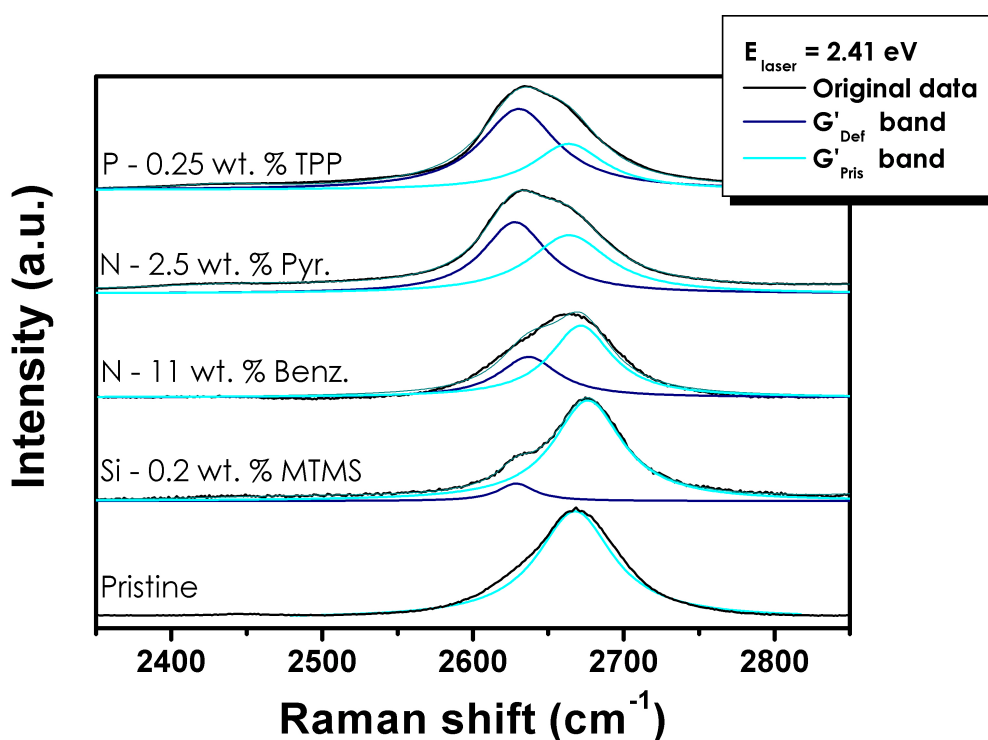


Figure 2.21 G' band Raman spectra and the corresponding Lorentzian two-peak-fitting of the G' band (G'_{Def} and G'_{Pris} bands) of the samples with maximum $I_{G'_{Def}}/I_{G'_{Pris}}$ relative intensities for each precursor (corresponding to the highest concentrations used in this work). The spectrum of annealed pristine SWNTs at 400 °C is included for comparison. The blue and cyan lines represent the Lorentzian fitting of the G'_{Def} and G'_{Pris} bands, respectively.

XPS analysis of N-doped benzylamine SWNTs proved that the content of nitrogen reaches a maximum at 0.3 at. %, and our Raman results indicate that pyrazine-produced N-doped nanotubes could surpass this limit. A careful XPS characterization of our pyrazine N-doped materials is underway.

Further inspection of this figure leads us to conclude that the most efficient doping is attributed to phosphorous, since the amount of P atoms available per C atom is relatively small (below the amount of N atoms available) and still the $I_{G'_{Def}}/I_{G'_{Pris}}$ relative intensity shows its highest values.

However, it is not yet clear whether the $I_{G'_{Def}}/I_{G'_{Pris}}$ relative intensities can be directly compared for different dopants. As discussed in Ref. 16 and 25, different atoms disturb the SWNT lattice differently. To address this point we selected the samples with highest $I_{G'_{Def}}/I_{G'_{Pris}}$ relative intensities from Figure 2.20 (i.e. 0.25 wt. % of TPP, 2.5 wt. % of pyrazine, 11 wt. % of benzylamine and 0.2 % of MTMS).

In Figure 2.21 we show the Raman spectra in the G' band region of the above mentioned samples and their corresponding fitting. In this graph it is very easy to visualize the G'_{Def} bands (blue lines) and the G'_{Pris} bands (cyan lines). As we go from the pristine sample to the P-doped sample we see an increase in intensity of the G'_{Def} band, directly measured in the $I_{G'_{Def}}/I_{G'_{Pris}}$ relative intensities.

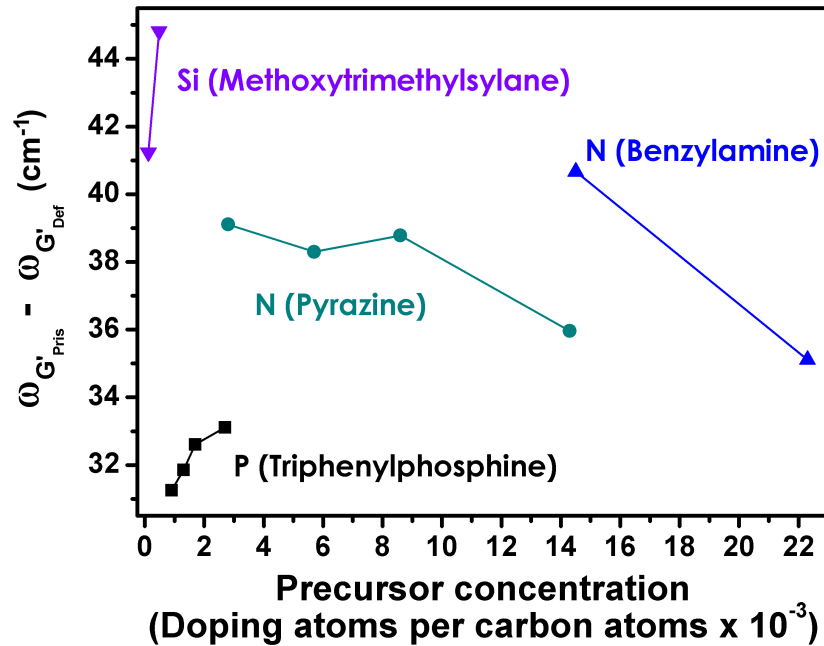


Figure 2.22 Plot corresponding to the G' band splitting ($\omega_{G'_{Pris}} - \omega_{G'_{Def}}$) of the P-, N- and Si-doped SWNTs as a function of precursor concentration.

The information of the fitted spectra was further used to calculate the frequency splitting $\omega_{G'_{Pris}} - \omega_{G'_{Def}}$ between the two G' peaks for the doped samples, see Figure 2.22. From this figure it is clear that there is a range of values particular to each doping element. For phosphorous the splitting values are in the range of ~ 31 - 33 cm^{-1} , for nitrogen the splitting values are in the range ~ 35 - 40 cm^{-1} and Si reported the highest values, in the range of ~ 41 - 45 cm^{-1} . These results suggest that the G' band splitting is more related to the nature of doping than to the doping level.

2. 4 Conclusions

The synthesis of single-wall carbon nanotubes in sulfur, nitrogen, phosphorous and silicon environments was achieved via aerosol-assisted-CVD.

Precursors containing the target doping element were mixed in ethanol-ferrocene solutions at different concentrations, thiophene for sulfur incorporation, triphenylphosphine was used in the case of phosphorous, methoxytrimethylsilane was used as a silicon precursor, and benzylamine and pyrazine were used as nitrogen precursors.

Electron microscopy of the samples as well as RBM Raman signals confirmed the presence of carbon nanotubes in the synthesized materials.

Electron microscopy analysis revealed that most of the materials consisted of doped SWNTs entangled with metallic nanoparticles. In the case of S and Si, interesting morphologies were formed, such as short bamboo-like MWNTs and Si nanorods with metallic tips, respectively.

In particular, the incorporation of sulfur promoted a very dense formation of by-products. The enhancement of the catalytic activity of iron by sulfur addition was confirmed through the copious presence of short, twisted bamboo-like MWNTs along with SWNTs. We believe that the modification of the experimental parameters (e.g. reduction of ferrocene concentration) could yield to the optimization of S-doped SWNTs.

Our RBM analysis showed that as the doping precursor was increased in the sprayer solution, narrower diameter tubes were favored. The latter is consistent with theoretical calculations indicating that dopants of heavier elements embedded in the hexagonal carbon lattice are more energetically favored in narrower tubes, exhibiting higher radii of curvature.

We have used the $I_{G'_{Def}}/I_{G'_{Pris}}$ relative intensities as a direct doping index for the amount of N, P and Si incorporated in the structure. Our samples synthesized with sulfur could not be included in this analysis due to the poor quality of the recorded Raman spectra. Hence we do not have strong evidence for the sulfur doping of SWNTs. Si-doped samples showed low $I_{G'_{Def}}/I_{G'_{Pris}}$ relative intensity values which are directly related to the small amount of silicon atoms available per carbon atoms during the synthesis. Nitrogen doping is more effective when pyrazine is used instead of benzylamine and phosphorous doping is very effective even at low TPP concentrations.

Our Raman records show that the increasing precursor concentration leads to higher doping levels, increasing the $I_{G'_{Def}}/I_{G'_{Pris}}$ relative intensities, and that the frequency splitting $\omega_{G'_{Pris}} - \omega_{G'_{Def}}$ between the two G' peaks depends more on the doping element than on the doping amount. We are carrying out more synthesis experiments in order to have a higher number of samples per doping element, to be able to run Raman spectroscopy measurements and elucidate the nature of the G' band splitting peculiarities observed in this work.

2.5 Related Articles

- 1 . J. Campos-Delgado, I.O. Maciel, D. A. Cullen, D. Smith, A. Jorio, M.A. Pimenta, H. Terrones, M. Terrones. *Chemical vapor deposition synthesis of N-, P-, and Si- doped single-wall carbon nanotubes* (Submitted to ACS Nano).
- 2 . A.L. Elías, P. Ayala, A. Zamudio, M. Grobosch, E. Cruz-Silva, J.M. Romo-Herrera, J. Campos-Delgado, H. Terrones, T. Pichler, M. Terrones. *Spectroscopic characterization of N-doped single-walled carbon nanotube strands: a X-ray photoelectron spectroscopy and Raman study*. Journal of Nanoscience and Nanotechnology (in press).
- 3 . I.O. Maciel, M.A. Pimenta, M. Terrones, H. Terrones, J. Campos-Delgado, A. Jorio. *The two peaks G' band in carbon nanotubes*. Phys. Stat. Sol. (b) 245, 10, 2197-2200, 2008
- 4 . I.O. Maciel, N. Anderson, M.A. Pimenta, A. Hartschuh, H. Qian, M. Terrones, H. Terrones, J. Campos-Delgado, A. Rao, L. Novotny, A. Jorio. *Electron and phonon renormalization near charged defects in carbon nanotubes*. Nature Materials 7, 878-883, 2008
- 5 . I.O. Maciel, J. Campos-Delgado, E. Cruz-Silva, M.A. Pimenta, B.G. Sumpter, V. Meunier, F. López-Urías, E. Muñoz-Sandoval, H. Terrones, M. Terrones, A. Jorio. *Synthesis, electronic structure, and Raman scattering of phosphorus-doped single-wall carbon nanotubes*. Nanoletters 9,6, 2267-2272, 2009

2.6 References

- ¹ M. Terrones. *Carbon nanotubes: synthesis and properties, electronic devices and other emerging applications*. Int. Mat. Rev. 49, 6, 325-377, 2004
- ² C.N.R. Rao, A. Govindaraj, R. Sen, B.C. Satishkumar. *Synthesis of multi-walled and single-walled nanotubes, aligned-nanotube bundles and nanorods by employing organometallic precursors*. Mat. Res. Innovat. 2, 128-141, 1998
- ³ F. Lupo, J.A. Rodríguez-Manzo, A. Zamudio, A.L. Elías, Y.A. Kim, T. Hayashi, M. Muramatsu, R. Kamalakaran, H. Terrones, M. Endo, M. Rühle, M. Terrones. *Pyrolytic synthesis of long strands of large diameter single-walled carbon nanotubes at atmospheric pressure in the absence of sulphur and hydrogen*. Chem. Phys. Lett. 410, 384-390, 2005
- ⁴ X. Blase, J.-C. Charlier, A. De Vita, R. Car, Ph. Redlich, M Terrones, W.K. Hsu, H. Terrones, D.L. Carroll, P.M. Ajayan. *Boron-mediated growth of long helicity-selected carbon nanotubes*. Phys. Rev. Lett. 83, 24, 5078- 5081, 1999
- ⁵ K. McGuire, N. Gothard, P.L.Gai, M.S. Dresselhaus, G. Sumanasekera, A.M. Rao. *Synthesis and Raman characterization of boron-doped single-walled carbon nanotubes*. Carbon 43, 219-227, 2005
- ⁶ W. Han, Y. Bando, K. Kurashima, T. Sato. *Boron-doped carbon nanotubes prepared through a substitution reaction*. Chem. Phys. Lett. 299, 368-373, 1999
- ⁷ D. Goldberg, Y. Bando, W. Han, K. Kurashima, T. Sato. *Single-walled B-doped carbon, B/N-doped carbon and BN nanotubes synthesized from single-walled carbon nanotubes through a substitution reaction*. Chem. Phys. Lett. 308, 337-342, 1999
- ⁸ R. Sen, B.C. Satishkumar, A. Govindaraj, K.R. Harikumar, G. Raina, J.-P. Zhang, A.K. Cheetham, C.N.R. Rao. *B-C-N, C-N and B-N nanotubes produced by the pyrolysis of precursor molecules over Co catalysts*. Chem. Phys. Lett. 287, 671-676, 1998

-
- ⁹ M. Terrones, P.M. Ajayan, F. Banhart, X. Blase, D.L. Carroll, J.C. Charlier, R. Czerw, B. Foley, N. Brobert, R. Kamalakaran, P. Kohler-Redlich, M. Rühle, T. Seeger, H. Terrones. *N-doping and coalescence of carbon nanotubes: synthesis and electronic properties*. Appl. Phys. A 74, 355-361, 2002
- ¹⁰ R. Droppa Jr., P. Hammer, A.C.M. Carvalho, M.C. dos Santos, F. Alvarez. *Incorporation of nitrogen in carbon nanotubes*. Journal of Non-Crystalline Solids 299-302, 874-879, 2002
- ¹¹ M. Glerup, M. Castignolles, M. Holzinger, G. Hug, A. Loiseau, P. Bernier. *Synthesis of highly nitrogen-doped multi-walled carbon nanotubes*. Chem. Commun. 2542-2543, 2003
- ¹² M. Glerup, J. Steinmetz, D. Samaille, O. Stéphan, S. Enouz, A. Loiseau, S. Roth, P. Bernier. *Synthesis of N-doped SWNT using the arc-discharge procedure*. Chem. Phys. Lett. 238, 193-197, 2004
- ¹³ F. Villalpando-Paez, A. Zamudio, A.L. Elias, H.Son, E.B. Barros, S.G. Chou, Y.A. Kim, H. Muramatsu, T. Hayashi, J. Kong, H. Terrones, G. Dresselhaus, M. Endo, M. Terrones, M.S. Dresselhaus. *Synthesis and characterization of long strands of nitrogen-doped single-walled carbon nanotubes*. Chem. Phys. Lett. 424, 345-352, 2006
- ¹⁴ E. Cruz-Silva, D.A. Cullen, L. Gu, J.M. Romo-Herrera, E. Muñoz-Sandoval, F. López-Urias, B.G. Sumpter, V. Meunier, J.-C. Charlier, D. J. Smith, H. Terrones, M. Terrones. *Heterodoped nanotubes: theory, synthesis, and characterization of phosphorus-nitrogen doped multiwalled carbon nanotubes*. ACS Nano 2, 3, 441-448, 2008
- ¹⁵ B. G. Sumpter, J. Huang, V. Meunier, J. M. Romo-Herrera, E. Cruz-Silva, H. Terrones, M. Terrones. *A theoretical and experimental study on manipulating the structure and properties of carbon nanotubes using substitutional dopants*. Int. J. of Quantum Chem. 109, 97-118, 2009

-
- ¹⁶ I.O. Maciel, J. Campos-Delgado, E. Cruz-Silva, M.A. Pimenta, B.G. Sumpter, V. Meunier, F. López-Urías, E. Muñoz-Sandoval, H. Terrones, M. Terrones, A. Jorio. *Synthesis, electronic structure, and Raman scattering of phosphorus-doped single-wall carbon nanotubes*. Nanoletters 9,6, 2267-2272, 2009
- ¹⁷ T. Kimura, T. Sugai, H. Shinohara. *Production and characterization of boron-silicon-doped carbon clusters*. Chem. Phys. Lett. 256, 269-273, 1996
- ¹⁸ C. Ray, M. Pellarin, L.L. Lermé, J.L. Vialle, M. Broyer. *Synthesis and structure of silicon-doped heterofullerenes*. Phys. Rev. Lett. 80, 24, 5365, 1998
- ¹⁹ R.J. Baierle, S. B. Fagan, R. Mota, A. J. R. da Silva, A. Fazzio. *Electronic and structural properties of silicon-doped carbon nanotubes*. Phys. Rev. B 64, 085413, 2001
- ²⁰ G. Tibbetts, C.A. Bernardo, D. W. Gorkiewicz, R.L. Alig. *Role of sulfur in the production of carbon fibers in the vapor phase*. Carbon 32, 4, 569-576, 1994
- ²¹ L. Ci, Z. Rao, Z. Zhou, D. Tang, X. Yan, Y. Liang, D. Liu, H. Yuan, W. Zhou, G. Wang, W. Liu, S. Xie. *Double wall carbon nanotubes promoted by sulfur in a floating iron catalyst CVD system*. Chem. Phys. Lett. 359, 63-67, 2002
- ²² Y.-L. Li, I.A. Kinloch, A.H. Windle. *Direct spinning of carbon nanotube fibers from chemical vapor deposition synthesis*. Science 304, 276-278, 2004.
- ²³ M. Motta, Y.-L. Li, I. Kinloch, A. Windle. *Mechanical properties of continuously spun fibers of carbon nanotubes*. Nanoletters 5, 8, 1529-1533, 2005
- ²⁴ I.O. Maciel, N. Anderson, M.A. Pimenta, A. Hartschuh, H. Qian, M. Terrones, H. Terrones, J. Campos-Delgado, A. Rao, L. Novotny, A. Jorio. *Electron and phonon renormalization near charged defects in carbon nanotubes*. Nature Materials 7, 878-883, 2008
- ²⁵ A.L. Elías, P. Ayala, A. Zamudio, M. Grobosch, E. Cruz-Silva, J.M. Romo-Herrera, J. Campos-Delgado, H. Terrones, T. Pichler, M. Terrones. *Spectroscopic characterization of N-doped single-walled carbon nanotube*

-
- strands: an X-ray photoelectron spectroscopy and Raman study.* Journal of Nanoscience and Nanotechnology (in press)
- ²⁶ C.S. Venkateswaran. *The Raman spectrum of sulphur in the solid and liquid states.* Proceedings Mathematical Sciences 1, 3, 120-121, 1934.
- ²⁷ R. Norris. *The Raman spectrum and the specific heat of crystalline sulphur.* Proceedings Mathematical Sciences 13, 4, 291-299, 1941
- ²⁸ Extracted from <http://www.photon.t.u-tokyo.ac.jp/~maruyama/kataura/kataura.html>
- ²⁹ B.G. Sumpter, V. Meunier, J.M. Romo-Herrera, E. Cruz-Silva, D.A. Cullen, H. Terrones, D.J. Smith, M. Terrones. *Nitrogen-mediated carbon nanotube growth: diameter reduction, metallicity, bundle dispersability, and bamboo-like structure formation.* ACS Nano 1, 4, 369-375, 2007
- ³⁰ I. O. Maciel, M.A. Pimenta, M. Terrones, H. Terrones, J. Campos-Delgado, A. Jorio. *The two peaks G' band in carbon nanotubes.* Phys. Stat. Sol. (b) 245, 10, 2197-2200, 2008

3. Production of carbon nanoribbons using the aerosol pyrolysis technique

Graphene is a single sheet of carbon atoms organized in a honey-comb structure. Before 2005, graphene was just a concept used by theorists to describe the formation of carbon nanotubes or to predict amazing electronic properties¹; nevertheless in that year a graphene boom took place when Novoselov *et al.*² reported their “scotch-tape” method to obtain single layer and double layer graphene.

This method gave scientists all around the world the opportunity to work with graphene as long as they had at their disposal HOPG, scotch-tape, SiO₂ substrates and an optical microscope. There are other ways to obtain graphene flakes and graphene nanoribbons, from heat treatment of diamond nanoparticles deposited on HOPG³, epitaxially grown⁴, with chemical treatments of graphite⁵, and more recently from treatments of carbon nanotubes^{6,7,8,9}.

Despite the production methods listed above, the synthesis of this material is still a challenge. Other drawbacks are the low yield production of the material, no control on its shape, the high pressure and temperature required for its synthesis, specific equipment, and high purity materials involved in the processes.

We have found a route to synthesize large amounts of graphitic nanoribbons, this material consists of stacked graphene sheets forming a ribbon-like structure of 10-20 nanometers in thickness, 20-300 nm in width and several microns in length¹⁰.

In this chapter we describe in detail the production method and we include results of the characterization carried out, which includes SEM, TEM, XRD, EDX and XPS.

The thermal stability of the graphitic nanoribbons has been tested through furnace heating. The resulting materials have been characterized by electron microscopy.

In particular a detailed Raman spectroscopy study of the heat treated nanoribbons is included.

3.1 Description of the synthesis method

The experimental set-up used in the synthesis of graphitic nanoribbons is shown schematically in Figure 3.1, where all the necessary equipment is placed inside a fume hood. A quartz tube (~1.1 m long), connecting an ultrasonic sprayer and a gas condenser/acetone trap for the exiting gases, is placed inside two tubular furnaces (see Fig. 3.1). The length of each furnace is 40 cm and the separation between the two furnaces is ~15 cm. An inert atmosphere is maintained by flowing argon gas through the system. A solution containing 280 ml of ethanol, 2.8235 mg of ferrocene (FeCp_2) and 0.266 ml of thiophene ($\text{C}_4\text{H}_4\text{S}$) is prepared and placed inside the ultrasonic sprayer. During the heating of the furnaces, the ultrasonic sprayer is kept turned off and the flow of Ar is set to 0.2 l/min. When both furnaces reach 950 °C, the ultrasonic sprayer is turned on. The aerosol thus produced is carried to the hot zone of the furnaces by raising the flow rate to 0.8 l/min. These conditions are maintained for 30 min, after which the sprayer is turned off, the flow rate is decreased to 0.2 l/min, and the two furnaces are allowed to cool down to room temperature.

Once the system has cooled down, the quartz tube is taken out and the material of interest containing the nanoribbons is scraped from the walls of the tube. The nanoribbons are deposited as a powder within furnace 1 in a region between 12 and 20 cm relative to the left edge position of the first furnace (see Figure 3.1).

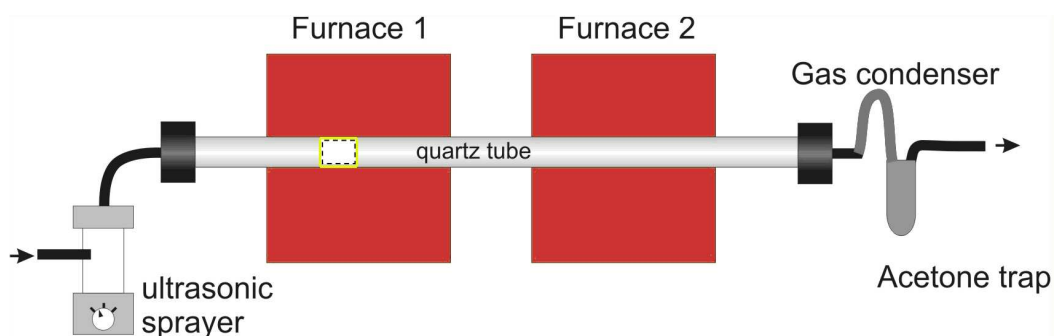


Figure 3.1 A schematic diagram of the experimental set-up used in the synthesis of graphitic nanoribbons. The yellow marked area in the tube within Furnace 1 corresponds to the region where the graphitic nanoribbon material is deposited during synthesis.¹¹

The powder containing the nanoribbons has been shown to be efficiently dispersible in various alcohols. We have used ethanol and methanol followed by sonication to create solutions of the graphitic nanoribbons. These solutions have further been used to prepare samples mounted on copper grid sample holders for use in scanning electron microscope (SEM) and transmission electron microscope (TEM) observations, and to prepare isolated nanoribbons samples.

3.2 Characterization of the pristine material

The morphology of the initial black powder consisted of ribbon-like structures exhibiting lengths of several microns, widths ranging from 20-300 nm and thicknesses of 10-20 nm (Figure 3.2). It is interesting to note that the initial ribbons revealed both flat regions as well as rippled areas (Figure 3.2b).

The edges of the as-prepared ribbons also displayed relatively sharp cuts that could be related to the presence of either zigzag or armchair edges (Figure 3.2b-c). Since the ribbons were extremely thin, SEM images (FEI-field emission SEM XL30 SFEG) almost suggested transparency when observed at 10-15 keV; note the presence of the holey carbon grid underneath the ribbons in Figure 3.2c.

Bright-field and dark-field images of the ribbons using scanning transmission electron microscopy (STEM), and are depicted in Figures 3.2d & 3.2f, respectively. The ribbons displayed only one type of contrast and Fe catalyst particles were never observed in these structures (note that carbon nanotubes containing metal catalyst particles at the nanotube tips were usually produced in the second furnace while the graphitic nanoribbon material was extracted from the first furnace).

By performing detailed elemental energy dispersive X-ray (EDX, using a JEOL JEM-2010F operated at 200 keV and equipped with a thin-window light-element-sensitive X-ray detector) spectroscopy line-scans along the ribbon surface (Fig. 3.2e), it was found that the nanoribbons consisted of C, while S was notably absent. Even surface-sensitive XPS could not detect any trace of S. Although graphene nanoribbons consist of only carbon, S appears to be crucial for growing the ribbons and it could well act as a catalyst. However, the presence of sulphur inserted in the

system during growth was positively confirmed in by-products found in a different zone of the quartz tube (i.e. in the region between furnace 1 and 2. See Chapter II for the description of similar experiments aimed to produce S-doped SWNTs, Figures 2.4 and 2.5). Figure 3.3 depicts ribbons under TEM and HRTEM imaging conditions (JEOL JEM-2010F operated at 200 keV). At low magnification, the material consisted only of carbon ribbons (Fig. 3.3a). HRTEM images of the ribbons (Figs. 3.3b-c) revealed the presence of hexagonal patterns, which were confirmed after obtaining the fast Fourier transform (FFT; see Fig. 3.3c inset). In order to confirm the graphitic structure and layer stacking, and to identify the edge structure, electron diffraction patterns were recorded from different ribbons (Fig. 3.3d). Interestingly, all the analyzed ribbons consisted of ABAB... stacked graphite (since all reflections from 3D graphite are visible in Fig. 3.3d), and the edges exhibited armchair and zigzag (or close to zigzag) morphologies (see below).

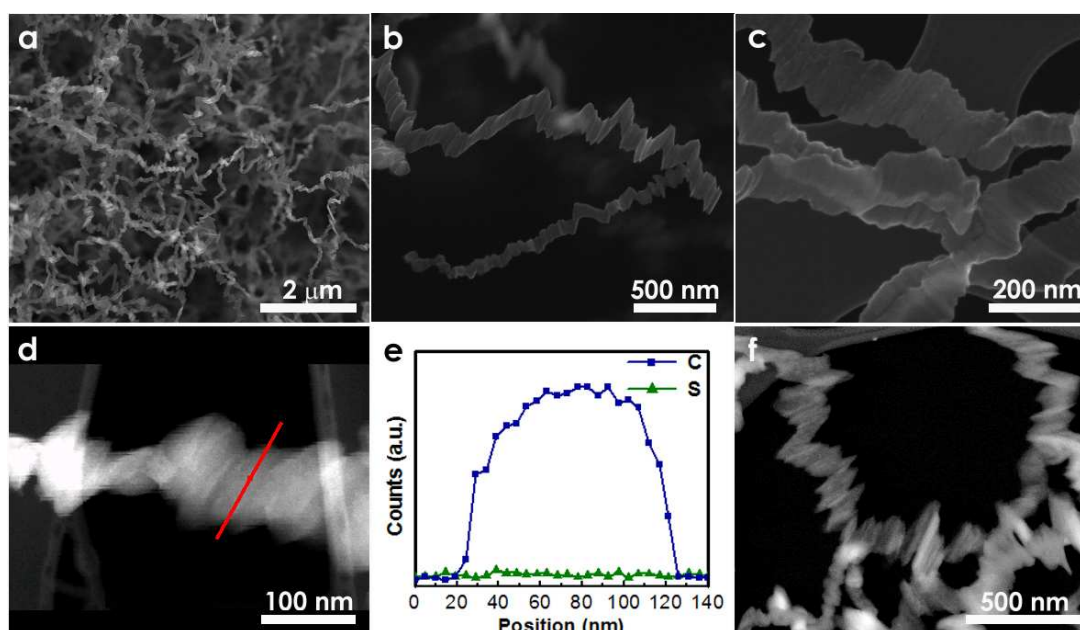


Figure 3.2 (a-c) SEM images of graphitic nanoribbons at different magnification. Note that the ribbons are very thin (~ 10 nm) and could be transparent to the SEM beam (see 1c); (d) HAADF image of a nanoribbon and its corresponding elemental EDX line-scan (see d), indicated by the line shown in (d). The elemental profile in (e) shows the absence of S and indicates that the ribbon mainly consists of C; (f) dark field STEM image of bulk nanoribbons displaying rippled regions within the ribbons.

The average bulk structure of the ribbon material was further studied by XRD (Bruker D8-advanced equipped with a Cu anode ($\lambda=1.5406 \text{ \AA}$) operated at 35 kV, 25 mA and 293 K). It was found that the nanoribbons exhibited a highly crystalline graphite-like structure, with the presence of strong (002), (100), (101), (004) and (110) reflections (Fig. 3.4a). Moreover, the linewidth of the (002) diffraction line gave an average L_c crystallite size of ca. 10-14 nm, in good agreement with SEM observations.

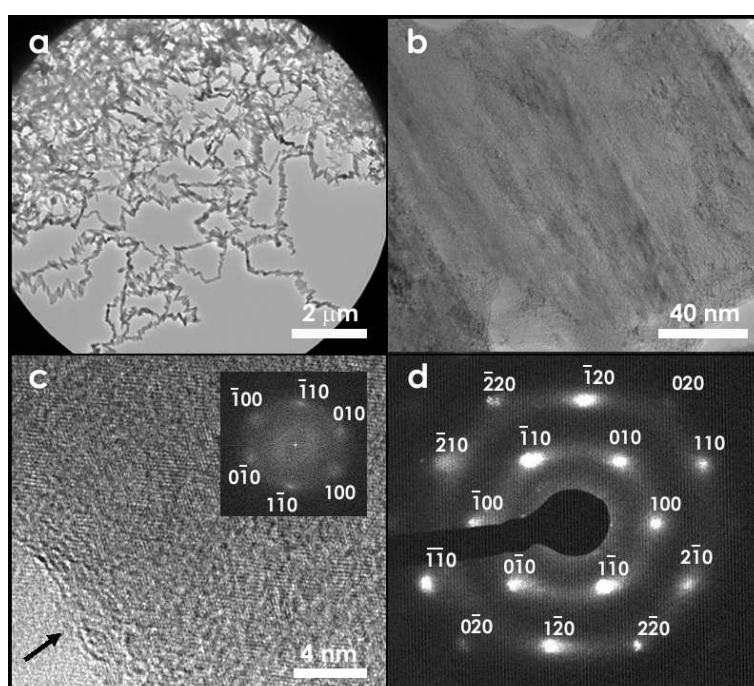


Figure 3.3 (a-b) Low and high magnification TEM images of graphitic nanoribbons; c) HRTEM image of a ribbon edge (the arrow indicates the ribbon edge) displaying a hexagonal pattern, and its corresponding FFT (inset); d) indexed electron diffraction pattern of an individual thin graphene nanoribbon (ca. 10 nm thick) showing the ABAB... stacking of the graphite structure with a 3D order

Bulk Raman spectroscopy measurements on the ribbons (Renishaw InVia system equipped with laser excitation energy $E_{\text{laser}} = 2.41 \text{ eV}$) revealed the presence of the D and G bands, located at 1355 and 1584 cm^{-1} , respectively (Fig. 3.4b). In general, it was found that the D-band exhibited the highest intensity, probably due to the high proportion of edges and ripples within the ribbons. The disorder-induced combination mode (D+G) at about 2940 cm^{-1} is also exceptionally strong. A more

detailed Raman spectroscopy study of pristine and heat treated nanoribbons is included in future pages.

In order to confirm that the nanoribbons were highly crystalline, we performed TGA studies (Thermo Haake, Cahn VersaTherm HS heating at 5 K/min to 1173 K in air). It was found that the decomposition temperature of the ribbons in air corresponded to 702 °C (Fig. 3.4c). This value is almost the same as that observed in highly crystalline carbon nanotubes produced by arc discharge techniques²⁴. Adsorption isotherms of N₂ and H₂ were measured volumetrically at 77 K after preheating in vacuo. Nitrogen (N₂) adsorption measurements on the carbon nanoribbons (Fig. 3.4d) revealed a BET surface area of 59 m²/g, which was similar to the surface area of acetylene black (86 m²/g). The adsorption data indicated that the nanoribbon material corresponds to a flat surface, which was not porous to N₂ molecules. The interaction of an N₂ molecule with the surface of the nanoribbon is weaker than that with highly-crystalline carbon black, which is in agreement with the presence of predominant edge-like surfaces. However, H₂ adsorption at 77 K indicated the presence of rather strong sites for supercritical H₂ adsorption corresponding to ca. 15 % of the monolayer capacity of N₂. Consequently, the nanoribbon should have a unique nanostructural fit for the adsorption of supercritical H₂.

XPS studies revealed the nature of the carbon bonds present in the sample (Figs. 3.4e-f) (JEOL JPS-9010MX using Mg K α radiation at 10⁻⁶ Pa. XPS spectrum being deconvoluted with a Gaussian-Lorentzian mixed function after correction). The material contained sp² and sp³ hybridized carbon atoms (39% sp² and 39% sp³; Fig. 3.4e), and the rest of the carbonaceous material was bonded to O (Fig. 3.4f) and consisted of carbonyl groups (C=O) and carboxylic groups (COO); note that 85 at. % corresponded to C and 15 at. % to O. We believe that the large number of sp³ hybridized carbon atoms was caused by the exposed edges and the rippled (highly curved) regions within the nanoribbons. The 1:1 ratio of sp³:sp² carbon atoms could also explain the large intensity of the D-band observed in Raman spectroscopy, because the material was indeed highly crystalline and showed an AB... stacking of the graphene layers.

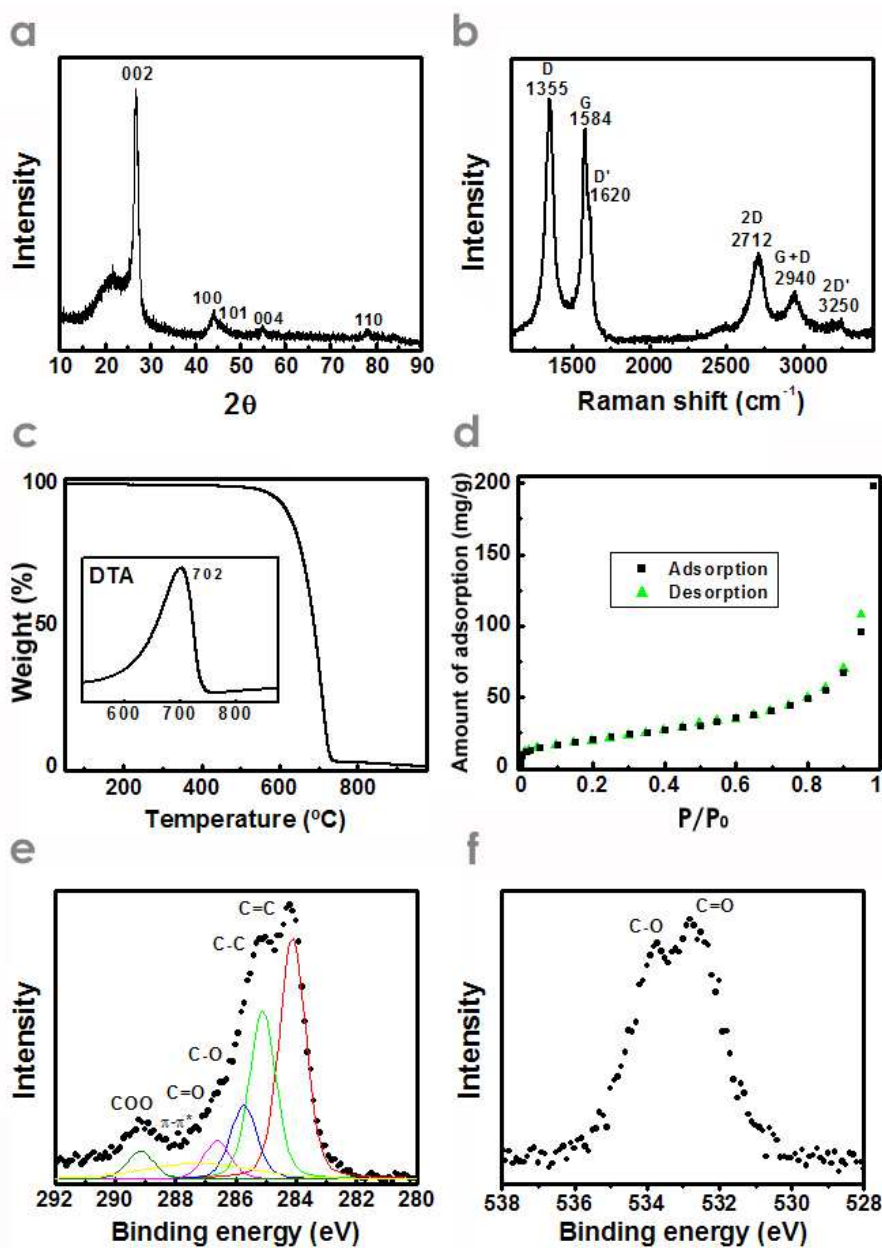


Figure 3.4 (a) XRD pattern of a bulk nanoribbon sample; (b) typical Raman spectrum of bulk nanoribbons showing the presence of the D and G band as well as the overtone and combination mode features taken at 514 nm laser excitation; (c) TGA plot and its first derivative presented in the inset showing the behavior of the DTA peak in an oxygen atmosphere for the ribbon material at high temperature; (d) A Typical N_2 adsorption isotherm of the nanoribbon sample; (e) XPS data of graphene nanoribbons for the C binding energies; it is clear that sp^2 and sp^3 hybridized carbon atoms are included in the sample with a 1:1 ratio, as well as carbonyl groups (C=O) and carboxylic groups (COO), and (f) XPS data for graphene nanoribbon material corresponding to the O binding energies, confirming the presence of different O terminated edges.

3.3 Annealing treatments of carbon nanoribbons

Historically, post-synthesis thermal treatments of carbon materials have been used with different objectives, including the achievement of higher degrees of graphitization¹², elimination of amorphous carbon in carbon nanotubes^{13,14}, graphitization of diamond particles³, transformation of SWNT bundles into graphite nanoribbons¹⁵, and the elimination of metal particles from the starting materials^{16,17}. During these thermally-induced structural transformations processes like graphitization and a process called loop formation at the edges of graphitic materials occurs¹⁸⁻²² (see Figure 3.5), whereby the chemically reactive open edges of adjacent graphene sheets join with one another to form a semi-cylindrical loop with a radius larger than the sheet-to-sheet separation distance.

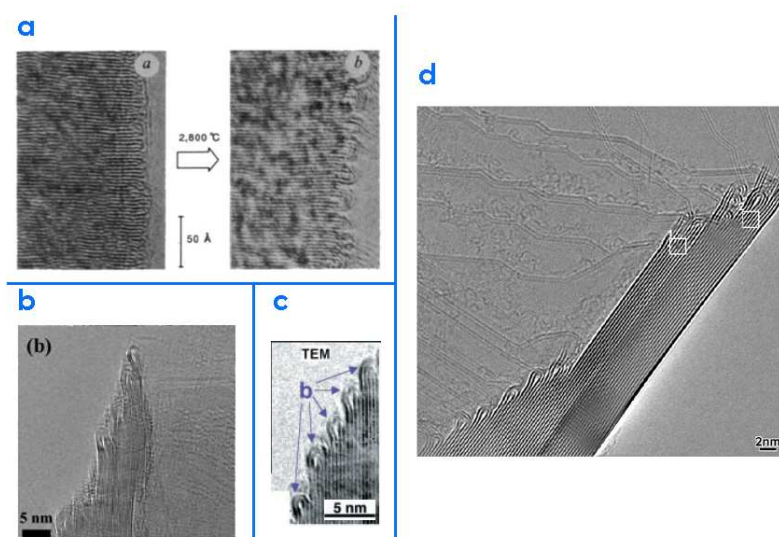


Figure 3.5 Loop formation at the edges of graphene planes induced by heat treatments in different carbon materials, a) filamentous graphite¹⁸, b) cup-stacked fibers²⁰, c) graphite polyhedral crystals¹⁹, and d) powders of pyrolytic graphite²¹.

These loops, which serve to eliminate the reactive edges and satisfy the dangling bond requirements of the edge structures, have been observed for diverse graphitic materials after heat treatments.

In Figure 3.5 we show some representative images of such materials: filamentous graphite¹⁸, graphite polyhedral crystals¹⁹, cup-stacked nanofibers²⁰ and powders of

lyolytic graphite²¹. José-Yacamán *et al.*²² previously reported an elongated graphitic structure with bent ends, and although closed ends were also observed in this prior report, their bent ends do not resemble the loops observed in the present work.

On the other hand, a sensitive technique to the graphitization process that occurs during annealing is Raman spectroscopy, through the evolution of the D, G and G' bands we can have an idea of the degree of graphitization of the studied sample. Figure 3.6 pictures heat treatment experiments found in the literature for different carbon materials studied by Raman scattering.

In order to study the thermal stability of our nanoribbons, high temperature heat treatments were conducted by collaborators in Japan, using a graphite furnace for 30 minutes under an Ar atmosphere. The heat treatment temperatures (T_{HT}) used in the study were 1000, 1500, 2000, 2500 and 2800 °C, the resulted samples will be denoted by "HT **** °C". SEM imaging, TEM imaging, X-ray powder diffraction, and thermogravimetric analysis (TGA), were used to characterize our ribbon samples upon increasing the heat treatment temperature²³. A Raman spectroscopy study at the bulk and individual level was also performed.

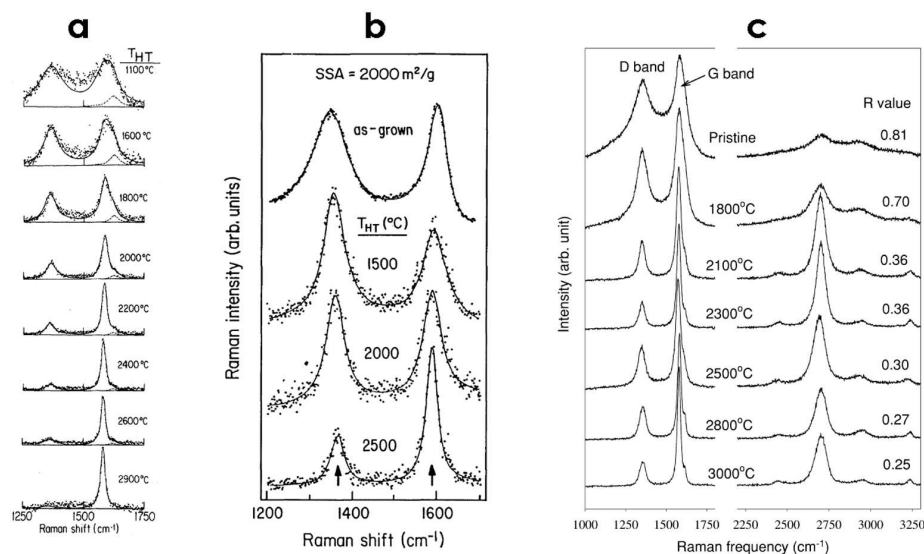


Figure 3.6 Raman spectroscopy of heat treated carbon materials, a) benzene-derived carbon fibers²⁴, b) activated carbon fibers²⁵, c) cup-stacked carbon fibers²⁰

3.3.1 Characterization of the annealed materials

The morphology of the heat treated (HT) ribbon samples was studied by SEM (FEI-field emission SEM XL30 SFEG).

The distinctive morphology features of the pristine sample, such as ripples on the surface and un-continuous edges, are still present in the HT samples.

In general these samples do not seem to show dramatic changes, as can be observed in Figure 3.7, which shows SEM micrographs for the pristine sample, HT 1000 °C, HT 2000 °C, 2500 °C and HT 2800 °C. Sample HT 1500 °C, not shown here, also shared the pristine morphology characteristics.

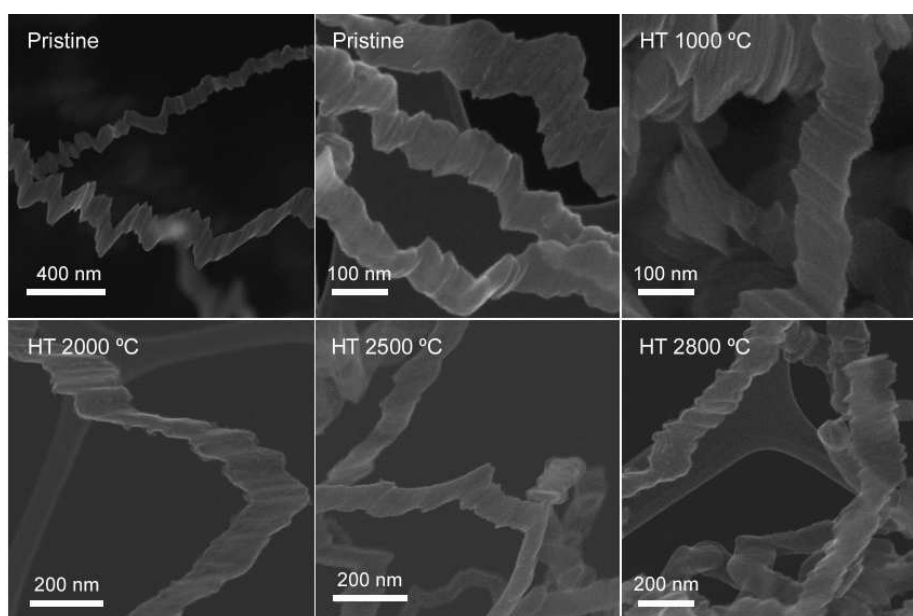


Figure 3.7 Different magnification SEM images of HT carbon nanoribbons

In order to study the structure of the HT samples we performed high-resolution TEM (JEOL JEM-2010F operated at 200 keV), with special interest on the edges of the nanoribbons, Figure 3.8 depicts the side-edge structure for the different T_{HT} values.

As the T_{HT} is increased it is evident that transformations take place, leading to structures with many striking differences that will be discussed carefully in the following paragraphs.

It is clear that the pristine sample contains many active end planes (edges).

As the samples are annealed, interesting features can be pointed out:

- 1) Small structural changes are observed for the pristine and the 1000 °C T_{HT} sample, both exhibit a well developed lattice fringe structure. We attribute these small changes to the fact that the synthesis temperature (950 °C) of the pristine material is very close to the first annealing temperature (1000 °C).
- 2) At 1500 °C, the lattice fringes straighten up and single-loops start to appear at the edges, although open edges are still present. Here, it is clear that point defects present in the individual layers start to anneal and disappear.
- 3) At 2000 °C, the disappearance of open edges and double-loop formation are observed.
- 4) For the highest annealing temperatures (2500 °C - 2800 °C), we observe increasingly straighter lattice fringes, multi-loop formation covering an increasing number of layers and the absence of open edges.

It is evident that a graphitization process, defect annealing and loop termination of edges due to high temperature exposure take place in the samples.

The loop formation observed in the edges of the ribbons has already been reported when temperature increasing is involved in the experiments¹⁸⁻²¹.

X-ray powder diffraction patterns (Philips Diffractometer model 12014424, Cu K α radiation $\lambda=1.54$ Å) plotted in Figure 3.9a, reveal a match to the graphite pattern for several reflections, not just for the (002) reflection, as is done in most studies of CVD-produced MWNTs²⁶.

The analysis of the (002) peak position revealed an average interlayer spacing of 3.36 Å (close to perfect graphite) for the pristine sample, HT 1000 °C, HT 2500 °C and HT 2800 °C samples, and 3.37 Å for the HT 1500 °C and HT 2000 °C samples.

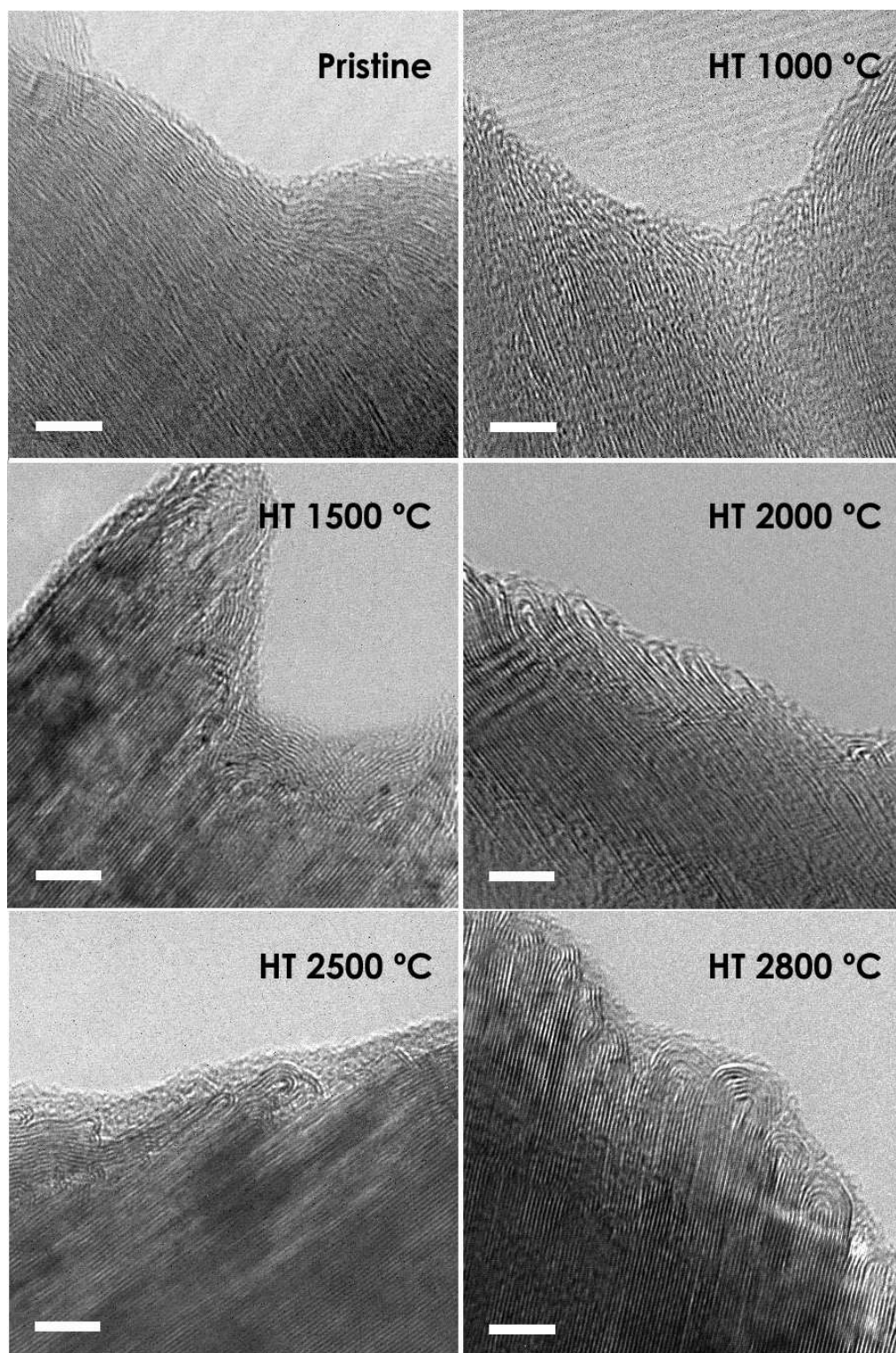


Figure 3.8 Transmission electron micrographs of the different HT carbon nanoribbons (scale bar = 5 nm).²³

Small changes are seen in all the reflections as the annealing temperature increases (see Fig. 3. 9b). It is noteworthy that in the HT samples no iron carbide peaks are present, as has been reported for the pristine ribbons¹⁰.

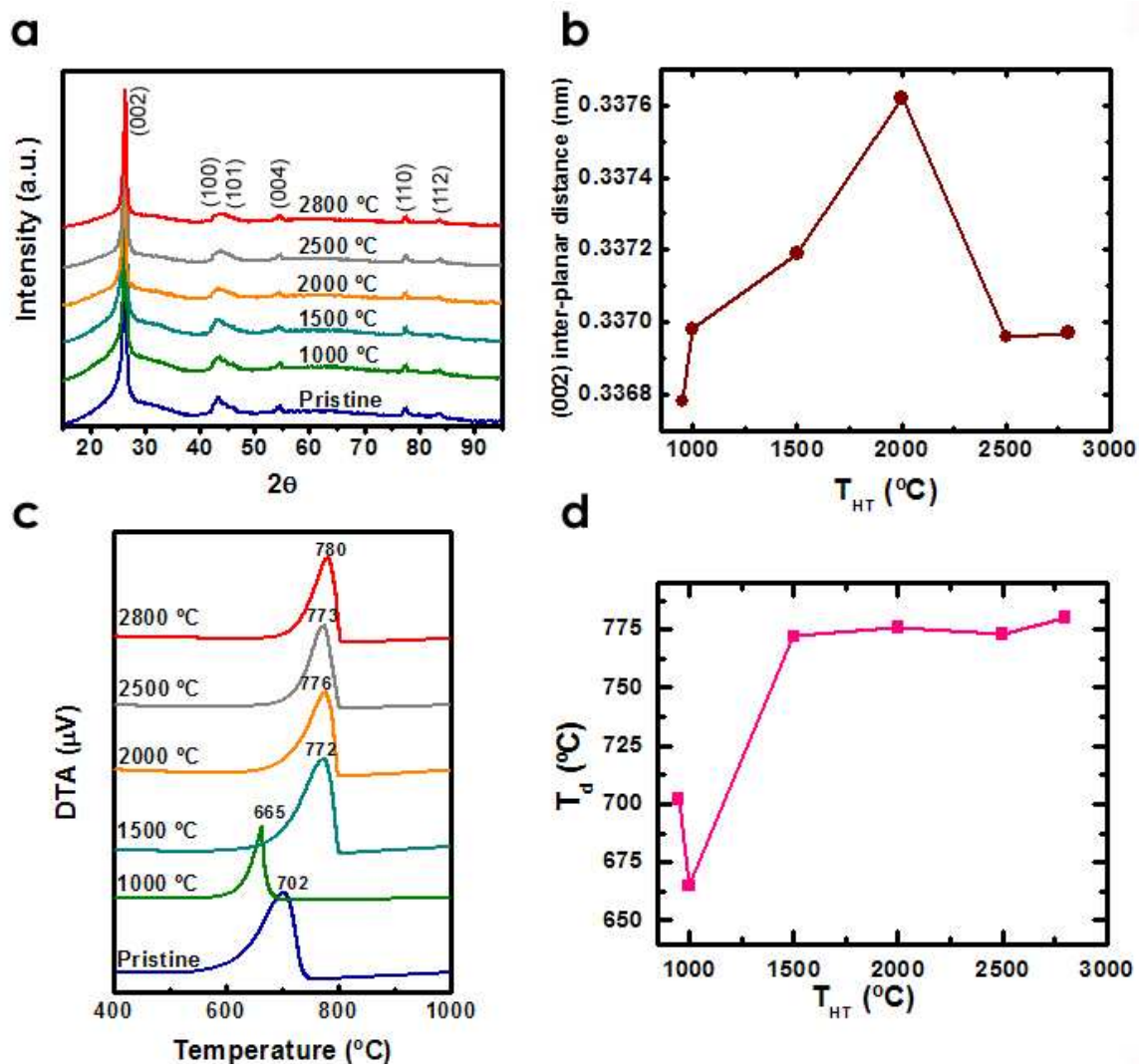


Figure 3.9 a) X-ray diffraction characterization of each HT treated sample, the numbers in parenthesis indicate the crystallographic reflections, b) interlayer distances between the (002) planes as a function of T_{HT} , c) first derivative with respect to temperature of the weight loss (DTA) curves of the heat treated samples, and d) T_d vs. T_{HT} plot for the peak temperature in c) for the different HT samples (the growth temperature for the pristine sample is 950°C).²³

In Fig. 3.9c, we show the first derivative with temperature (DTA) of the weight loss curves obtained from the TGA analysis (Thermo Haake, Cahn VersaTherm HS system, heating the samples at 5 °C/min to 900 °C in air).

Interesting phenomena can be deduced from these measurements:

- As T_{HT} is increased, the TGA analysis reveals an up-shift in the decomposition temperature T_d of the ribbon materials in air, from 702 °C for the pristine sample to 780 °C for the HT 2800 °C sample; this behavior suggests a restructuring taking place during the heating process (replacement of open edges by loops), which makes the material less reactive, thereby increasing the decomposition temperature.
- The HT 1000 °C sample, however, has a lower T_d (665 °C) than the pristine sample (702 °C). As suggested by previous work in carbon nanotubes²⁷, defect migration and vacancy coalescence induced by heat treatment effects could be taking place at this stage, forming large area defects which turn the sample into a more reactive material. It is also possible that at 1000 °C in an Ar atmosphere, the ribbon sample detaches some passivation atoms (e.g. H, O) that recombine with defective areas creating larger reactive and broken regions around defects. The above effects, combined with the presence of open edges passivated by oxygen or hydrogen groups, could contribute further to the decrease of the decomposition temperature. It is noteworthy that at 1000 °C the ribbon sample is not able to completely anneal defects into energetically stable sp^2 hybridized carbon regions, thus leaving a metastable carbon network that is still quite reactive.
- A difference of 107 °C in T_d for the HT 1500 °C and HT 1000 °C samples suggests that the number of defects and reactive sites decreases significantly in this temperature range. We suggest that competing processes are here in play. Firstly, the high temperature promotes the annealing of defects as

revealed by the straightening of the lattice fringes observed in Figure 6, and the termination of the reactive edges by loop formation are responsible for the T_d change.

- For the HT 1500 °C samples and up, the T_d range is from 772 °C to 780 °C (see Fig. 3.9d). This stability in T_d suggests that no major restructuring of the sample is occurring among these different temperature stages, which agrees with our TEM observation in that the edges form single to multiple loops in this temperature range, thereby reducing chemically active sites and reducing the overall reactivity.

In order to have a clear picture of the restructuring taking place during annealing treatment, we have identified the transformations that occur for each T_{HT} . Figure 3.10 shows a diagram imaging such transformations.

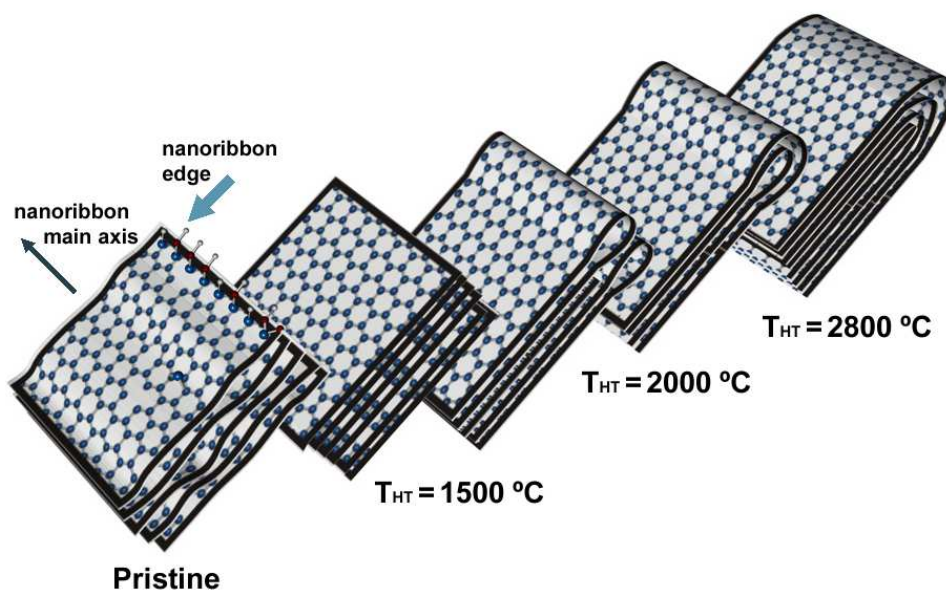


Figure 3.10 Schematic model for the restructuring process achieved by the thermal annealing treatment.²³

For T_{HT} below 1500 °C the sample consists of relatively well ordered planes and well-developed crystallinity (confirmed by XRD and electron diffraction¹⁰) but still

contains point defects (vacancies), out-of-plane interstitial atoms, Stone-Wales and other defects, in addition to the bare edges of the ribbons where some oxygen groups are present¹⁰.

By 1500 °C, defect annealing starts to take place and we observe straighter lattice fringes, approaching a defect-free planar structure, and some open edges become passivated by single-loop formation driven by surface energy minimization.

For HT 2000 °C, double loop formation is evident, and as the temperature is increased further, multi-loops with increasing loop diameters are observed and open edges are no longer present.

The zipping mechanism proposed by Rotkin²⁸ seems to elegantly describe the loop formation phenomenon. According to this model, two adjacent graphene sheets will tend to join their edges to form a loop, and the radius of curvature will systematically be greater than the separation of the sheets.

When single and double loops are formed (see Figure 3.8) an increase in the radius of curvature is evident, confirming this aspect of the proposed model²⁶.

This local increase in the interlayer distances at the loops may well explain the presence of slightly higher interlayer spacings observed by analyzing the graphite (002) peak from the X-ray powder diffraction patterns of samples treated at different temperatures.

Note that as the loop radius is increased, the loops start forming more faceted structures, as is commonly seen in other carbon nanostructures^{10,29}.

3.3.2 Raman spectroscopy study of the annealed materials

Raman spectroscopy is a powerful tool to analyze carbon nano-systems, due to the sensitive response in Raman signal of C-C bonds and defects in the structure (see Appendix B).

Bulk micro Raman spectra with laser excitation energies in the range 1.91 eV - 2.61 eV were acquired at room temperature for 2 minutes with laser powers of 1

mW. The samples were analyzed in the backscattering geometry using a 100x objective lens which focused the laser beam on a spot of $\sim 0.5 \mu\text{m}$ in diameter. At least two measurements were recorded per sample and the spectra shown here are the resulting averages. All the spectra were normalized to the G band intensity. Seven different laser energies were used: Krypton (1.91 eV), Argon (2.41, 2.54, and 2.61 eV), YAG (2.33 eV) and Rhodamine dye (2.13 and 2.17 eV). Spectra were recorded for six samples (a pristine sample and samples heat treated at 1000 °C, 1500 °C, 2000 °C, 2500 °C and 2800 °C).

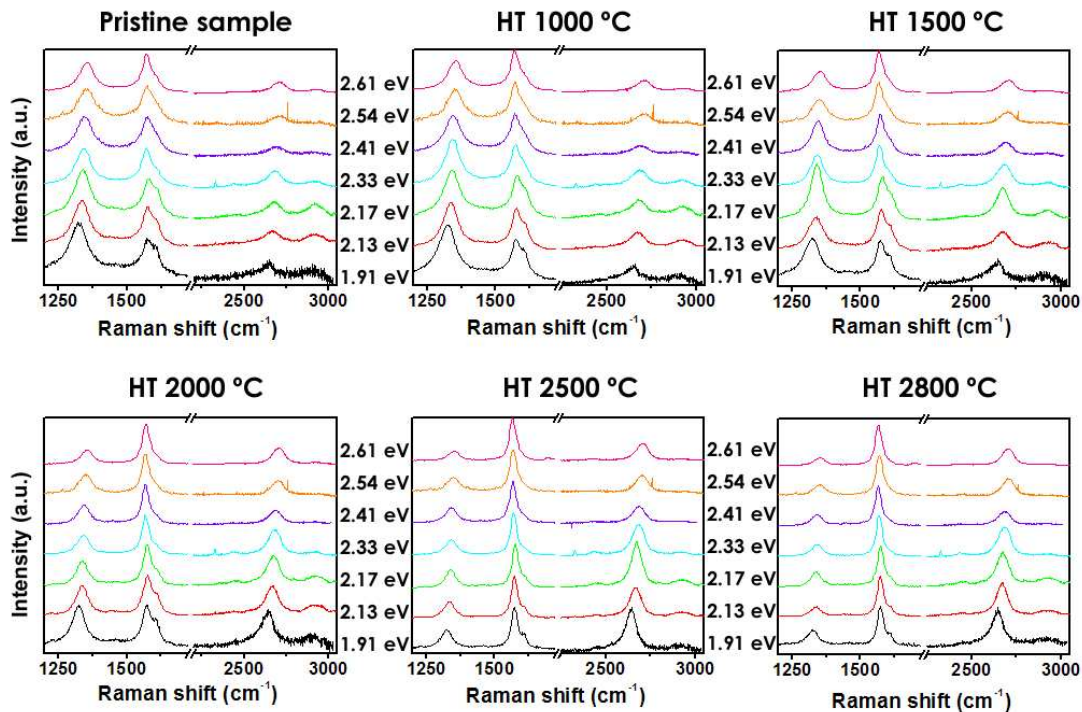


Figure 3.11 Bulk Raman spectra of the investigated samples using seven different laser excitation energies in the range 1.91 eV - 2.61 eV.

In Figure 3.11 we show the spectra of the bulk pristine sample, and the bulk heat treated samples at 1000, 1500, 2000 °C, 2500 and 2800 °C (HT 1000 °C, HT 1500 °C, HT 2000 °C, HT 2500 °C and HT 2800 °C, respectively).

A quick inspection of these measurements reveals differences among the three samples for each of the different E_{laser} . The main Raman features (D, G, D' and G')

bands) show interesting behavior as the heat treatment temperature (T_{HT}) and E_{laser} are increased.

In order to make a quantitative analysis of the Raman features, we have fitted those main peaks for the pristine, HT 1500 °C, HT 2000 °C and HT 2800 samples for each of the seven laser excitation energies. We used a program to automatically identify and fit the peaks with Lorentzians called “Peak Fit”, with the Residuals method.

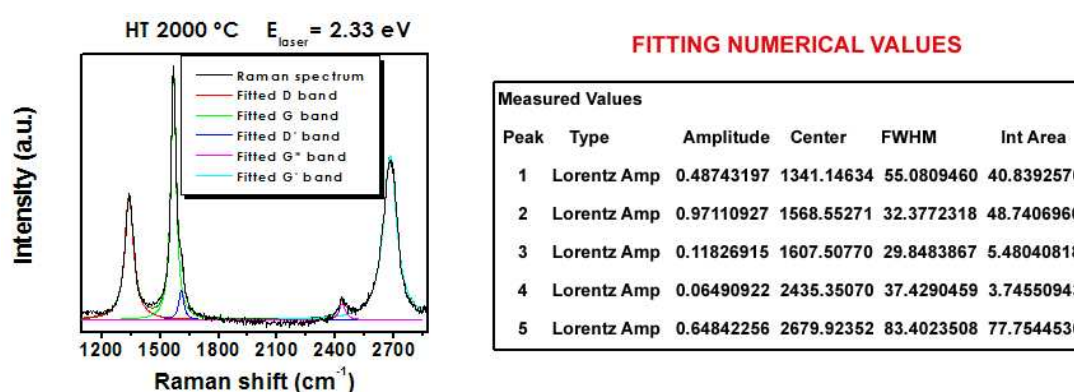


Figure 3.12 Example of the fitting carried out for the bulk Raman measurements. The spectrum of the sample HT 2000 °C for $E_{laser} = 2.33$ eV was fitted with 5 Lorentzian peaks (plot on the left), the numerical values derived from the fitting (right) were further used for analysis of the frequency positions and the integrated area ratios.

Each spectrum was fitted with 4 main peaks (D, G, D' and G' bands) sometimes 5 peaks (D, G, D', G* and G').

The numerical information derived from the fitting was used to identify frequency positions at maximum intensity of the peaks and to calculate ratios of the integrated areas as will be discussed below (See Figure 3.12).

When a study at different E_{lasers} is carried out, the dispersion (change) of the peak positions can be quantified as a function of laser energy. Of particular interest is the shifting of the D- and G'-band peaks with different E_{laser} . Both peaks shift to higher frequency values as E_{laser} is increased, in accordance with double resonance theory³⁰.

Figure 3.13a summarizes the frequency behavior of the D-, G-, D'- and G'- bands for the pristine sample (open squares), HT 1500 °C (open circles), HT 2000 °C (open inverse-triangles) and HT 2800 °C (open triangles) samples as a function of E_{laser} . The peak position of the D- and G'-bands show a very strong dependence on E_{laser} , up-shifting linearly as E_{laser} is increased.

These peaks show the same behavior as that reported for other sp^2 carbon materials.^[31,32,33] On the other hand, the frequencies of the G and D' bands hardly change as E_{laser} is increased.

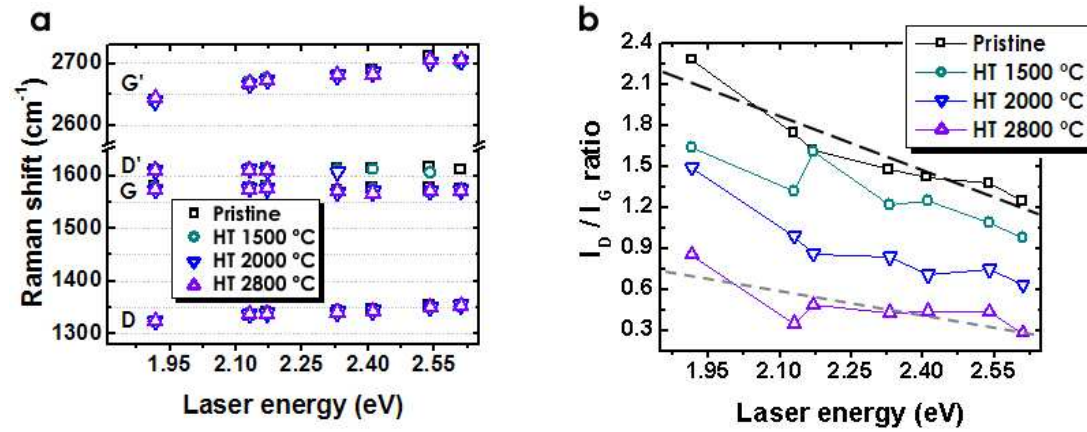


Figure 3.13 a) D-, G-, D'-, and G'- band positions as a function of E_{laser} for the pristine, HT 1500 °C, HT 2000°C and HT 2800°C samples, b) I_D/I_G ratios vs. E_{laser} , the black (violet) dashed line represents a linear fit to the pristine (HT 2800 °C) values

We can point out that the slopes of the dependence for the frequency of the D- and G'- bands on E_{laser} take the highest values for the pristine sample and the lowest for the HT 2800 °C sample.

The pristine sample shows a frequency dependent slope for the D-band on E_{laser} of $\partial\omega_D/\partial E_{\text{laser}} \approx 43 \text{ cm}^{-1}\text{eV}^{-1}$ and the slope of the G'-band is $\partial\omega_{G'}/\partial E_{\text{laser}} \approx 96 \text{ cm}^{-1}\text{eV}^{-1}$. For the HT 2800 °C sample, the values are: $\partial\omega_D/\partial E_{\text{laser}} \approx 36 \text{ cm}^{-1}\text{eV}^{-1}$ and $\partial\omega_{G'}/\partial E_{\text{laser}} \approx 87 \text{ cm}^{-1}\text{eV}^{-1}$.

These numbers indicate a difference in dispersion directly related to the changes induced by the heat treatments in the sample such as defect annealing, in-plane crystallization, and loop formation at the edges.

There is a remarkable difference from the values reported by Vidano *et al.*³⁰ and Matthews *et al.*³¹ ($\partial\omega_D/\partial E_{\text{laser}} \approx 50 \text{ cm}^{-1}/\text{eV}$ and $\partial\omega_G/\partial E_{\text{laser}} \approx 100 \text{ cm}^{-1}/\text{eV}$) where sp^2 -hybridized carbon materials were used, such as disordered pyrolytic and glassy carbons, crystalline graphite, PPP and HOPG.

The differences in these values might be attributed to the nature of our sample, which could contain a starting 1:1 ratio of sp^2 - sp^3 hybridization (e.g. pristine sample), and a high density of edges¹⁰.

In 1984 Lespade and co-workers³⁴ performed a Raman study of graphitization of different carbon samples under heat treatments. They came up with four “graphitization indices” derived from the Raman spectra.

In this discussion we will use two of them, the I_D/I_G ratios and FWHM of the G band, in order to monitor the graphitization process of the heat treated nanoribbons.

In Figure 11 we can observe an increase in the D-, D'- and G'-band intensities as E_{laser} is decreased. In the case of the D-band, this tendency is quantified through the ratio of the integrated intensities of the D- and G-bands (I_D/I_G) shown in Figure 3.13b as a function of E_{laser} .

For all of the samples, we observed lower I_D/I_G ratios when high E_{laser} energies are used. For the lowest energy ($E_{\text{laser}}=1.91 \text{ eV}$), the I_D/I_G ratios were the largest for all four samples (unannealed and heat treated).

Looking at the set of I_D/I_G ratio values for each sample, the dependence on E_{laser} for the pristine sample is the highest (making a rough linear fit to the values, the slope of the line is -1.3 a.u./eV , as seen from the black dashed line in Figure 3.13b), while the dependence on E_{laser} decreases significantly for the sample heat treated at $2800 \text{ }^\circ\text{C}$ (fitting the values linearly, the slope of the line is -0.55 a.u./eV , see violet dashed line in Figure 3.13b).

Once again, the differences on E_{laser} dependence of the I_D/I_G ratios may be attributed to intrinsic changes triggered by the annealing treatments.

The shifts to smaller values in the I_D/I_G ratios are noteworthy as we increase the heat treatment temperatures from 1500 °C to 2800 °C, suggesting an increase in crystalline order induced by the heat treatment temperature (T_{HT}). This latter sample, as described previously²³, consists of a highly crystalline graphite-like material exhibiting multiple *loops* formed between adjacent graphene layers as a result of the high temperature annealing treatment (see Figure 3.8).

The evolution of the FWHM (Full Width at Half Maximum) of the G band as a function of heat treatment temperature for each laser line is plotted in Figure 3.14a. The decrease in FWHM as T_{HT} is increased, confirms a sharpening of the G band which is a direct evidence of enhanced crystallization and the annealing of structural defects.

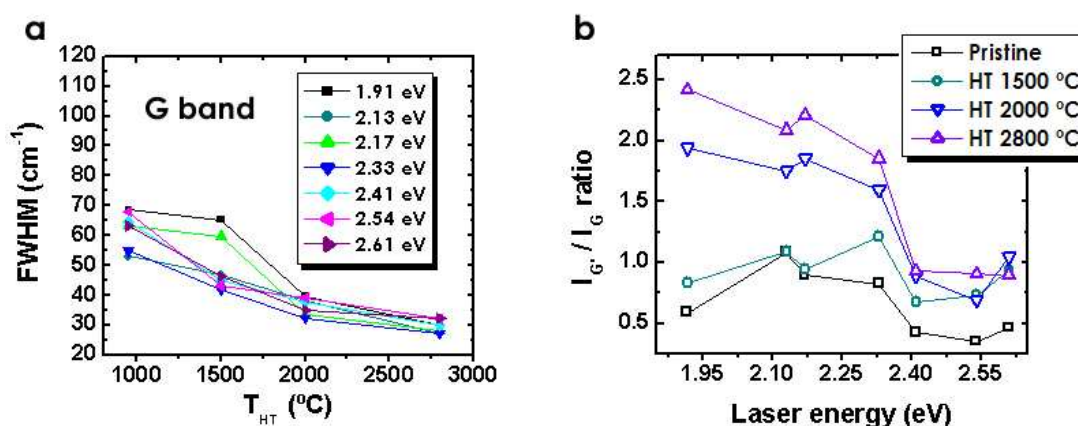


Figure 3.14 a) FWHM values of the G band as a function of heat treatment temperature (T_{HT}) for each of the seven excitation laser energies, and d) $I_{G'}/I_G$ ratios vs. E_{laser} .

When looking at Figure 3.11, especially at low energies (1.91 eV - 2.17 eV), it is evident that the intensity of the G' band shows a progressive increase as the heat treatment temperature is increased. Figure 3.14b shows a plot of the $I_{G'}/I_G$ ratios as a function of laser energy. Contrary to the behavior of the D band, the $I_{G'}/I_G$ ratios show their lowest values for the pristine sample and the highest ones for the HT 2800 °C sample. The $I_{G'}/I_G$ ratios reveal a dependence on E_{laser} , though it is not linear and it does not follow the behavior shown by the I_D/I_G ratios.

One remarkable feature of the ribbon samples is their inability to graphitize completely. The double peak shape of the G' band (characteristic of HOPG and graphitized materials, explained by a second order double resonance Raman process where we observe signal from the incident and scattered phonons²⁸) is not observed in our samples, not even for the material annealed at the highest temperature (2800 °C). This is probably due to the loop termination of the edges which is itself symmetry-breaking and should contribute in intensity to disorder-induced Raman features.

In summary, the bulk Raman measurements confirm that after thermal annealing, the material enhanced its degree of crystallinity. The low residual D-band in the HT 2800 °C sample indicates a more crystalline structure when compared to its unannealed counterpart, but showing still remaining symmetry-breaking elements caused by the formation of loops.

In order to prepare isolated nanoribbon samples, a powder of the pristine sample and samples heat treated at 1500 °C and 2800 °C were dispersed in methanol and sonicated for 1 hour. After this time, one drop of the solution was deposited on a Si/SiO₂ substrate.

Due to the length dimensions of the nanoribbons (several microns), the identification of the individual nanostructures was possible using an optical microscope.

Once the isolated nanoribbons were detected, we performed scans of the individual ribbons with $E_{\text{laser}} = 2.33$ eV at steps of 0.2 μm .

A computerized/motorized stage allowed us to precisely move the substrate in order to scan the region of the substrate containing the nanoribbon of interest.

Each final measurement lasted 60 seconds and the optical power at the sample position was maintained below 0.3 mW in order to avoid local heating effect.

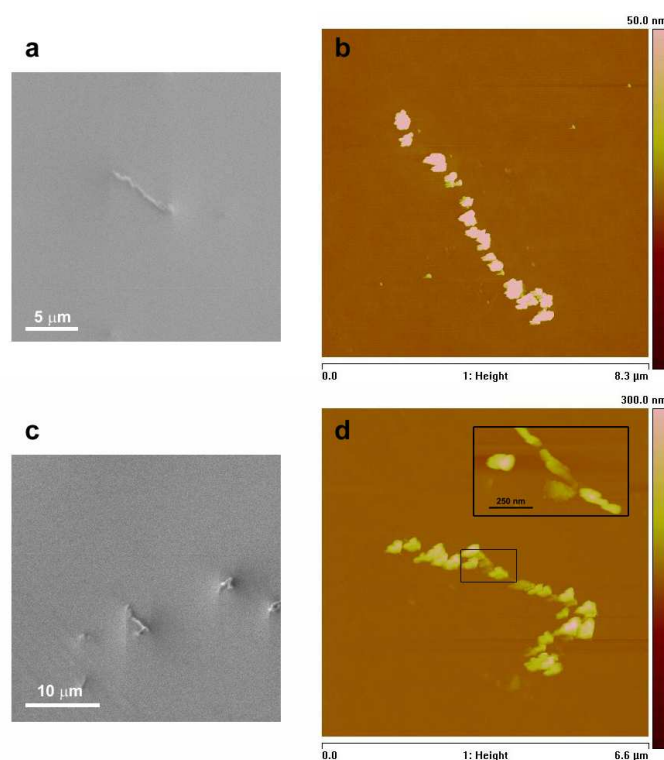


Figure 3.15 a) and c) SEM micrographs of a pristine nanoribbon and a nanoribbon annealed at 2800 °C, respectively. The same pieces imaged by AFM after laser irradiation at 1.5 mV, b) pristine and d) HT 2800 °C. The inset in d) contains a higher resolution AFM image of the marked section.

Our first measurements, at relatively low power levels (~ 1.5 mW) with $E_{\text{laser}} = 2.33$ eV and post-AFM-imaging (Atomic Force Microscopy) of the species, revealed damage of the structure.

Figure 3.15 a and c shows two individual nanoribbons identified by SEM before Raman spectroscopy, a pristine sample in a) and a heat treated one at 2800 °C in c).

After the material was scanned with the laser, at powers around 1.5 mW, the structure was modified as can be observed in Figure 3.15 b) and d), at this point what looked continuous in a) and c) became irregular with a segmented morphology. We assume that some parts of the ribbons were not in complete contact with the substrate, and therefore the heat induced by the incident laser could not be efficiently dissipated and this led to the destruction of the material.

This information suggests that the sample had an overall low thermal conductivity. To prevent sample heating and temperature dependent shifts of the Raman spectra, the power was decreased to ~ 0.3 mW when probing the nanoribbons.

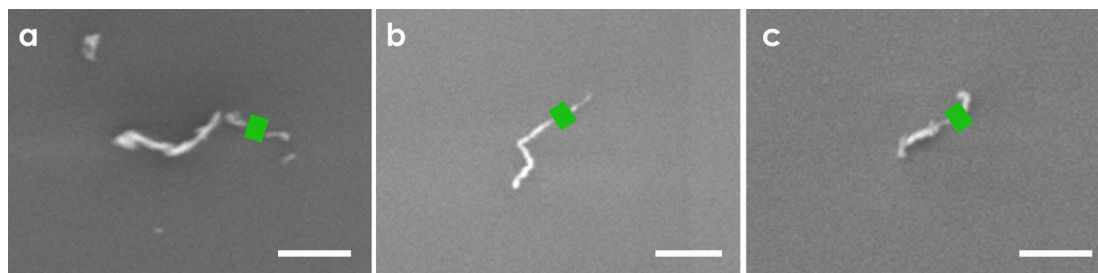


Figure 3.16 SEM micrographs of the individual nanoribbons, a) unannealed sample, b) sample annealed at 1500 °C and c) sample annealed at 2800 °C. The green lines across the nanoribbons indicate the areas where the measurements were recorded and the real magnitude of the laser beam spot. Scale bars = 2 μm .

Once individual nanoribbons were identified using an optical microscope, scanning electron microscopy was used to characterize them. Figure 3.16 shows the isolated nanoribbons used in the measurements reported in Figure 3.17. The wide green lines in Figure 16 represent the real area scanned by the incident laser beam.

Raman spectroscopy line scans were performed across the nanoribbons, each scan consisting of 4-6 individual measurements at steps of 0.2 μm , going from one edge of the nanoribbon to the other (Figure 3.16 and 3.17d). Considering the spot size of the laser beam, this procedure allowed us to hit the sample mainly on the edges when the laser was far from the center of the nanoribbon.

The results of these measurements are plotted in Figures 3.17 a, b and c, and a diagram of the positions of the measurements relative to the nanoribbon morphology is shown in Figure 3.17d. It is clear that the spectra recorded far from the center of the nanoribbons show more intense D band features for all three nanoribbon samples.

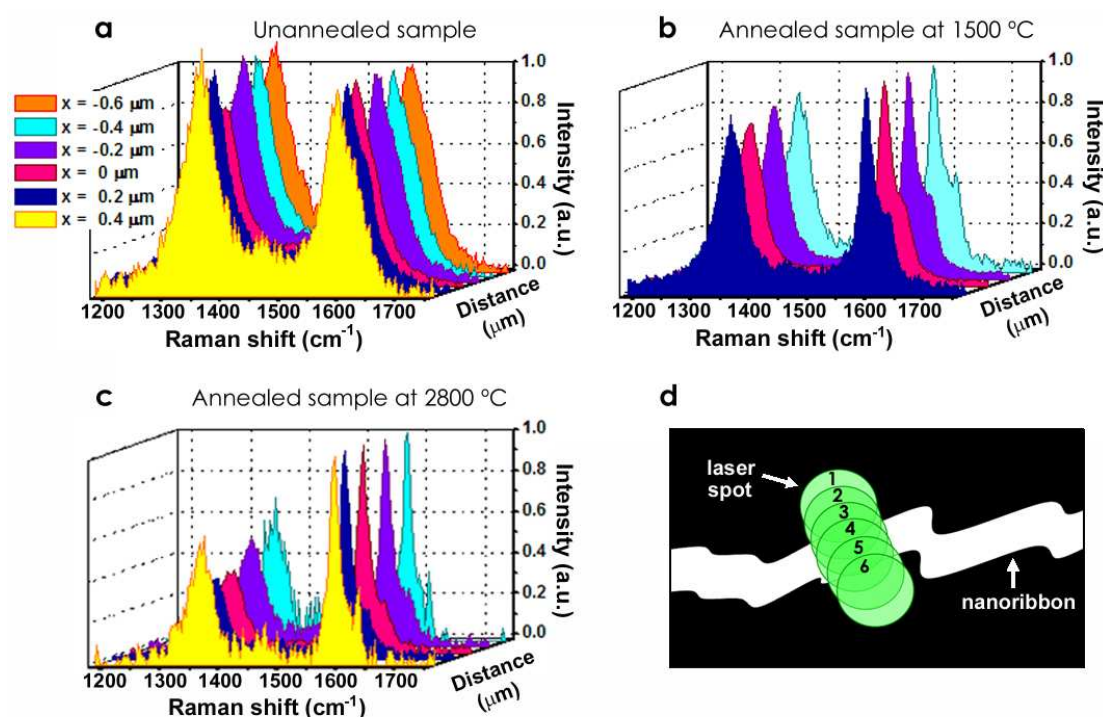


Figure 3.17 Raman spectroscopy line scans at $E_{\text{laser}} = 2.33$ eV in the range from $-0.6 \mu\text{m}$ to $0.4 \mu\text{m}$ in steps of $0.2 \mu\text{m}$ taken on individual nanoribbons: a) pristine sample, b) heat treated sample at $1500 \text{ }^\circ\text{C}$ and c) heat treated sample at $2800 \text{ }^\circ\text{C}$. d) A diagram illustrating the position of the laser spot (green circles) at each measurement across the nanoribbon. The numbers from 1 to 6 relate to the actual laser spot positions labeled in Figure 18a.

We attribute this to a higher density of disorder-inducing elements present on the ribbon edges, such as sp^3 hybridized carbon atoms, defects¹⁰ and loops (whose curvature is symmetry-breaking) in the case of the annealed samples²³.

We believe that the spectra taken at the central part of the ribbons exhibit more contributions coming from the hexagonal honeycomb planes which are perpendicular to the laser beam.

Thus, the signal intensities differ along the scan as observed in Figure 3.18a, where the intensities of the D-bands are plotted as a function of the distance across individual nanoribbons.

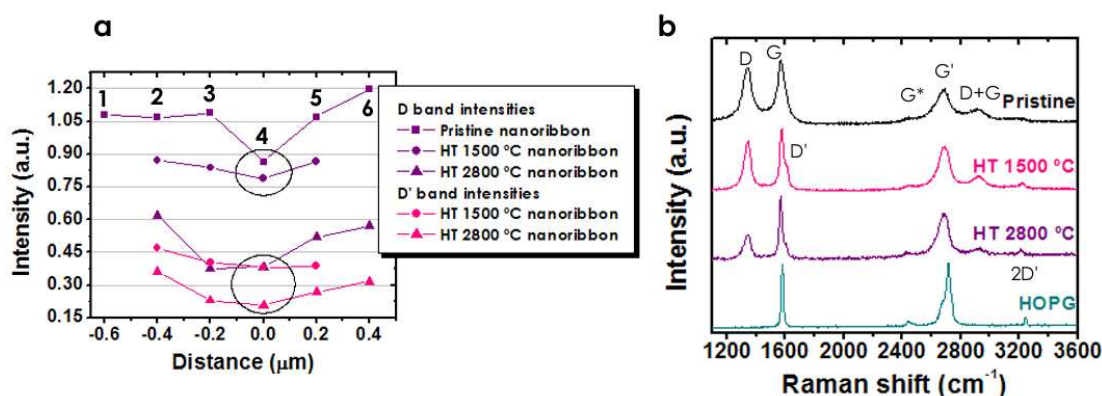


Figure 3.18 The intensities of the D- and D'- bands vs. distance in the line scan measurements on the three individual nanoribbons are plotted in a); the circled regions represent the centers of the isolated nanoribbons, and b) Raman measurements with lower D band intensities for each sample, the spectrum of HOPG is also included for comparison.

Similar to the bulk observations, we note a decrease in the D-band intensity as we go from the unannealed sample to the one annealed at 1500 °C and finally to the heat treated at 2800 °C. Figure 3.18b shows the spectrum with the lowest D-band intensity for each of the samples and the spectrum of HOPG is also shown for comparison.

The increase in annealing temperature sharpens the G, G*, G' and 2D' features, while it decreases the intensity of the disorder-induced features (D-, D'- and D+G-bands).

As we have mentioned earlier, although high temperatures were used in the heat treatments (up to 2800 °C), we still observe a residual D-band, and the shape of the G'-band indicates the inability of these samples to achieve long range AB stacking order, characteristic of highly crystalline graphitic samples.

3.4 Conclusions

We have found a new route to efficiently produce graphitic nanoribbons at atmospheric pressure. We have demonstrated that heat treatments up to 2800 °C of as-produced carbon nanoribbons anneal point defects and interstitials within individual graphene layers, thus leading to a material with a higher degree of crystallinity, in which the reactive edges of the ribbons are transformed into loops in a self-assembly process that can be strongly controlled by the variation of T_{HT} .

We have performed a detailed Resonance Raman study of heat treated nanoribbons on both bulk and individual nanoribbon samples. At the bulk level, we have confirmed a laser energy dependence of the D- and G'-bands frequency positions; and in these dependence values we found differences within the samples attributed to the annealing process.

The decrease of the I_D/I_G ratios and the FWHM of the G band as the heat treatment temperature is increased suggests an increase in crystallinity of the hexagonal honeycomb lattice, consequence of a partial graphitization process in which the stacking order could not be achieved completely possibly caused by the loop formation at the ribbon edges.

At the individual nanoribbon level, we have demonstrated that edge contributions to the Raman spectra intensify the signal of the D-band, indicating that symmetry-breaking elements such as sp^3 -like hybridized carbon atoms, structural defects and loops are present particularly in the vicinity of the edges.

However, the large number of loops present at the edges of all the ribbons is responsible for observing some residual D-band intensity.

The general up-shift of the decomposition temperature in the TGA analysis also reveals a more stable and less reactive material as T_{HT} increases in the range above which loop formation takes over.

3.5 Related Articles

- 1 . J. Campos-Delgado, H. Farhat, Y.A. Kim, A. Reina, J. Kong, M. Endo, H. Muramatsu, T. Hayashi, H. Terrones, M. Terrones, M.S. Dresselhaus. *Resonant Raman study on bulk and isolated graphitic nanoribbons*. Small DOI: 10.1002/sml.200901059
- 2 . J. Campos-Delgado, Y.A. Kim, T. Hayashi, A. Morelos-Gómez, M. Hofmann, H. Muramatsu, M. Endo, H. Terrones, R.D. Shull, M.S. Dresselhaus, M. Terrones. *Thermal stability studies of CVD-grown graphene nanoribbons: defect annealing and loop formation*. Chem. Phys. Lett. 469, 177-182, 2009
- 3 . J. Campos-Delgado, J.M. Romo-Herrera, X. Jia, D.A. Cullen, H. Muramatsu, Y.A. Kim, T. Hayashi, Z.F. Ren, D.J. Smith, Y. Okuno, T. Ohba, H. Kanoh, K. Kaneko, M. Endo, H. Terrones, M.S. Dresselhaus, M. Terrones. *Bulk production of a new form of sp^2 carbon: crystalline graphene nanoribbons*. Nanoletters 8, 2773-2778, 2008

3.6 References

- ¹ K. Nakada, M. Fujita, G. Dresselhaus, M.S. Dresselhaus. *Edge state in graphene ribbons: nanometer size effect and edge shape dependence*. Phys. Rev. B. Vol. 54, 24, 1996
- ² K.S. Novoselov, A.K. Geim, S.V. Morozov, D. Jiang, Y. Zhang, S.V. Dubonos, I.V. Grigorieva, A.A. Firsov. *Electric field effect in atomically thin carbon films*. Science. 306, 666, 2004 and K.S. Novoselov, D. Jiang, F. Schedin, T.J. Booth, V.V.Khotkevich, S.V. Morozov and A.K. Geim. *Two-dimensional atomic crystals*. PNAS. Vol. 102, No. 30, 2005
- ³ A.M. Affoune, B.L.V. Prasad, AH.Sato, T. Enoki, Y. Kaburagi, and Y. Hishoyama. *Experimental evidence of a single nano-graphene*. Chem. Phys. Lett. 348, 17, 2001
- ⁴ C. Berger, Z. Song, X. Li, X. Wu, N. Brown, C. Naud, D. Mayou, T. Li, J. Hass, A.N.Marchenkov, E.H. Conrad, P.N. First, and W.A. de Heer. *Electronic confinement and coherence in patterned epitaxial graphene*. Science. 312, 1191, 2006
- ⁵ X. Li, X. Wang, L. Zhang, S. Lee, H. Dai. *Chemically derived, ultrasmooth graphene nanoribbon semiconductors*. Science 319, 1229, 2008
- ⁶ M. Zhang, D.H.Wu, C.L. Xu, Y.F. Xu, and W.K. Wang. *Ribbon-like nanostructures transformed from carbon nanotubes at high temperature and pressure*. Nanostructured Materials. 10, 1145, 1998
- ⁷ A. G. Cano-Márquez, F. J. Rodríguez-Macías, J. Campos-Delgado, C.G. Espinosa-González, F. Tristán-López, D. Ramírez-González, D.A. Cullen, D.J. Smith, M. Terrones, Y.I. Vega-Cantú. *ExMWNTs: graphene sheets and ribbons produced by lithium intercalation and exfoliation of carbon nanotubes*. Nanoletters 9, 4, 1527-1533, 2009

-
- ⁸ D.V. Kosynkin, A.L. Higginbotham, A. Sinitskii, J.R. Lomeda, A. Dimiev, B.K. Price, J.M. Tour. *Longitudinal unzipping of carbon nanotubes to form graphene nanoribbons*. Nature 458, 2009
- ⁹ L. Jiao, L. Zhang, X. Wang, G. Diankov, H. Dai. *Narrow graphene nanoribbons from carbon nanotubes*. Nature 458, 877-880, 2009
- ¹⁰ J. Campos-Delgado, J.M. Romo-Herrera, X. Jia, D.A. Cullen, H. Muramatsu, Y.A. Kim, T. Hayashi, Z.F. Ren, D.J. Smith, Y. Okuno, T. Ohba, H. Kanoh, K. Kaneko, M. Endo, H. Terrones, M.S. Dresselhaus, M. Terrones. *Bulk production of a new form of sp^2 carbon: crystalline graphene nanoribbons*. Nanoletters 8, 2773-2778, 2008
- ¹¹ X. Jia, J. Campos-Delgado, E.E. Gracia-Espino, M. Hofmann, H. Muramatsu, Y.A. Kim, T. Hayashi, M. Endo, J. Kong, M. Terrones, M.S. Dresselhaus. *Loop formation in graphitic nanoribbon edges using furnace heating or Joule heating*. J. Vac. Sci. Technol. B 27, 4, Jul/Aug, 1996-2002, 2009
- ¹² J. Goma and M. Oberlin. *Graphitization of thin carbon films*. Thin Solid Films 65, 221, 1980
- ¹³ Y.S. Park, Y.C. Choi, K. S. Kim, D-C Chung, D.J. Bae, K.H. An, S.C. Lim, X.Y. Zhu, Y.H. Lee. *High yield purification of multiwalled carbon nanotubes by selective oxidation during thermal annealing*. Carbon 39, 655-661, 2001
- ¹⁴ I.W. Chiang, B.E. Brinson, R.E. Smalley, J.L. Margrave, R.H. Hauge. *Purification and characterization of single-wall carbon nanotubes*. J. Phys. Chem. B 105, 1157, 2001
- ¹⁵ H.R. Gutiérrez, U.J. Kim, J.P. Kim, P.C. Eklund. *Thermal conversion of bundled carbon nanotubes into graphitic ribbons*. Nanoletters 5, 2195, 2005
- ¹⁶ A.C. Dillon, K.M Jones, T.A. Bekkedahl, C.H. Kiang, D.S. Bethune, M.J. Heben. *Storage of hydrogen in single-walled carbon nanotubes*. Nature 386, 377, 1997

-
- ¹⁷ J.L. Zimmerman, R.K. Bradley, C.B. Huffman, R.H. Hauge, J.L. Margrave. *Gas-phase purification of single-wall carbon nanotubes*. Chem. Mater. 12, 1361, 2000
- ¹⁸ H. Murayama, T. Maeda. *A novel form of filamentous graphite*. Nature 345, 791, 1990
- ¹⁹ Y. Gogotsi, J.A. Libera, N. Kalashnikov, M. Yoshimura. *Graphite polyhedral crystals*. Science 290, 317, 2000
- ²⁰ M. Endo, B.J. Lee, Y.A. Kim, Y.J. Kim, H. Muramatsu, T. Yanagisawa, T. Hayashi, M. Terrones, M.S. Dresselhaus. *Transitional behaviour in the transformation from active end planes to stable loops caused by annealing*. New Journal of Physics 5, 121.1, 2003
- ²¹ Z. Liu, K. Suenaga, P.J.F. Harris, S. Iijima. *Open and closed edges of graphene layers*. Phys. Rev. Lett. 102, 015501, 2009
- ²² M. José-Yacamán, H. Terrones, L. Rendón, J.M. Domínguez. *Carbon structures grown from decomposition of a phenylacetylene and thiophene mixture on Ni nanoparticles*. Carbon 33, 669, 1995
- ²³ J. Campos-Delgado, Y.A. Kim, T. Hayashi, A. Morelos-Gómez, M. Hofmann, H. Muramatsu, M. Endo, H. Terrones, R.D. Shull, M.S. Dresselhaus, M. Terrones. *Thermal stability studies of CVD-grown graphene nanoribbons: defect annealing and loop formation*. Chem. Phys. Lett. 469, 177-182, 2009
- ²⁴ T.C. Chieu, M.S. Dresselhaus. *Raman studies of benzene-derived graphite fibers*. Phys. Rev. B 26, 10, 1982
- ²⁵ A.M. Rao, A.W.P. Fung, M.S. Dresselhaus, M. Endo. *Structural characterization of heat-treated activated carbon fibers*. J. Mater. Res. 7, 7, 1788-1794, 1992
- ²⁶ M. Terrones, PhD. Thesis, University of Sussex, Sussex, UK, 1997
- ²⁷ C. Jin, K. Suenaga, S. Iijima. *Vacancy migrations in carbon nanotubes*. Nanoletters 8, 1127, 2008

-
- ²⁸ S.V. Rotkin. *SWNT nucleation: energetics of zipping-edge mechanism*. Mat. Res. Soc. Symp. Proc. 675, W2.9.1, 2001
- ²⁹ M.S. Dresselhaus. G. Dresselhaus. K. Sugihara, I.L. Spain, H.A. Goldberg. Springer Series in Materials Science Vol. 5. Graphite Fibers and Filaments. Springer-Verlag, New York/Berlin/Heidelberg, 1988.
- ³⁰ R. Saito, A. Grüneis, G.G. Samsonidze, V.W.Brar, G. Dresselhaus, M.S. Dresselhaus, A. Jorio, L.G. Cançado, C. Fantini, M.A. Pimenta, A.G. Souza-Filho. *Double resonance Raman spectroscopy of single-wall carbon nanotubes*. New Journal of Physics 5, 157.1-157.15, 2003
- ³¹ L.G. Cançado, K. Takai, T. Enoki, M. Endo, Y.A. Kim, H. Mizusaki, A. Jorio, L.N. Coelho, R. Magalhães-Paniago, M.A. Pimenta. *General equation for the determination of the crystallite size L_a of nanographite by Raman spectroscopy*. Appl. Phys. Lett. 88, 163106, 2006
- ³² R. P. Vidano, D. B. Fischbach, L. J. Willis, T. M. Loehr. *Observation of Raman band shifting with excitation wavelength for carbons and graphites*. Solid State Communications 39, 341-344, 1981
- ³³ M. J. Matthews, M.A. Pimenta, G. Dresselhaus, M.S. Dresselhaus, M. Endo. *Origin of the dispersive effects of the Raman D band in carbon materials*. Phys. Rev. B 59, 10, 6585, 1999
- ³⁴ P. Lespade, A. Marchand, M. Couzi, F. Cruege. *Caracterisation de matériaux carbonés par microspectrometrie Raman*. Carbon 22, 4/5, 375-385, 1984

4. *In situ* reconstruction of graphitic nanoribbons by Joule heating

The process by which electric current is passed through a conductor releasing heat is called Joule heating. This phenomenon was first studied by James Prescott Joule in 1841. He deduced that the heat produced was proportional to the square of the current, multiplied by the electrical resistance of the conductor.

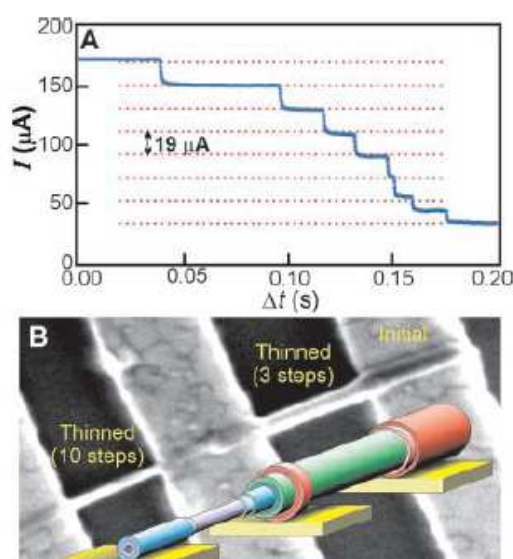
$$Q \propto I^2 \cdot R$$

This relationship is known as Joule's law¹.

Joule heating has provided an efficient way to achieve high temperatures in many carbon materials, and it has been demonstrated that carbon nanostructures could be modified substantially by Joule heating.

In 2001 Avouris and co-workers², reported the breakdown of single shells of multiwall carbon nanotubes (MWNTs) under a constant high bias regime. The removal of carbon shells from these conductors was observed both electrically and with the use of atomic force microscopy after the experiment (see Figure 4.1).

Figure 4.1 (A) The partial electrical breakdown of a MWNT at constant voltage stress proceeds in a series of discrete steps corresponding to the loss of individual carbon shells from the MWNT. Equally spaced dotted lines emphasize the surprisingly regular spacing. (B) Images of partially broken MWNTs show clear thinning, with a decrease in radius equal to the intershell spacing (0.34 nm) times the number of completed breakdown steps. The two segments of this sample were independently thinned by 3 and 10 shells, as depicted by the color overlays (Extracted from Reference 2).



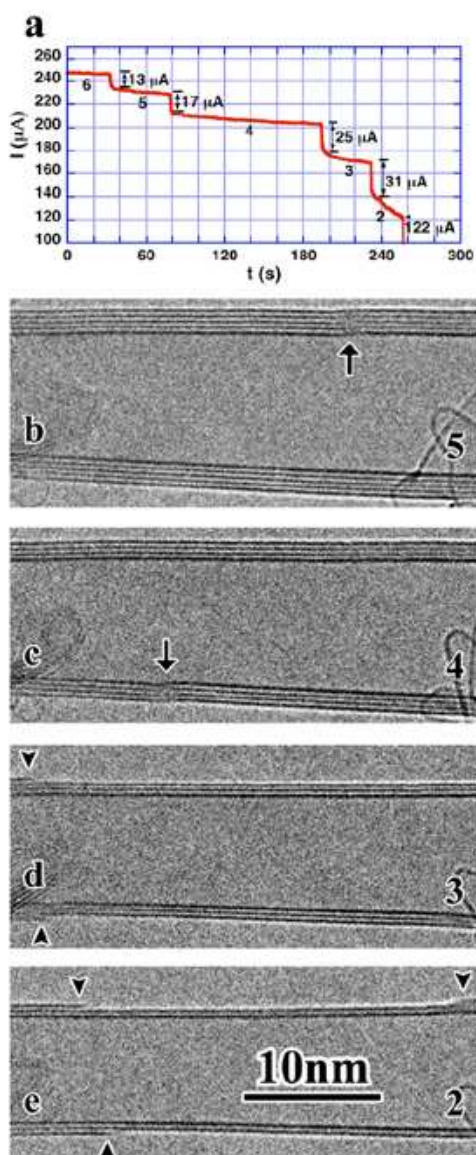


Figure 4.2 (a) The current time ($I-t$) curve of the breakdown of the MWNT shown in panels b-e. The numbers below the plateau indicate the total wall number. (b)-(e) Sequential HRTEM images showing that the walls of the six-wall nanotube are removed wall-by-wall from the outermost wall (b) to the innermost wall (e). The numbers indicate the total number of walls. The arrows mark kinks. The arrowheads denote the residue of the 4th and the 3rd walls after breakdown.³

Electrically, the breakdown of a single carbon shell results in a partial conductance drop that typically occurs within a few milliseconds. When stressed at sufficiently high bias, multiple independent drops occur as one carbon shell after another is broken. The resulting staircase of current as a function of time is shown in Figure 4.1A, as eight shells of a MWNT are sequentially removed. Atomic force microscopy (AFM) was used to resolve the gradual thinning of the studied MWNT (see Figure 4.1B). Although in this work the primary factor of the breakdown was attributed to current-induced defect formation and not to the Joule heating effect, a latter report by Huang *et al.*³ proved that the breakdown of the tubes originated from heat-stimulated imperfections.

The Joule heating experiments by Huang and co-workers were conducted inside a transmission electron microscope, which allowed a real time observation of the structural transformations occurring to the MWNT. For this experiment, a multiwall carbon nanotube was end contacted and kept free standing in high vacuum (10^{-8} Torr), inside a HRTEM equipped with a scanning tunneling microscopy (STM) probe. In such an arrangement, atomic-scale imaging and $I-V$ measurements were carried out concurrently for the first time.

When passing a current of 240 μA , breakdown occurs at the midpoint of the nanotube, resulting in the formation of a clean six-wall nanotube segment, which was eliminated wall-by-wall by electric breakdown. The loss of one wall under a constant bias of 3 V results in an instant current drop, as shown in Fig. 4.2a. The current drops are approximately 13, 17, 25, and 31 μA for the 6th, 5th, 4th, and 3rd wall breakdown (the innermost wall is labeled as the first wall), respectively.

The sequential wall-by-wall breakdown was recorded by HRTEM. Figure 4.2b-e shows clearly that one wall is removed after each current drop, and each wall is removed sequentially from the outermost wall (5th) to the innermost wall (2nd).

HRTEM indicates that the breakdown eventually results in the formation of a double-wall nanotube. Their observation (Figure 1) that the breakdown is initiated in the middle of the nanotube (not in the contacts) indicates that it is caused by resistive heating. This is also supported by the defect generation and migration along the nanotubes.

Typical defects observed are kinks, holes, and sliding between different walls. These are apparently heat-stimulated imperfections.

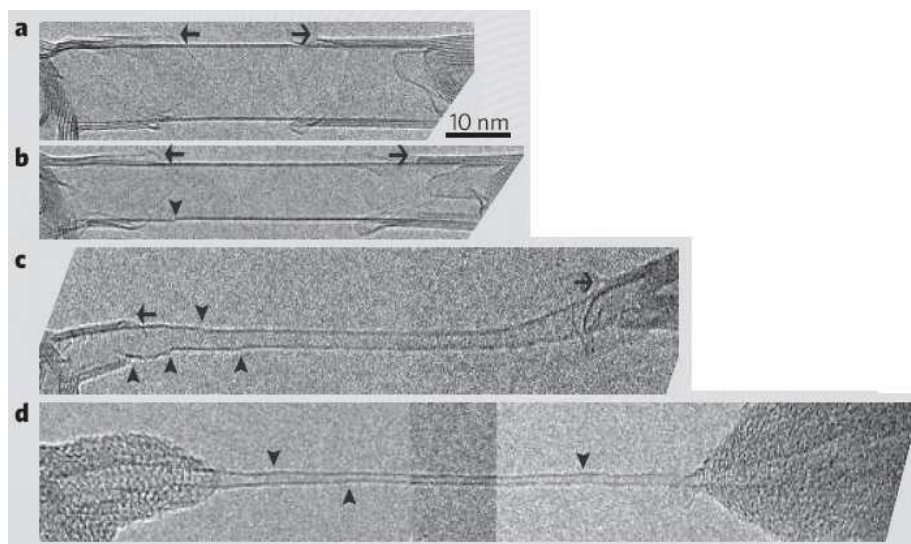


Figure 4.3 a-d Tensile elongation of a single-wall carbon nanotube under a constant bias of 2.3 V (images are scaled to the same magnification). Arrowheads mark kinks; arrows indicate features at the ends of the nanotube that are almost unchanged during elongation. (Extracted from Ref. 4)

From the lattice spacing of 4 Å, they estimate that the temperature in the middle of nanotube is between 2000 and 3000 °C at the breakdown voltage of 3 V.

From the Fourier law, the middle section of the nanotube is the hottest spot; therefore it is not difficult to understand that the breakdown occurs in the middle of the nanotube, starting either from the outermost wall or from the innermost wall.³

The same set-up was used by Huang *et al.* in 2006 to prove the superplastic properties of carbon nanotubes⁴ and to achieve the formation of nanotubes from amorphous carbon nanowires⁵.

Huang and coworkers showed that, at high temperatures, individual SWNTs can undergo superplastic deformation, becoming nearly 280 % longer and 15 times narrower before breaking.

In their experiment, a SWNT with an initial length of 24 nm (Figure 4.3a) was formed in situ by the electrical breakdown of a multwalled carbon nanotube inside a high resolution transmission electron microscope equipped with a piezo manipulator (STM tip).

The piezo manipulator was used to pull the SWNT to increase the strain (Figure 4.3 b-d), at a constant bias of 2.3 volts. At tensile failure, the SWNT was 91 nm long, showing a tensile elongation of 280 %; its diameter was reduced 15-fold, from 12 to 0.8 nm.

During deformation at a bias of 2.3 V, the temperature is estimated to be more than 2000 °C. At such high temperatures, the nanotube seems to be completely ductile. Kinks and point defects are fully activated, resulting in superplastic deformation impossible at low temperatures.

Kinks form frequently during tensile straining (Figure 4.3 b-d), and these kinks propagate along the tube and then pile up (Figure 4.3d) or disappear at the ends.

The kink motion is evidence of kink mediated plasticity at high temperatures. The nanotube narrows immediately after the kink passes.

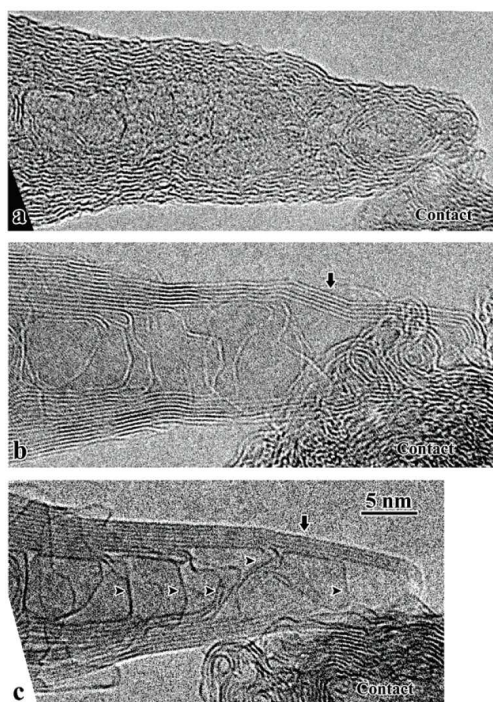


Figure 4.4 Crystallization of a disordered nanotube caused by an I-V measurement. a) a nanotube with disordered wall structures. b) crystallization of a) caused by making an I-V measurement, c) the graphitization of b) was improved after holding at a high power (350 μ W) for 3 min. (Extracted from Reference 5).

In situ formation of nanotubes was accomplished when nanowires of amorphous carbon were deposited by the electron-beam on the STM tip.

After growth, the nanowire was bonded to another electrode by deposition of amorphous carbon between the nanowire tip and the electrode and then resistively heated to temperatures higher than 2000 $^{\circ}$ C by applying a high-bias voltage.

The high temperatures promoted the graphitization of the structure, leading to the formation of concentric nanotube walls (see Figure 4.4). These experiments helped to understand the dynamics of the non-catalytic growth of carbon nanotubes.

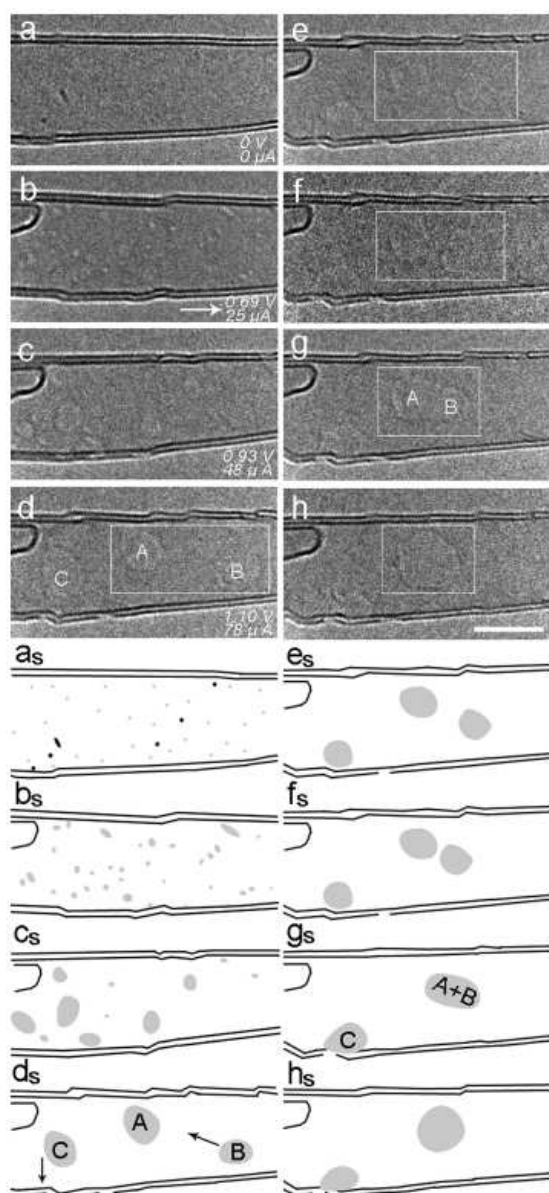


Figure 4.5 Time sequential HR-TEM images for the formation, migration, and coalescence of large vacancies in a DWNT (a–h) and their respectively schematic images (a_s–h_s). Scale bar = 5 nm.

The Japanese group led by Iijima⁶, reported in 2008 the formation and dynamics of vacancies in carbon nanotubes in a Joule heating regime.

Figure 4.5 illustrates the experiment they performed, where a double wall carbon nanotube was first damaged by electron beam irradiation (Figure 4.5a, no voltage is applied), creating adatoms (black spots) and monovacancies (white spots). When a voltage up to 0.7 V was gradually applied, most of the dark spots are wiped out although the bright spots remain there, as shown in Figure 4.5b (also shown schematically in Figure 4.5b_s).

In addition to the disappearance of carbon adatoms and clusters, a few vacancies with an enlarged size were newly formed on the nanotube wall (Figure 4.5b). They might correspond to multivacancies such as di-, triple-, or octavacancies created either by the coalescence of nearby monovacancies or through the further carbon loss around the monovacancies. When they further raised the temperature by increasing the input voltage to 1.1 V (a current about 78 μA), most of the smaller vacancies disappeared and no more obvious carbon adatoms or clusters (dark contrast spots) could be observed, as shown in Figure 4.5c (also shown schematically in Figure 4.5c_s).

Instead, a few even larger vacancies with a diameter of about 1–2 nm were created, corresponding to tens of carbon atoms loss. They were mostly formed due to the coalescence of those mobile smaller vacancies in neighboring hexagons.

Examples of even larger vacancies are given in Figure 4.5d-h (also shown schematically in Figure 4.5d_s-h_s), where particular attention is paid on three large vacancies marked as A, B, and C respectively in Figure 4.5d. Vacancies A and B are separated by a center-to-center distance of about 7 nm at $t = 170$ s (Figure 4.5d). Vacancy B migrates toward A, and vacancy C migrates downward to the sidewall, while vacancy A strolls around its original position. The migration of vacancies B and C is quite smooth, and they do not cause any massive structural distortions on the nanotube walls. Although each of them is trying to keep an energy-favored round shape and their edge-shapes are slightly and frequently changing, suggesting the diffusion of carbon atoms through the edge would become easier at this high temperature. It takes about 18 s for vacancy B to arrive at vacancy A.

Once they get in touch, coalescence starts gradually and a narrow neck forms between them. Within 0.5 s, the coalescence process is completed and a much larger hole is formed. Soon after, the edge of the hole is annealed again into a round-shaped one with a diameter of about 4 nm, and its surface area is roughly equal to the sum of vacancies A and B.

More importantly and surprisingly, this large hole is still mobile. It moves upward and finally migrates to the left end of this DWNT (images not shown here). When it reaches the sidewall, we could recognize that the large hole lies in the outer shell of the DWNT because a portion of the outer wall disappears, not the inner wall, and consequently so do vacancies A, B, and C.

Note that this newly formed large hole could survive without any splitting, even at room temperature after removing the applied voltage. In the above experiments, we find the vacancies in the outer wall are definitely more likely to migrate. This is reasonable because most of the current is supposed to flow through the outmost

shells, therefore the “hotter” outer wall is more favorable for the formation and migration of vacancy, and a CNT with a larger diameter is more likely to accommodate a large vacancy due to the weakened curvature effect. The presence of inner wall is also playing a key factor here. When a large hole is formed on the outer wall by losing tens of carbon atoms or even more, the outer shell is hardly able to reconstruct by diameter shrinkage because of the existence of inner walls.

By adopting the previously proposed thermal conductivity for a suspended CNT, the temperature on the CNT is estimated to range from ~1000 to ~1800 K. For the migration of the vacancy B in Figure 4.5, we know the traveling distance within a given time (about 7.3 nm for 18 s). The calculated vacancy migration speed is 0.4 nm/s.

The Joule heating experiments on our graphitic nanoribbons that we will describe in this chapter were conducted using the facilities of the Department of Physics in Boston College in Boston, Massachusetts, USA.

The experiments that we have carried out in this system have provided two different and interesting results. On one hand, we were able to produce for the first time atomically smooth zigzag or armchair edges from defective rough edges present in graphite nanoribbons, by applying a controlled voltage⁷.

On the other hand, the increment in temperature induced loop formation between adjacent sheets⁸ (single-, double- and multiple-loops), as described previously for the furnace heating experiments (see Chapter 3 section 3). We will describe in detail both processes and list the differences in sample preparation that lead to each phenomenon.

4.1 Conditions of the experiment

Resistive Joule heating experiments on the graphitic nanoribbons were carried out using an integrated STM-TEM system (a JEOL 2010F HRTEM integrated with a Nanofactory STM holder) which is further attached to a piezoelectric stage that allows us to move the tip in all 3 (x , y , z) directions (see Figure 4.6).

The STM tip and sample holder also serve as two electrodes.

The as-prepared nanoribbon sample is placed in between the STM tip and the sample holder, and a controlled bias voltage was applied across the ribbon.⁸

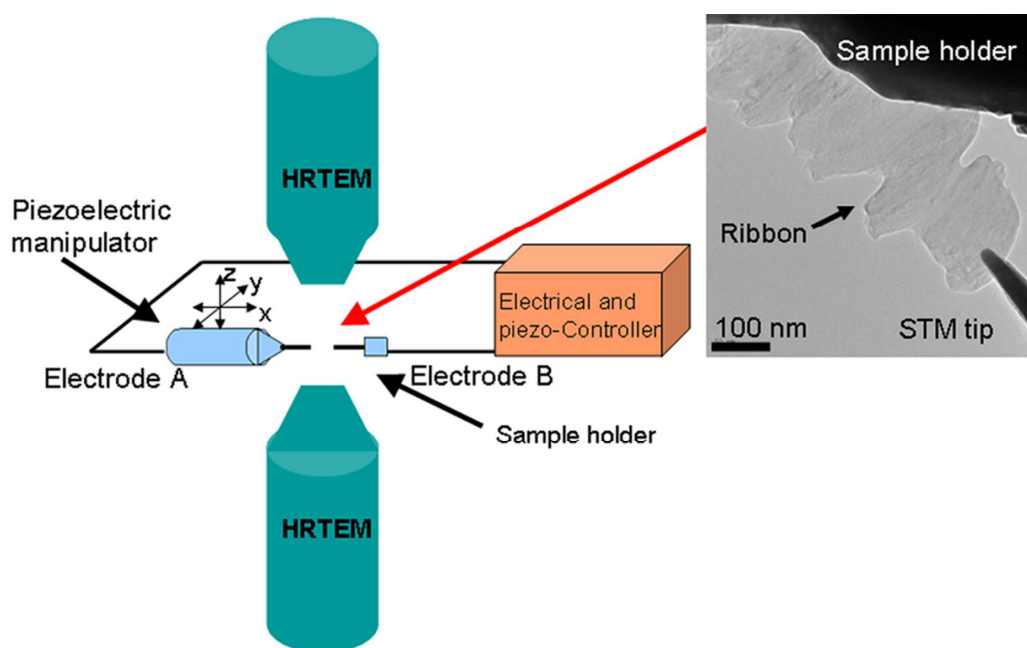


Figure 4.6 A schematic diagram of the TEM-STM system. The inset on the right shows a low magnification TEM image of a nanoribbon piece placed in between two electrodes (the sample holder and the STM tip).⁸

4.2 Crystallization and sharp edge formation

A short and narrow graphitic nanoribbon (315 nm long and 66 nm wide) was placed inside the Joule heating set-up described above (inset of Figure 4.8A), before a controlled voltage was applied, the structure of the nanoribbon was intentionally damaged through irradiation of the electron beam for a long-time period (~15 min). The effects of this irradiation are evident in Figure 4.8A in the left-hand panel and Figure 4.10A, where the structure of the nanoribbon before the Joule Heating experiment is shown.

Comparing this image with the pristine nanoribbon morphology (Figure 3.3 b and c, Figure 3.8 Pristine) we can not help noticing that the sheets edges became irregular and unparallel probably due to the evaporation of C species, triggered by e-beam irradiation.

Once a controlled bias voltage was applied through the nanoribbon, the effects induced by Joule heating were monitored by HRTEM and by changes in the current vs. voltage (I-V) curves. The material behaved like a metal (straight line for the I-V curves) following Ohm's law.

As we applied a voltage (up to 1.6 V) over the length of the ribbon, the I-V curve, depicted in Figure 4.7A, showed three distinct regimes: i) a linear regime from 1 to 1.25 V (which lasted 7 min and 30 sec), ii) a slowly increasing slope regime from 1.25 to 1.6 V (for ~ 2 min), and iii) a rapidly increasing slope regime at 1.6 V (for a lapse of ~ 27 minutes). In the nonlinear regime at 1.6 V, the resistance decreases with increasing input energy, this tendency is observed in Figure 4.7B, where resistance versus input energy is plotted. As current flows at an applied voltage of 1.6 V, a restructuring process takes place, where the degree of crystallinity of the ribbon improves rapidly causing the resistance values to drop (Figures 4.8D and 4.9), and the sample thickness decreases, until all the graphene layers evaporate and the sample breaks from the middle (Figure 4.9C).

During the experiment, linear I-V sweeps were performed. Figure 4.8 shows representative images at different stages of the experiment (left-hand panels) and their corresponding I-V curves (right-hand panels).

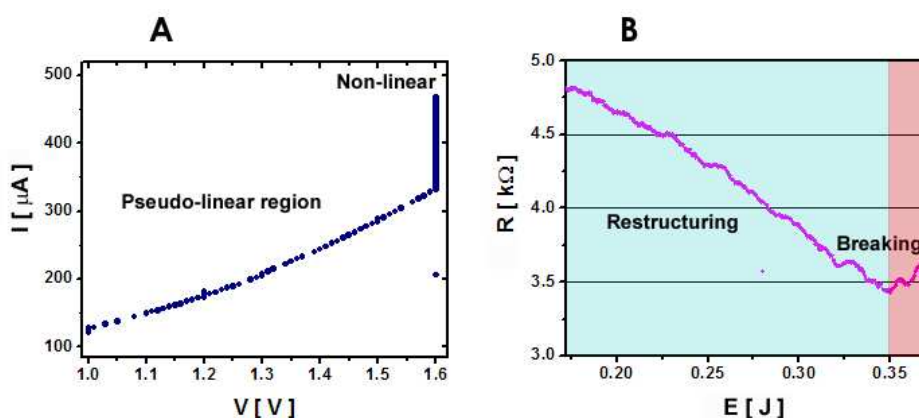


Figure 4.7 A) I vs. V curve during Joule heating, indicating three regimes: i) a linear regime from 1 to 1.25 V, ii) a slowly increasing slope regime from 1.25 to 1.6 V, and iii) a rapidly increasing slope regime at 1.6 V. B) Resistance versus input energy at 1.6 V applied bias (Adapted from Ref. 6).

Before Joule Heating (Figure 4.8A) the structure, as described before, was damaged by the electron beam and consisted of graphene sheets with irregular and unparallel edges. The resistance value at this point corresponds to 20 k Ω .

When 1 V of bias voltage was applied (Figure 4.8 B and C), the structure of the nanoribbon suffered major transformations, a progressive crystallization process started taking place at this voltage, the irregular lines representing the sheets edges seen in Figure 4.8B commence to straighten up and align in Figure 4.8C; the transformations are also reflected in the change of resistance values, dropping from 11.4 k Ω to 10.5 k Ω . During the highest voltage regime (1.6 V, Figure 4.8D) the sample decreases its resistance value to 9.1 k Ω and below, graphitization is fully achieved and we observe a defect-free honey-comb structure and the formation of sharp edges (Figure 4.9b). Arrays of zig-zag (armchair) edges are formed and the evolution of AA- to AB- stacking order is also achieved.⁷

We believe that the high temperatures induced by Joule Heating are responsible for the crystallization process. The e-beam irradiation played also a crucial role in the sharp edge formation as described above. Both effects combined, eventually led to the rupture of the nanoribbon (Figure 4.9C).

At high applied voltages (1.6 V), the preferred reconstruction-crystallization effects induced by the high temperature caused by Joule heating are seen in going from Figure 4.10 A to B.

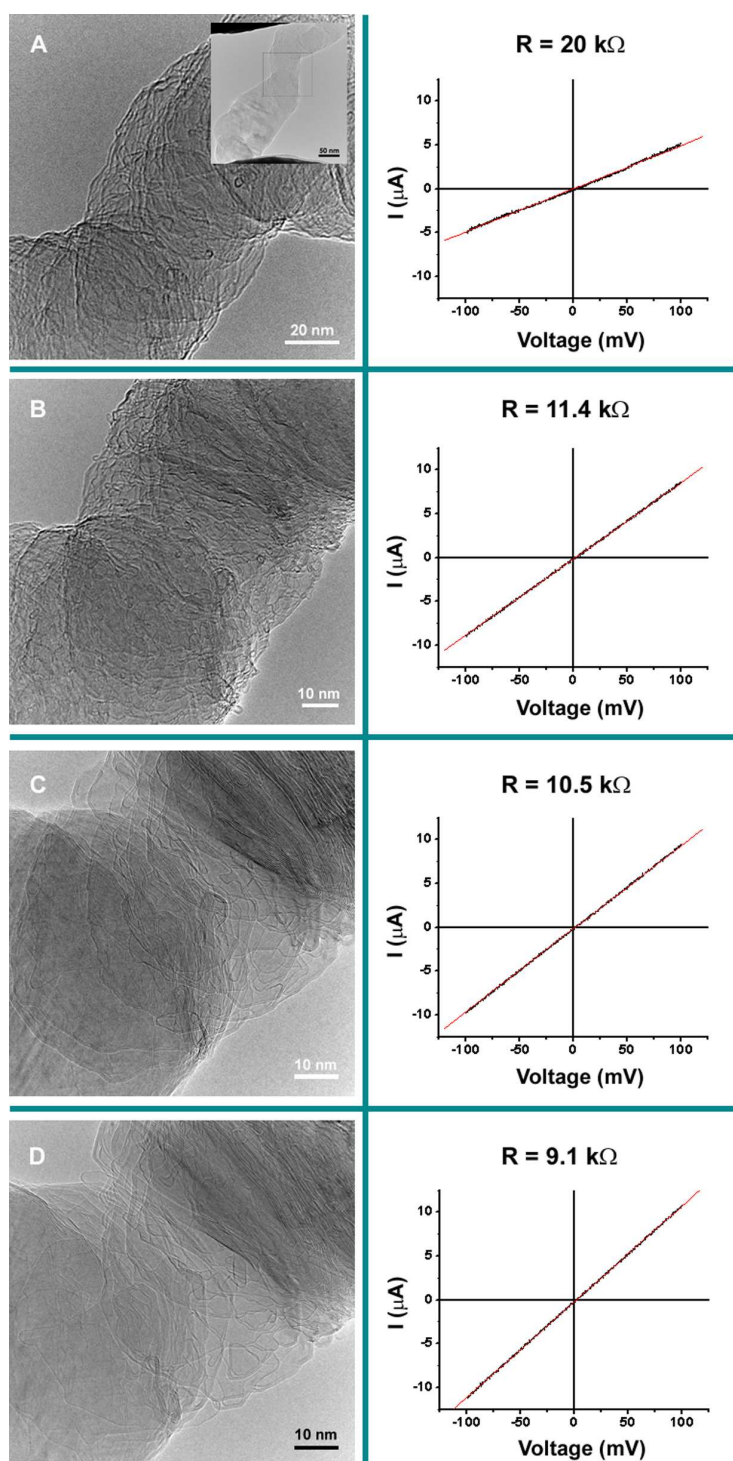


Figure 4.8 Representative HRTEM images at different stages of the experiment (left-hand panels) and their corresponding I-V curves (right-hand panels). A) before Joule Heating, the inset in the left panel shows the nanoribbon attached to both electrodes, B) and C) at an applied voltage of 1 V, D) at an applied voltage of 1.6 V. Resistance values are calculated by fitting linearly the data and taking the inverse of the slope values.

The well-resolved HRTEM images allowed us to determine the edge configuration by looking at the hexagons orientation (see Figures 4.9B and 4.10D). Before Joule heating the edges seen in the material are irregular and very few correspond to zigzag (pink lines) or armchair segments (green lines). After 10 min of annealing at 1.6 V, the reconstruction process induced the formation of straight edges in either armchair or zigzag configurations, indicating that the activation energy of atoms forming zigzag or armchair edges is lower than for other edge configurations. Other types of edges are seen infrequently because a mixture of zigzag and armchair edges is metastable due to an energy penalty at the edge junctions.

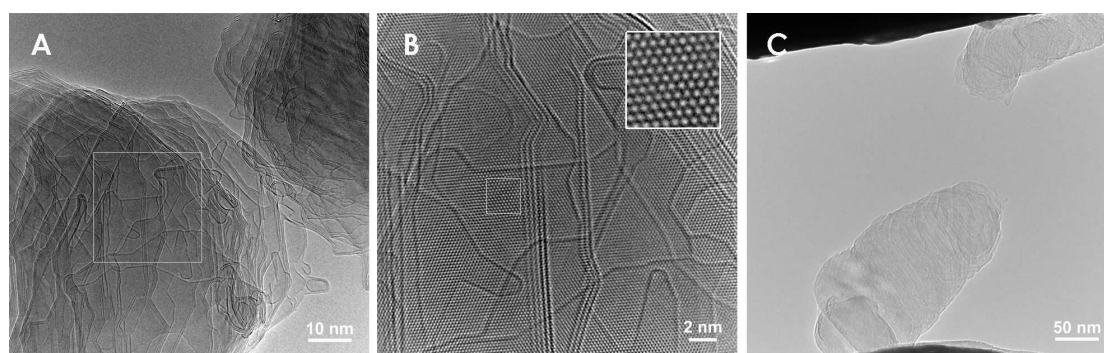


Figure 4.9 TEM images of the Joule Heating experiment at an applied bias voltage of 1.6 V. A) Image of the nanoribbon before rupture, B) high resolution image of the selected area in A; the inset shows a detail of the marked region where the highly crystalline honey-comb lattice of carbon atoms is evident. C) Low resolution image of the nanoribbon after rupture.

Figure 4.10D depicts the reconstructed graphitic material shown in Figure 4.10B. The measured in-plane lattice spacing for our ribbons is 0.24 ± 0.02 nm, consistent (within the accuracy of our TEM measurements) with literature values for graphite [which is $\sqrt{3} a_{c-c}$, where a_{c-c} is the nearest-neighbor carbon-to-carbon distance⁹]. As a result of carbon atom vaporization and Joule heating, the defective graphitic edges in the as-grown nanoribbon sample crystallize and finally become atomically sharp and highly crystalline. The maximum length of the smooth edges observed after the process in Fig. 4.10C is ~ 29 nm. The mechanism of reconstruction or crystallization for the nanoribbons and edges is attributed primarily to the initial edge configuration of the material (irregular and unparallel), carbon atom

vaporization, the current flow along the ribbon and edges, and the high temperature associated with the resistive Joule heating.

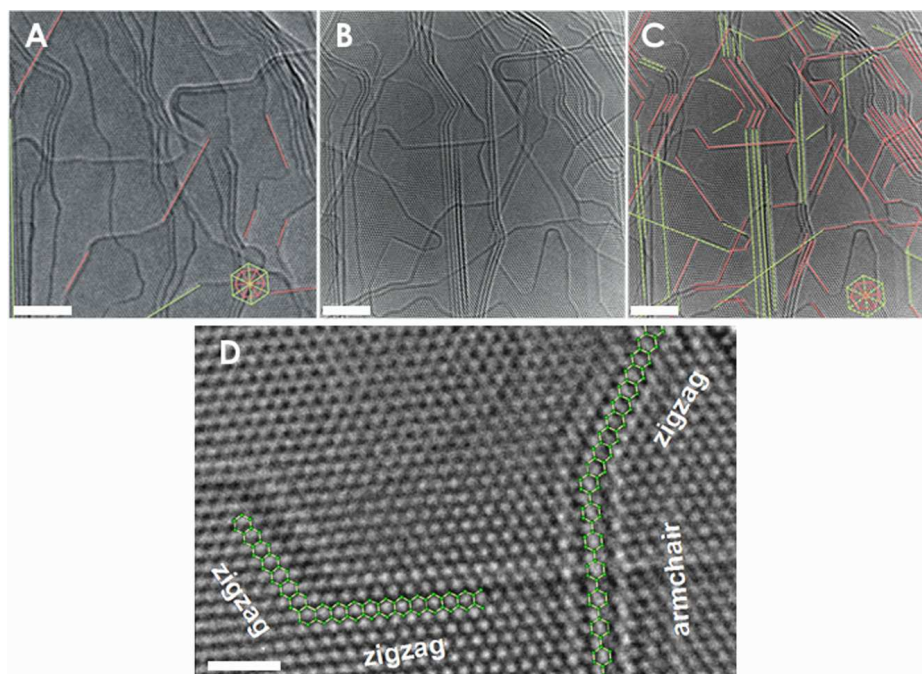


Figure 4.10 Crystallization and edge formation in graphitic nanoribbons. A) Nanoribbon sample before Joule heating, showing very few zigzag (pink lines) and armchair edges (green lines). B) The same ribbon sample after Joule heating (for 10 min at 1.6 V), in which most of the edges seen are either zigzag or armchair edges, as indicated in C). The inset hexagons indicate the zigzag- or armchair-edge orientations associated with the lattice patterns in A) and C). D) High-magnification image of the annealed sample showing that well-defined zigzag-armchair and zigzag-zigzag edges are formed. Scale bars in A), B) and C), 4 nm; in D), 1 nm (Adapted from Reference 7).

The graphitization steps of carbon at high temperatures have been described by Goma and Oberlin¹⁰. According to their observations, the graphitization process happens in two phases, 1) a pregraphitization stage, below 2000 °C, where small mosaic elements about 10 Å in size become associated in an almost parallel alignment with tilt and twist boundaries to form distorted layers; 2) above 2000 °C dewrinkling of carbon layers occurs and L_a (the in-plane crystallite size) increases markedly, triperiodic order is achieved. For our ribbon samples, we observed the transformation of AA stacking into ABAB stacking, and we attribute these

transformations mainly to the high temperatures reached (above 2000°C) in the nonlinear voltage regime. The dynamics of the edge reconstruction are shown in Fig 4.11, A to D. In this figure we see a time resolved sequence of a three layered graphene edge structure placed on top of another few-layered graphene sheet with a zigzag-armchair-zigzag-armchair edge configuration forming 150° angles (note that the angles between zigzag and armchair edges can be 30°, 90°, or 150°). As we apply a bias voltage of 1.6 V (reaching high annealing temperatures), the armchair edge above the zigzag edge starts to evaporate, resulting in the upward movement of the zigzag edge (red arrows) with a speed of 2.3 nm/min. This low speed at the investigated high temperatures indicates that the necessary activation energy is much larger than the activation energy of defect migration observed by Jin *et al.*⁶ in carbon nanotubes.

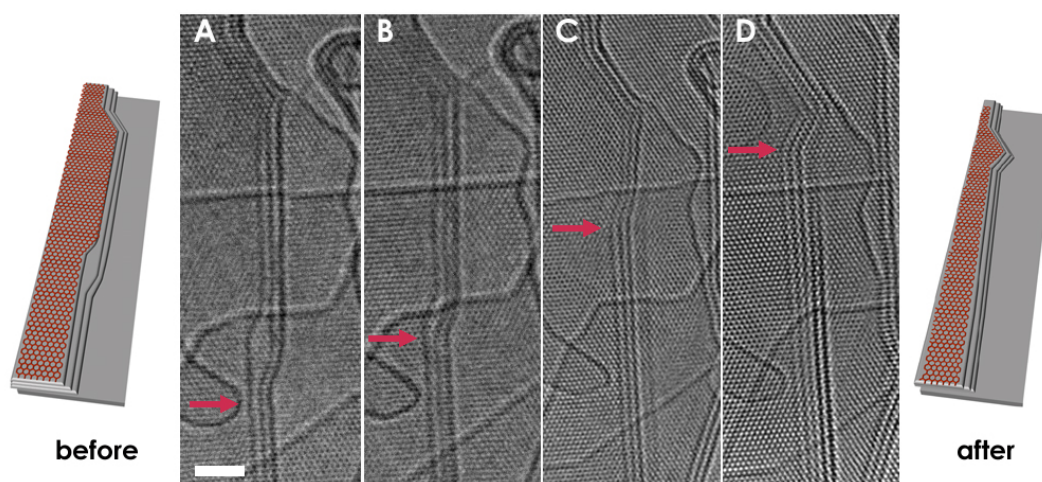


Figure 4.11 Edge motion under Joule heating. A) Three-layer zigzag-armchair-zigzag-armchair edge array. The red arrows indicate the position of the zigzag-armchair edge junction. After some time of Joule heating, the junction moves up [B and C], keeping the short zigzag-edge length almost unchanged. Eventually, the zigzag edge joins with the upper zigzag edge, forming a stable zigzag-zigzag-armchair edge array (D). The sketches on the left of A) and on the right of D) are simulated structures of A) and D), respectively. Scale bar in A, 2 nm.⁷

Eventually, as shown in Figure 4.11D, the armchair edge is eliminated, and the lower zigzag edge joins with the upper zigzag edge and forms a stable zigzag-zigzag junction.

Joule heating involves both current flow and atomic vibrations. Point (localized) defects are associated with large amplitude vibrations, and these are likely to be annealed first. In addition, zigzag edged graphene ribbons are the only graphene structures which have electronic states that are localized along their edges¹¹.

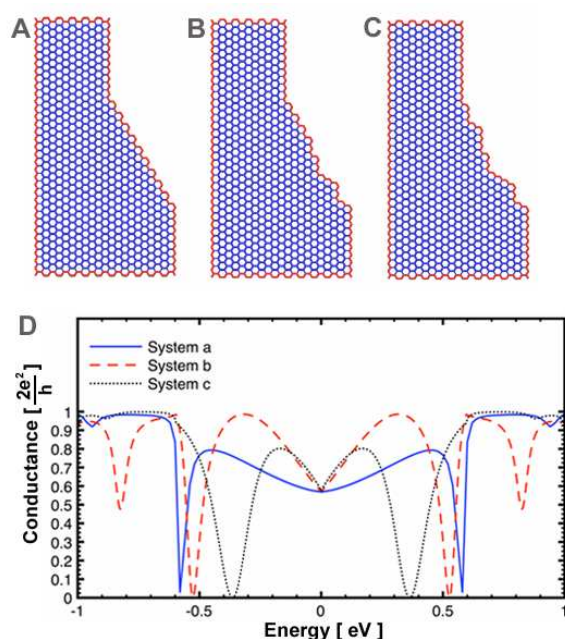


Figure 4.12 Transport properties of graphene nanoribbon heterojunctions based on a single π -orbital tight-binding model (the Fermi energy is located at $E=0$ eV). A) to C) Three models considered here, where the details of the edges are highlighted in red. In each case, the two electrodes consist of two zigzag-edge nanoribbons. The conductance corresponding to systems A) to C) is presented in D. (Adapted from Ref. 7).

Because the electronic dispersion is quite large, the electronic flow in zigzag-edged nanoribbons occurs mainly along these zigzag edges. When a zigzag edge meets a non-zigzag edge, the electronic flow is reduced, and the system acts as if a large resistance were introduced at the junction.

Therefore, heating will result and will cause electron flow away from the edge junction or, if enough energy is dissipated at the junction, will result in a modification of the structure. In that case, provided that sufficient energy is dissipated in this manner, the atomic structure will rearrange locally until electronic flow is reestablished. Starting from a zigzag edge, this can take place if the structure is annealed into a zigzag edge. For this reason, zigzag-zigzag junctions are the favored junction formation (Figure 4.11). This zigzag edge formation mechanism is therefore local, because it is due to a high local resistance at the edge intersection. The conductance of the heterojunctions between zigzag and armchair edges is considerably reduced because of the fact that transmission is hindered on those non-zigzag edges where no electronic state is present.

The Joule annealing process and its associated current flow create stable “edge arrays” (see Figures 4.10C and 4.11 A-D). These edge arrays indicate that an offset is present between the edges of two adjacent layers. The results of a careful measurement of the edge-to-edge distances in these edge arrays is plotted in Fig. 4.13a, which shows clear peaks at 0.34-, 0.38-, and 0.43-nm edge-to-edge distances.

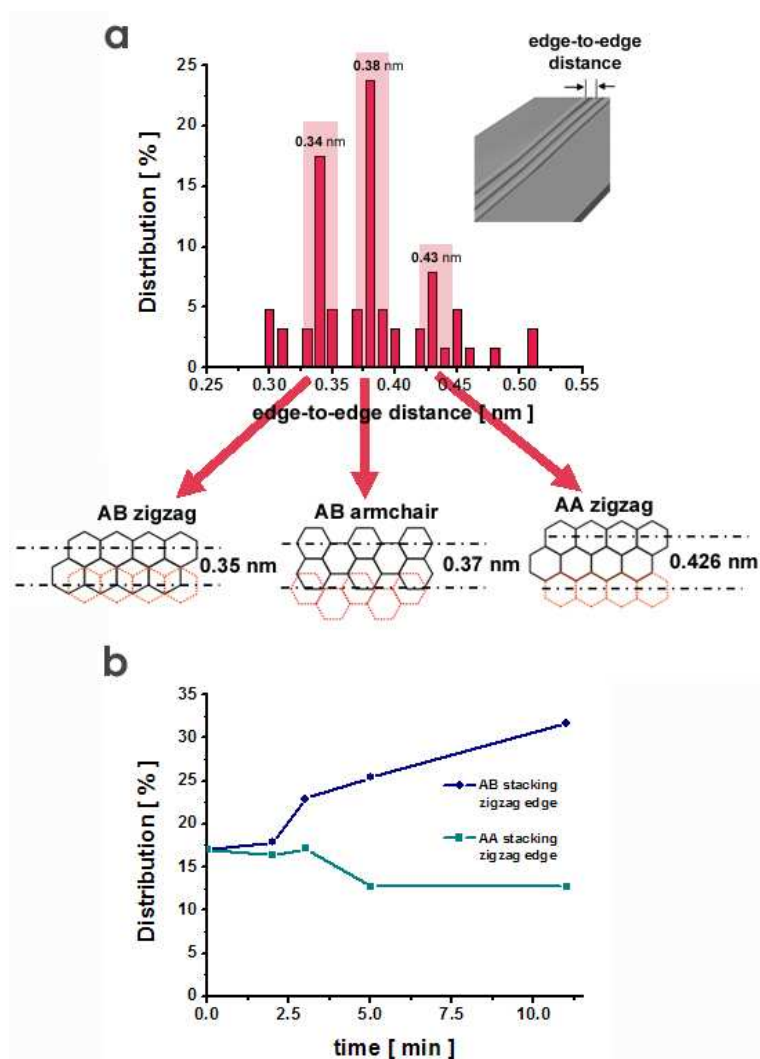


Figure 4.13 Edge arrays and their time evolution. a) The experimental edge-to-edge distances in the edge arrays show three main peaks at 0.34, 0.38 and 0.43 nm. These peaks correspond to the separation (off-set) of the two adjacent AB stacked zigzag edges, AB stacked armchair edges, and AA stacked zigzag edges, respectively, as indicated in the inset of a). b) Time evolution of the stacking of all the edges obtained from analysis of Figure 4.9. Error of points is 2%.⁷

These distances correspond to the offset of adjacent edges of differently stacked graphene layers (AB zigzag, AB armchair, AA zigzag). Of particular interest, the evolution of the edge arrays (Fig. 4.13b) after 10 min of irradiation and Joule annealing shows a clear increase for the AB stacked zigzag edges and a decrease of the AA stacked zigzag edges.

The percentage of AB stacked zigzag edges increases from 17 to 32 %, whereas the percentage of AA stacked zigzag edges decreases from 17 to 13% after a 10-min annealing treatment, indicating that the AB stacked layer configuration is more stable than AA stacking. This observation is attributed to the fact that the ABAB stacked configuration is thermodynamically more stable than AA stacking¹² and is consistent with the Goma-Oberlin mechanism⁹.

4.3 Loop formation at the edges

Resistive Joule heating experiments on the as-produced graphitic nanoribbons (consciously minimizing the electron beam exposure before and after the constant bias voltage was applied) were carried out using the integrated scanning tunnel microscope (STM)-TEM system described in Section 4.1. Figure 4.15 a-d depicts TEM images of the nanoribbon edges after Joule heating. As we can see from these images, in the interior region of the ribbon material, the originally wavy fringes of the pristine material (see Figures 3.8 Pristine and 4.14a) are developed into close packed straight lines, indicating an increased crystallinity of the graphitic nanoribbon material, which is consistent with our observation of furnace heated samples at 1500 °C and 2800 °C (Figures 3.8 HT 1500 °C and 4.14 b and c).

Along the edges of the ribbon material, the open ends disappear, thus forming loops of different shapes (Figure 4.15a-d). The loops formed near the electrodes (Figure 4.15a) reveal a larger degree of curvature with a minimum of 2-3 layers contained within the loops, a result which is consistent with the furnace-heated samples¹³ in the temperature range between 2000 °C - 2500 °C.

The loops formed further away from the electrodes (Fig. 4.15 b-c) display a smaller curvature with more than 10 layers contained on average within a single loop.

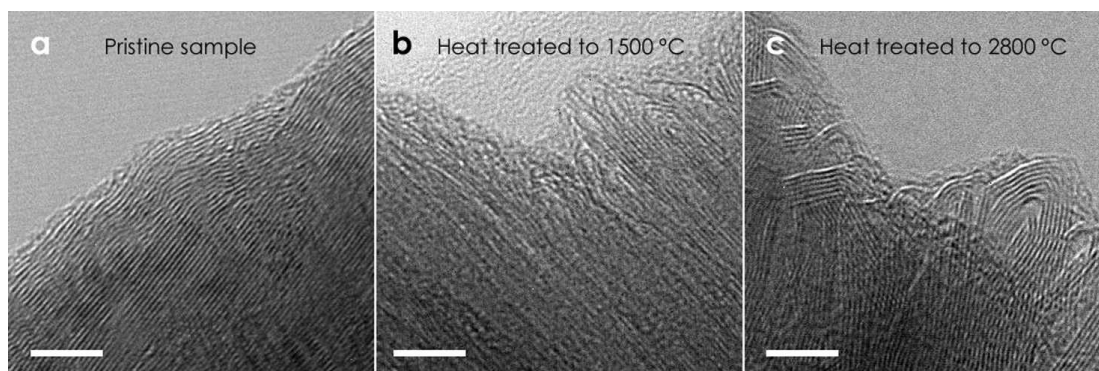


Figure 4.14 TEM micrographs of the edges of graphitic nanoribbons annealed in furnace: a) pristine sample, b) heat treated sample at 1500 °C, and c) heat treated sample at 2800 °C. The scale bars for the three images correspond to 5 nm.⁸

Finally, the loops formed near the central region of the ribbon material (Figure 4.15d) reveal larger loops and these even contain some facets (graphitization effect). Compared with the furnace heat treatment at 2800 °C (Figure 4.14c) where multiple loops (~6 layers) are formed, Joule heating (Figure 4.15c-d) results in loop formation with more layers (>10 layers), which might indicate that a higher local temperature is reached.

The effect of loop formation by Joule heating is primarily attributed to the high temperature achieved by resistive Joule heating.

We attribute the different shapes of the loops, that is, smaller loops (double or triple) near the electrodes (Figure 4.15a), and larger multiple loops and faceted formations near the central region of the ribbon (Figure 4.15d), to the larger temperature difference across the ribbon.

In our Joule heating experiments, the two electrodes serve as heat sinks.

Due to the achievement of good thermal conductivity near the electrodes, the temperature near the electrodes is much lower than that in the central region of the ribbon.

The formation of different loop structures along the nanoribbon is a direct evidence of temperature gradient.

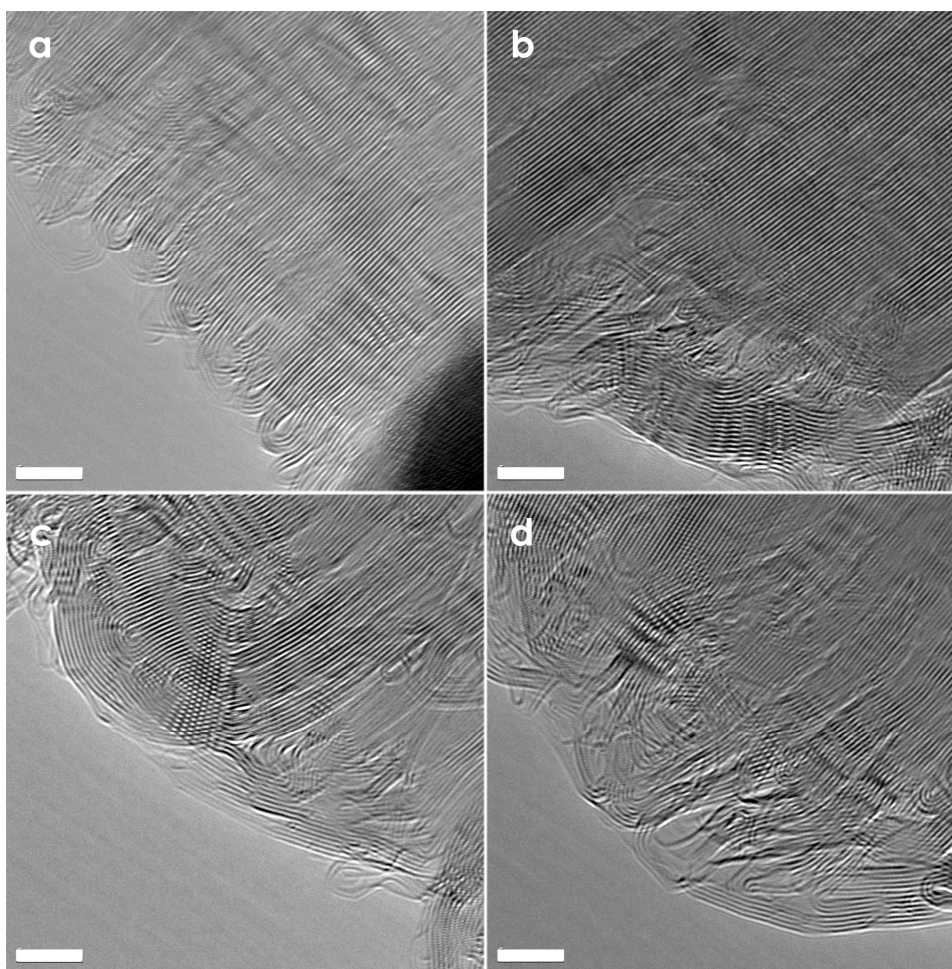


Figure 4.15 TEM images showing loop formation by Joule heating: a) near the electrode, b) and c) further away from the electrodes than in (a), and d) near the central region of the suspended graphitic nanoribbon material. (Scale bar is 5 nm)⁸.

This result is also consistent with the furnace heating experiments, which showed that different shapes of loops are formed at different annealing temperatures (Figure 3.8 and 4.14).

4.4 Estimation of the achieved temperatures

In order to estimate the temperature of the graphitic nanoribbons during the Joule heating experiment, Pt nanoparticles were deposited chemically on the as-

prepared nanoribbon surface (Figure 4.16a), and the structural changes in the Pt nanoparticles were monitored in-situ.

The Pt anchoring process consisted of sonicating for 15 minutes a mixture of graphitic nanoribbons (10 mg), plus 10 ml of N,N-dimethylformamide (Sigma-Aldrich®, 99%), (1,5-Cyclooctadiene) dimethylplatinum (II) (Sigma-Aldrich®, 97%) as a platinum source and polyvinylpyrrolidone (Sigma-Aldrich®, average mol wt. 10,000) as a passivating agent.

After sonication, the suspension was maintained under an Ar-H₂ (5% H₂) atmosphere to increase the reduction rate, and the suspension was subsequently placed in a glycerin bath at 110 °C for 40 minutes.

Next, the suspension was allowed to cool down to room temperature and the composite material (graphitic nanoribbons with Pt particles) was recovered by filtration. These graphitic nanoribbons exhibited platinum nanoparticles (with an average size of ~6 nm) anchored to their surface (see Figure 4.16a). Finally a thermal treatment was carried out at 350 °C under an Ar atmosphere for 15 minutes in order to eliminate any residues of organic material that could remain on the surface of the composite material.

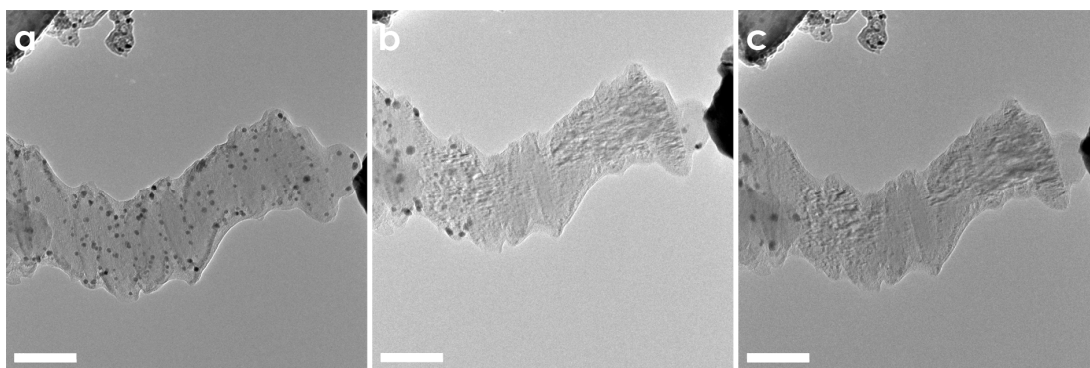


Figure 4.16 A sequence of TEM images showing Pt nanoparticles on the ribbon surface (a) before Joule heating, (b) after Joule heating for 11 minutes under a constant bias of ~2V, and (c) after Joule heating for another 4 minutes under a constant bias of ~2V. Here we see that the Pt particles melt and merge into bigger clusters (b), and start to evaporate from the central region of the ribbon (b), and eventually evaporate across almost the entire ribbon sample (c). (Scale bar is 100 nm).⁸

The modified nanoribbon material was then mounted on the Joule heating set-up. As we increased the applied voltage across the nanoribbons, the Pt nanoparticles near the central region of the ribbon started to melt and merge with other small neighboring Pt nanoparticles (some particles finally reached a diameter of 13 nm). Subsequently, and starting from the central region, the Pt nanoparticles evaporated, resulting in a clean surface (devoid of Pt nanoparticles) near the center of the ribbon sample (Figure 4.16b).

When a higher voltage is applied, additional Pt nanoparticles evaporate and eventually almost the entire ribbon is free of Pt nanoparticles (Figure 4.16c).

From these experiments, we confirmed that good thermal contacts are made near the electrodes, and that the two electrodes serve as heat sinks. The central region of the ribbon (Figure 4.14c) exhibits the highest temperature at a given applied voltage. Given the bulk Pt boiling point of 3827 °C, and that the boiling point of the Pt nanoparticles will have a lower boiling point than their bulk counterpart material due to size effects¹⁴, we estimate the temperature of the suspended ribbon sample under Joule heating to be above 2800 °C based on the loop formation morphology (comparison of Figures 3.8 HT 2800 °C and 4.14d).

4.5 Conclusions

As we have carefully described in this chapter, Joule heating experiments of graphitic nanoribbons lead either to sharp edge reconstruction or to loop termination of the edges, depending on the treatment given to the starting material.

When an as-produced nanoribbon is submitted to Joule heating (minimizing e-beam exposure), there is a significant rise in temperature.

This increase in temperature results in the annealing of defects, in-plane crystallization, and for the edges, the adjacent sheets (with parallel edges) find a more stable configuration forming loops, as seen in furnace heating¹³, and Iijima's recent work¹⁵ (see Figure 3.5d).

The configuration of the loops formed along the nanoribbon in this Joule heating experiment, gave irrefutable evidence of a temperature gradient, where the highest temperature is found in the center of the nanostructure.

When the same experiment is conducted in a nanoribbon specie that has been irradiated with the electron beam (for the purpose of imaging or to intentionally damage the structure), the results are completely different

Our experiments show that e-beam irradiation of the sample prior to Joule heating (between 10 min - 15 min) plays a decisive role in the reconstruction process.

This irradiation damages the structure, leading to the creation of vacancies and, most importantly, the sheets edges become irregular and unparallel probably due to the indistinctive evaporation of carbon atoms.

The irregularity of the edges does not favor the loop formation but the sharp edge reconstruction (primarily zigzag or armchair configurations) in the Joule heating process.

We have also carried out experiments of indirect temperature estimation during the Joule Heating treatments by depositing platinum nanoparticles (~6 nm in diameter) on the nanoribbons.

Our results showed that the temperatures achieved are high enough to melt and evaporate the Pt nanoparticles located in the middle of the nanoribbons.

We are certain that the achieved temperatures surpass the 2800 °C at the center of the studied nanostructure, consistent with Huang's estimations³⁻⁵ on experiments conducted in the same set-up using carbon nanotubes.

4.6 Related articles

- 1 . X. Jia, J. Campos-Delgado, E.E. Gracia-Espino, M. Hofmann, H. Muramatsu, Y.A. Kim, T. Hayashi, M. Endo, J. Kong, M. Terrones, M.S. Dresselhaus. *Loop formation in graphitic nanoribbon edges using furnace heating or Joule heating*. J. Vac. Sci. Technol. B 27, 4, Jul/Aug, 1996-2002, 2009
- 2 . X. Jia, M. Hofmann, V. Meunier, B.G. Sumpter, J. Campos-Delgado, J.M. Romo-Herrera, H. Son, Y.-P. Hsieh, A. Reina, J. Kong, M. Terrones, M.S. Dresselhaus. *Controlled formation of Sharp zigzag and armchair edges in graphitic nanoribbons*. Science 323, 1701-1705, 2009

4.7 References

- ¹ Yves Quéré. *Physics of Materials*. Gordon and Breach Science Publishers. Amsterdam, 1998
- ² P.G. Collins, M.S. Arnold, Ph. Avouris. *Engineering carbon nanotubes and nanotube circuits using electrical breakdown*. Science 292, 706-709, 2001
- ³ J.Y. Huang, S. Chen, S.H. Jo, Z. Wang, D.X. Han, G. Chen, M.S. Dresselhaus, Z.F. Ren. *Atomic-scale imaging of wall-by-wall breakdown and concurrent transport measurements in multiwall carbon nanotubes*. Phys. Rev. Lett. 94, 236802, 2005
- ⁴ J.Y. Huang, S. Chen, Z.Q. Wang, K. Kempa, Y.M. Wang, S.H. Jo, G. Chen, M.S. Dresselhaus, Z.F. Ren. *Superplastic carbon nanotubes*. Nature 439, 281 2006
- ⁵ J.Y. Huang, S. Chen, Z.F. Ren, G. Chen, M.S. Dresselhaus. *Real-time observation of tubule formation from amorphous carbon nanowires under high-bias Joule Heating*. Nano Letters 6, 8, 1699-1705, 2006
- ⁶ C. Jin, K. Suenaga, S. Iijima. *Vacancy migrations in carbon nanotubes*. Nanoletters 8, 4, 1127-1130, 2008.
- ⁷ X. Jia, M. Hofmann, V. Meunier, B.G. Sumpter, J. Campos-Delgado, J.M. Romo-Herrera, H. Son, Y.-P. Hsieh, A. Reina, J. Kong, M. Terrones, M.S. Dresselhaus. *Controlled formation of Sharp zigzag and armchair edges in graphitic nanoribbons*. Science 323, 1701-1705, 2009
- ⁸ X. Jia, J. Campos-Delgado, E.E. Gracia-Espino, M. Hofmann, H. Muramatsu, Y.A. Kim, T. Hayashi, M. Endo, J. Kong, M. Terrones, M.S. Dresselhaus. *Loop formation in graphitic nanoribbon edges using furnace heating or Joule heating*. J. Vac. Sci. Technol. B 27, 4, 1996-2002, 2009
- ⁹ B.T. Kelly. *Physics of Graphite*. Applied Science Publishers. London, 1981

-
- ¹⁰ J. Goma, M. Oberlin. *Graphitization of thin carbon films*. Thin Solid Films 65, 221-232, 1980
 - ¹¹ K. Nakada, M. Fujita, G. Dresselhaus, M.S. Dresselhaus. *Edge state in graphene ribbons: nanometer size effect and edge shape dependence*. Phys. Rev. B 54, 24, 17954-17961, 1996
 - ¹² S. Latil, V. Meunier, L. Henrard. *Massless fermions in multilayer graphitic systems with misoriented layers: Ab initio calculations and experimental fingerprints*. Phys. Rev. B 76, 201402, 2007
 - ¹³ J. Campos-Delgado, Y.A. Kim, T. Hayashi, A. Morelos-Gómez, M. Hofmann, H. Muramatsu, M. Endo, H. Terrones, R.D. Shull, M.S. Dresselhaus, M. Terrones. *Thermal stability studies of CVD-grown graphene nanoribbons: defect annealing and loop formation*. Chem. Phys. Lett. 469, 177-182, 2009
 - ¹⁴ M. Attarian Shandiz. *Effective coordination number model for the size dependency of physical properties of nanocrystals*. J. Phys.: Condens. Matter 20, 325237, (2008).
 - ¹⁵ Z. Liu, K. Suenaga, P.J.F. Harris, S. Iijima. *Open and closed edges of graphene layers*. Phys. Rev. Lett. 102, 015501, 2009

5. Conclusions and Perspectives

The synthesis of doped SWNTs and graphitic nanoribbons has been addressed using an aerosol-assisted CVD method.

Using the floating catalyst technique, ethanol-ferrocene solutions were prepared with precursor compounds of the doping element.

The synthesis of single-wall carbon nanotubes in sulphur, nitrogen, phosphorous and silicon environments was achieved via aerosol-assisted-CVD.

Precursors containing the target doping element were mixed in ethanol-ferrocene solutions at different concentrations, thiophene for sulphur incorporation, triphenylphosphine was used in the case of phosphorous, methoxytrimethylsilane was used as silicon precursor, and benzylamine and pyrazine were used as nitrogen precursors.

Electron microscopy of the samples as well as RBM Raman signal confirmed the presence of carbon nanotubes in the synthesized materials.

Electron microscopy analysis revealed that most of the materials consisted of doped SWNTs entangled with metallic nanoparticles, in the case of S and Si, interesting morphologies were formed, such as short bamboo-like MWNTs and Si nanorods with metallic tips, respectively.

In particular, the incorporation of sulphur promoted a very dense formation of by-products. The enhancement of the catalytic activity of iron by sulphur addition was confirmed through the copious presence of short, twisted bamboo-like MWNTs along with SWNTs. We believe that the modification of the experimental parameters (e.g. reduction of ferrocene concentration) could yield to the optimization of S-doped SWNTs.

The RBM analysis of our N- and P- doped materials showed that as the doping precursor was increased in the sprayer solution, narrower diameter tubes were

avored. The latter is consistent with theoretical calculations indicating that dopants of heavier elements embedded in the hexagonal carbon lattice are more energetically favored in narrower tubes exhibiting higher radii of curvature.

We have used the $I_{G'_{Def}}/I_{G'_{Pris}}$ relative intensities as a direct doping index for N, P and Si.

Our samples synthesized with sulphur could not be included in this analysis due to the poor quality of the recorded Raman spectra. Hence we do not have strong evidence for the effect of sulphur doping of SWNTs.

Si-doped samples showed low $I_{G'_{Def}}/I_{G'_{Pris}}$ relative intensity values which are directly related to the small amount of silicon atoms available per carbon atoms during the synthesis. Nitrogen doping is more effective when pyrazine is used (compared to benzylamine), and phosphorous doping is very effective even at low TPP concentrations.

Our Raman records show that increasing the precursor concentration leads to higher doping levels, increasing the $I_{G'_{Def}}/I_{G'_{Pris}}$ relative intensities, and that the frequency splitting of the G' band depends more on the doping element than the doping amount.

We are carrying out more synthesis experiments in order to have a higher number of samples per doping element, to be able to run Raman spectroscopy measurements and to elucidate the nature of the G' band splitting peculiarities observed in this work.

Our experiments for sulphur doping of SWNTs, led us to find a new route to efficiently produce graphitic nanoribbons at atmospheric pressure. The process is based on the pyrolytic decomposition at 950 °C of solutions of ferrocene-ethanol-thiophene at concentrations of 1.25 - 98.63 - 0.12 wt. %, respectively.

The morphology of the initial black powder that was collected consisted of ribbon-like structures of graphitic layers aligned parallel to the nanoribbon main axis with

average dimensions of several microns in length, widths ranging from 20-300 nm and thicknesses of 10-20 nm. It is interesting to note that the initial ribbons revealed both flat regions as well as rippled areas. The structure provides the material with a high proportion of edges, which are passivated by the presence of oxygen groups and sp^3 hybridization.

We have demonstrated that heat treatments up to 2800 °C of as-produced carbon nanoribbons anneal point defects and interstitials within individual graphene layers, thus leading to a material with a higher degree of crystallinity, in which the reactive edges of the ribbons are transformed into loops in a self-assembly process that can be strongly controlled by the variation of T_{HT} .

We have performed a detailed Resonance Raman study of heat treated nanoribbons on both bulk and individual nanoribbon samples. At the bulk level, we have confirmed a laser energy dependence of the D- and G'-bands frequency positions; and in these dependence values we found differences within the HT samples attributed to the annealing process.

The decrease of the I_D/I_G ratios and of the FWHM of the G band as the heat treatment temperature is increased suggests an increase in crystallinity of the hexagonal honeycomb lattice, a consequence of a partial graphitization process in which the stacking order could not be achieved completely possibly caused by the loop formation at the ribbon edges.

At the individual nanoribbon level, we have demonstrated that edge contributions to the Raman spectra intensify the signal of the D-band, indicating that symmetry-breaking elements such as sp^3 -like hybridized carbon atoms, structural defects and loops are present particularly in the vicinity of the edges.

However, the large number of loops present at the edges of all the ribbons is responsible for observing some residual D-band intensity. The general up-shift of the decomposition temperature in the TGA analysis also reveals a more stable and

less reactive material as T_{HT} increases in the range above which loop formation takes over.

The annealing processes that resulted from the Joule Heating experiments, proved to produce both, loops at the edges between parallel adjacent graphene sheets, and sharp zigzag or armchair edges when the sheets have been previously damaged by irradiation with an electron beam.

We have also carried out experiments of temperature estimation during the Joule Heating treatments. Our results showed that the temperatures achieved surpass the 2800 °C.

The work reported in this thesis has opened new lines of research related to the CVD synthesis of doped-SWNTs and graphitic nanoribbons.

Although a lot of experiments and characterization have been carried out, as this thesis proves, the scientific curiosity keeps motivating us to imagine, conceive and design new experiments in the search for new properties and new materials.

5. 1 Future work on doped-SWNTs

The optimization of sulphur-doping experiments is pending.

Although we were able to produce SWNTs in the presence of sulphur, the generation of by-products was greatly enhanced, and the SWNT Raman signal was screened in our measurements.

We believe that a lower concentration of ferrocene (~0.5 wt. % in contrast to the 1.25 wt. % used in our experiments reported in Chapter II), combined with the sulphur effect will provide enough catalytic action to synthesize SWNTs, while bigger Fe-S particles that promote the formation of short-twisted bamboo-like MWTNs will not be as numerous.

Also the use of Ar-H₂ instead of pure Ar as a carrier gas could inhibit the formation of amorphous carbon residues and extend the life-time of the catalyst particles.

The introduction of MTMS in the ethanol-ferrocene solutions to produce Si-doped SWNTs at concentrations above 0.1 wt. % triggered the formation of interesting by-products and decreased the SWNT formation. We believe that the modification of experimental parameters (increase of temperature and flow rate) will increase the velocity of the reaction and thus, promote the formation of SWNTs before the catalytic particles become de-activated by the formation of Fe-Si alloys.

Our results proved that nitrogen doping is more efficient when pyrazine is used as precursor (compared to benzylamine), evaluated through the $I_{G_{Def}}/I_{G_{Pris}}$ relative intensities. However, XPS measurements need to be performed in order to confirm this idea. Quantification of P-doping should also be addressed using this technique.

Testing the biocompatibility of cells with the different doped SWNTs is also pending.

5.2 Future work on graphitic nanoribbons

We have performed a lot of characterization on our graphitic nanoribbons. XPS measurements of pristine nanoribbons revealed a striking 1:1 ratio of sp²/sp³ hybridization.

Our observations lead us to think that this high proportion of sp³ hybridization can be attributed to the elevated proportion of edges present in the sample.

This possible explanation needs to be confirmed by XPS measurements of the heat treated nanoribbons. We expect to find a decreased signal of the sp³ hybridization due to the presence of loops which have passivated the edges in the annealed samples.

5.2 Future work on graphitic nanoribbons

So far we have worked with pristine and heat treated nanoribbons but we have not done chemistry-related experiments. We believe that due to the nature of our sample, we could chemically treat or exfoliate the sheets to end up with single-layer or double layer graphene nanoribbons.

Another line of research could be to try to reinforce materials with our nanoribbons, such as polymers and ceramics.

APPENDIX A

Carbon nanotubes synthesis methods and characterization tools

Synthesis methods

Arc discharge

An arc discharge is generated when a bias voltage is applied between two metallic electrodes, if the bias is sufficiently high to produce a discharge; the result is a small current flowing through the circuit (both electrodes and the existing gas in between).¹

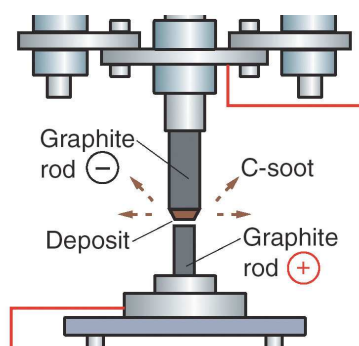


Figure A1 Diagram of an arc discharge chamber used to produce carbon nanotubes.²

The carbon arc provides a simple and traditional tool for generating the high temperatures needed for the vaporization of carbon atoms into a plasma (>3000 °C). Typical conditions for operating a carbon arc for the synthesis of carbon nanotubes include the use of carbon rod electrodes of 5-20 mm diameter, separated by ~1 mm with a voltage of 20-25 V across the electrodes and a DC electric current of 50-120 A flowing between the electrodes. The arc is typically operated in ~500 Torr He with a flow rate of 5-15 ml/s for cooling purposes. As the carbon nanotubes form, the length of the positive electrode (anode) decreases, and carbon material is deposited in the negative electrode (See Figure A1)³.

The first reports of single-wall carbon nanotube synthesis go back to 1993. Independently, two groups achieved their synthesis and both reports appeared one after the other in Nature magazine (Iijima, *et al.*⁴ and Bethune, *et al.*⁵, see Figure A2). Both experiments were carried out in an arc discharge chamber with graphite

electrodes (set-up used to produce C₆₀), with some differences in the experimental parameters.

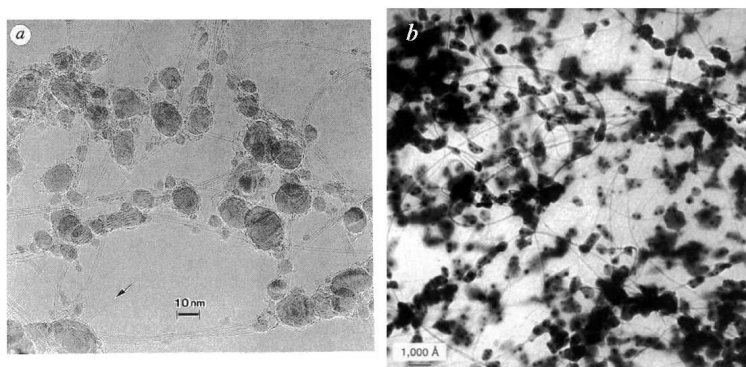


Figure A2 TEM images of arc-discharge produced SWNTs, a) extracted from Reference 4, b) extracted from reference 5

Catalysts used to prepare isolated single-wall carbon nanotubes (SWNTs) include transition metals such as Co, Ni, Fe and rare earths such as Y and Gd, while mixed catalysts such as Fe/Mi, Co/Ni and Co/Pt have been used to synthesize ropes of SWNTs. The iron or cobalt catalyst in the arc process forms both SWNTs and nanometer/size carbide particles surrounded by graphene layers, as well as metal clusters encapsulated within graphene layers. Thus purification is necessary to separate out a pure single-wall nanotube sample.⁴

Laser ablation

Using this technique the first report of SWNTs was published by Thess and co-workers⁶ in 1996. A Co-Ni/graphite composite laser vaporization target was used, consisting of 1.2 atom % Co-Ni alloy with equal amounts of Co and Ni added to the graphite. Two sequenced laser pulses were used to evaporate the target placed inside a furnace operated at 1200 °C. Flowing argon gas sweeps the entrained nanotubes from the high temperature zone to the water-cooled Cu collector downstream, just outside the furnace, Figure A3 shows a schematic representation of a typical laser ablation set-up.

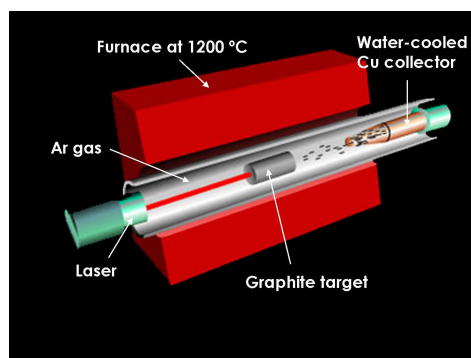


Figure A3 Diagram of the set-up used in the laser vaporization method to produce SWNTs⁷

The material thus produced appears as a mat of ropes 10-20 nm in diameter and up to 100 μm or more in length.

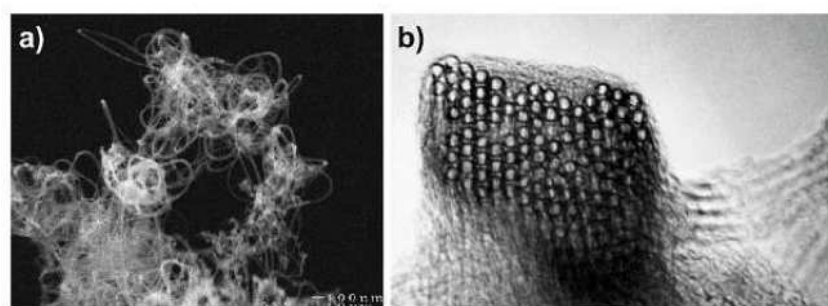


Figure A4 a) SEM micrograph of SWNT material showing a mat of tangled carbon fibers, b) TEM image of a single rope of SWNTs made up of ~ 100 SWNTs as it bends through the image plane of the microscope, showing uniform diameter and triangular packing of the tubes within the rope. (Extracted from Ref. 6)

Under TEM examination, each “rope” consisted primarily of a bundle of SWNTs aligned along a common axis, see Figure A4. The single-wall nanotubes are held together by weak van der Waals inter-nanotube bonds to form a two-dimensional triangular lattice with a lattice constant of 1.7 nm, and an inter-tube separation of 0.315 nm at closest approach within a rope.⁶

Chemical Vapor Deposition

Chemical vapor deposition (CVD) is a chemical process used to produce high-purity, high-performance solid materials. The process is often used in the

semiconductor industry to produce thin films. In a typical CVD process, the substrate is exposed to one or more volatile precursors, which react and/or decompose on the substrate surface to produce the desired deposit. Frequently, volatile by-products are also produced, which are removed by gas flow through the reaction chamber.

A number of forms of CVD are in wide use and are frequently referenced in the literature (atmospheric pressure CVD, low-pressure CVD, ultrahigh vacuum CVD, aerosol assisted CVD, direct liquid injection CVD, microwave plasma-assisted CVD, plasma-enhanced CVD, remote plasma-enhanced CVD).⁸

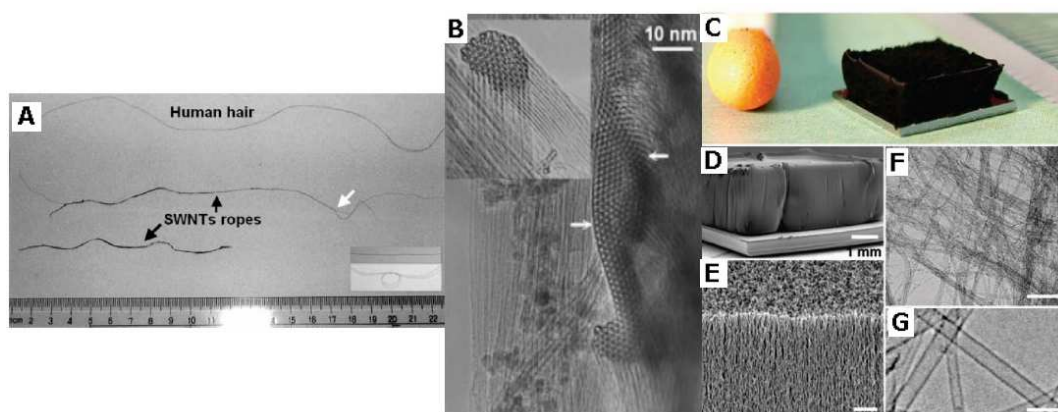


Figure A5 A) and B) extracted from reference 13, C) - G) extracted from reference 14. A) Optical image showing a human hair and two as-grown SWNT strands (indicated by black arrows), B) HRTEM image of a top view of a SWNT rope, white arrows indicate the arrangement of the triangle lattice of a large area in a SWNT strand. The inset shows a cross-sectional view of a polycrystalline bundle. C) SWNT forest grown with water-assisted CVD. Picture of a 2.5-mm-tall SWNTs forest on a silicon wafer. A matchstick on the left and a ruler with millimeter markings on the right is for size reference. D) SEM image of the same SWNT forest, E) SEM image of the SWNT forest ledge. Scale bar = 1 μm . F) Low resolution TEM image of the nanotubes. Scale bar = 100 nm . G) High-resolution TEM image of the SWNTs. Scale bar = 5 nm .

The synthesis of carbon nanotubes from the vapor phase utilizes equipment similar to that used for the preparation of vapor-grown carbon fibers, with the furnace temperature held at 1100 $^{\circ}\text{C}$ and using Fe catalyst particles, but using a low benzene gas pressure. A variety of other hydrocarbons, catalysts and catalyst

supports have been used successfully by various groups worldwide to synthesize carbon nanotubes.⁵

Other metallic catalysts used are Fe, Ni, Co and Pt. These are, either seeded as nanoparticles in substrates previous to the CVD reaction or as “floating” catalysts, where compounds containing the metals are mixed with the hydrocarbon at the time of reaction. The most common hydrocarbons used are methane, benzene, acetylene, toluene and ethylene. A typical CVD set-up contains a furnace, a reaction chamber, Ar or He flow to keep an inert atmosphere and carry the gases outside the furnace and the reaction zone.

The first report of CVD produced SWNTs was by H. Dai in 1996⁹ decomposing CO and using Mo as catalyst, and later works reported the use of different hydrocarbons (methane¹⁰, ethylene¹¹).

In 2002 Maruyama and co-workers¹² reported the synthesis of high purity SWNTs with this method. Using alcohol as the carbon source at low temperatures (700 °C - 800 °C, it is worth mentioning that low pressures are involved in the process) a product free of impurities as amorphous carbon, multi-walled carbon nanotubes, metal nanoparticles and carbon nanoparticles were completely suppressed by the etching effect of the –OH radical.

In the same year, Zhu et al¹³ achieved the synthesis of long strands of SWNTs (Figure 3A and B). Ferrocene and small concentrations of thiophene were mixed with n-hexane and the pyrolysis temperature was 1150 °C.

The so-called super-growth of SWNTs was achieved by Hata in 2004¹⁴, when SWNT forests of 2.5 mm were synthesized during 10 minutes of reaction (see Figure 3 C-G). This group added minute amounts of water vapor to the Ar or He flow. Catalysts were seeded in different substrates by sputtering and ethylene was used as a carbon source.

Characterization tools

The characterization of carbon nanotubes and carbon nanostructures aims to identify the morphology, dimensions, structure, chemical composition, physical,

chemical and electronic properties. Researchers in nanosciences use several techniques as standard characterization tools, some of which are described below.

Electron microscopy

Electron microscopy is a type of microscopy that uses a particle beam of highly energetic electrons to illuminate a specimen and create a highly-magnified image. Electron microscopes have much greater resolving power than light microscopes that use electromagnetic radiation and can obtain much higher magnifications of up to 2 million times. The greater resolution and magnification of the electron microscope is because the wavelength of an electron, its de Broglie wavelength, is much smaller than that of a photon of visible light.¹⁵

The basic steps involved in all electron microscopes are:

1. A stream of electrons is formed (by the electron source) and accelerated toward the specimen using a positive electrical potential
2. This stream is confined and focused using metal apertures and magnetic lenses into a thin, focused, monochromatic beam
3. This beam is focused onto the sample using a magnetic lens
4. Interactions occur inside the irradiated sample, affecting the electron beam

These interactions and effects are detected and transformed into an image.

The electron microscope uses electrostatic and electromagnetic lenses in forming the image by controlling the electron beam to focus it at a specific plane relative to the specimen.¹⁶

The Scanning Electron Microscope (SEM) is a type of electron microscope that images the sample by scanning it with a high-energy beam of electrons in a raster scan pattern. The electrons interact with the atoms that make up the sample producing signals that contain information about the sample's surface topography, composition and other properties such as electrical conductivity.

The types of signals produced by an SEM include secondary electrons, back scattered electrons, characteristic x-rays, light, specimen current and transmitted electrons. These types of signal all require specialized detectors that are not

usually all present on a single machine. For conventional imaging in the SEM, specimens must be electrically conductive, at least at the surface, and electrically grounded to prevent the accumulation of electrostatic charge at the surface.¹²

Transmission electron microscopy (TEM) is a microscopy technique whereby a beam of electrons is transmitted through an ultra thin specimen, interacting with the specimen as it passes through. An image is formed from the interaction of the electrons transmitted through the specimen; the image is magnified and focused onto an imaging device, such as a fluorescent screen, on a layer of photographic film, or to be detected by a sensor such as a CCD camera.¹²

X-ray diffraction

X-ray crystallography is a method of determining the arrangement of atoms with a crystal, in which a beam of X-rays strikes a crystal and scatters into many different directions.¹⁷

Bragg's law states that when X-rays hit an atom, they make the electronic cloud move as does any electromagnetic wave. The movement of these charges re-radiates waves with the same frequency; this phenomenon is known as Rayleigh scattering (or elastic scattering). These re-emitted wave fields interfere with each other either constructively or destructively (overlapping waves either add together to produce stronger peaks or subtract from each other to some degree), producing a diffraction pattern on a detector or film. The resulting wave interference pattern is the basis of diffraction analysis.

The interference is constructive when the phase shift is a multiple of 2π ; this condition can be expressed by Bragg's law

$$n\lambda = 2d \sin \theta$$

where n is an integer determined by the order given, λ is the wavelength of the X-rays, d is the spacing between the planes in the atomic lattice and θ is the angle between the incident ray and the scattering planes.

This technique has been used widely because it constitutes a non-destructive, accurate method to investigate the atoms arrangement of a particular sample through the diffraction pattern.

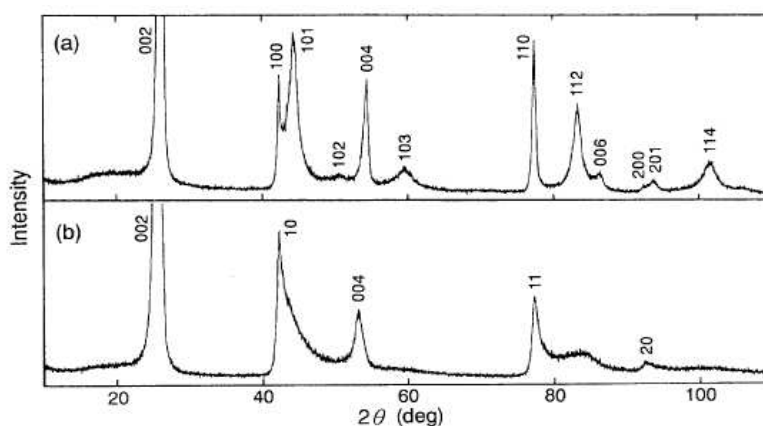


Figure A6 X-ray diffraction profiles of a) a graphite rod, and b) a core of a deposit grown after arc discharge. The core consists of bundles of carbon tubules and hollow nanoparticles¹⁸

Carbon materials are often characterized by X-ray diffraction since it is a sensitive tool to identify sp^2 and sp^3 hybridization through the (002) and (111) reflections, see Figure A6. Impurities and by-products like metal nanoparticles produced in the CVD synthesis of multi-wall carbon nanotubes are easily detected when strong iron carbides reflections are present in the spectra.

XPS

X-ray photoelectron spectroscopy (XPS) is a surface analytical technique, which is based upon the photoelectric effect. Each atom in the surface has core electrons with the characteristic binding energy, that is conceptually, not strictly, equal to the ionization energy of that electron. When an X-ray beam is directed to the sample surface, the energy of the X-ray photon is adsorbed completely by the core electron of an atom. If the photon energy, $h\nu$, is large enough, the core electron will then escape from the atom and be emitted from of the surface. The emitted electron with the kinetic energy of E_k is referred to as the photoelectron.

The binding energy is given by the relation

$$E_b = h\nu - E_k$$

The core electron of an element has a unique binding energy, which seems like a “fingerprint”. Thus almost all elements except for hydrogen and helium can be identified via measuring the binding energy of its core electron. Furthermore, the

binding energy of the core electron is very sensitive to the chemical environment of the element. The same atom when bonded to the different chemical species, leads to a change in the binding energy of its core electron. Since the number of photoelectrons of an element is dependent upon the atomic concentration of that element in the sample, XPS is used to not only identify the elements but also quantify the chemical composition.¹⁹

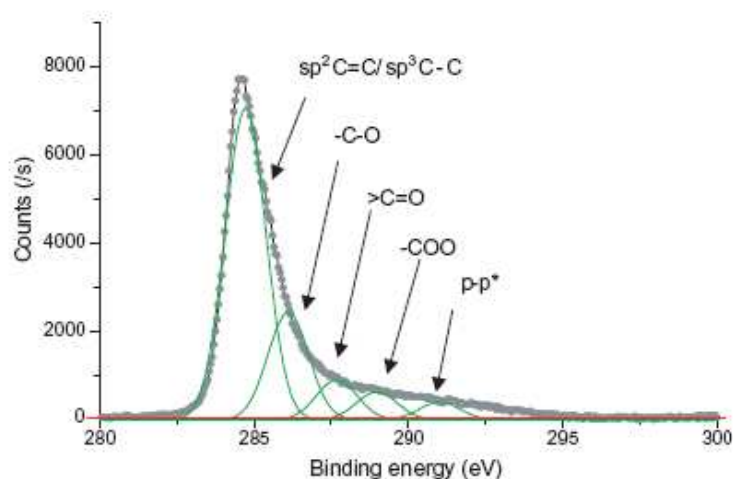


Figure A7 An example of XPS C1s peak deconvolution of MWNTs and the assigned bonds²⁰

Figure A7 is included to illustrate a representative XPS measurement from carbon nanostructures, it is extracted from Reference 19 where an XPS study on functionalized MWNTs was carried out. In the figure, the C1s signal is shown and a deconvolution depicts the signal contribution from the different types of bonds (i.e. C=C, C-C, C-O, C=O, COO).

EDX

EDX analysis stands for Energy Dispersive X-ray analysis. It is sometimes referred to also as EDS or EDAX analysis. It is a technique used for identifying the elemental composition of the specimen, or an area of interest thereof. The EDX analysis system works as an integrated feature of an electron microscope, and can not operate on its own without the latter.

During EDX analysis, the specimen is bombarded with an electron beam inside the scanning electron microscope. The bombarding electrons collide with the specimen

atoms' own electrons, knocking some of them off in the process. A position emptied by an ejected inner shell electron is eventually occupied by a higher-energy electron from an outer shell. To be able to do so, however, the transferring outer electron must give up some of its energy by emitting an X-ray.

The amount of energy released by the transferring electron depends on which shell it is transferring from, as well as which shell it is transferring to. Furthermore, the atom of every element releases X-rays with unique amounts of energy during the transferring process. Thus, by measuring the amounts of energy present in the X-rays being released by a specimen during electron beam bombardment, the identity of the atom from which the X-ray was emitted can be established.²¹

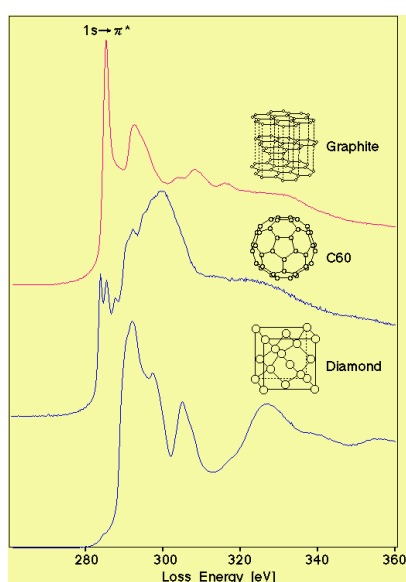


Figure A8 EELS spectra of carbon allotropes²²

EELS

When an electron beam is incident into specimen, a part of the electrons is inelastically scattered and loses a part of its energy. Elemental composition and the atomic bonding state can be determined by analyzing the energy with the spectroscope attached under the electron microscope (Electron Energy Loss Spectroscopy). Because the analyzing region can be selected from a part of the enlarged electron microscopic image, one can analyze a very small region. Moreover, by selecting electrons with a specific loss energy by a slit so as to image them, the element distribution in a specimen can be visualized (Elemental Mapping).

Diamond, graphite and fullerene are the materials that consist of only carbon, so that, all of these specimens have absorption peaks around 284 eV in EELS corresponding to the presence of carbon atoms. From the fine structure of the absorption peak, the difference in bonding state and local electronic state can be detected (see Figure A8). The sharp peak at the absorption edge corresponds to

the excitation of a carbon K-shell electron (1s electron) to an empty anti-bonding π -orbital. In the case of diamond this sharp peak is absent.²²

Raman spectroscopy

This technique is based on the Raman effect, which consists of the inelastic scattering of light by matter.

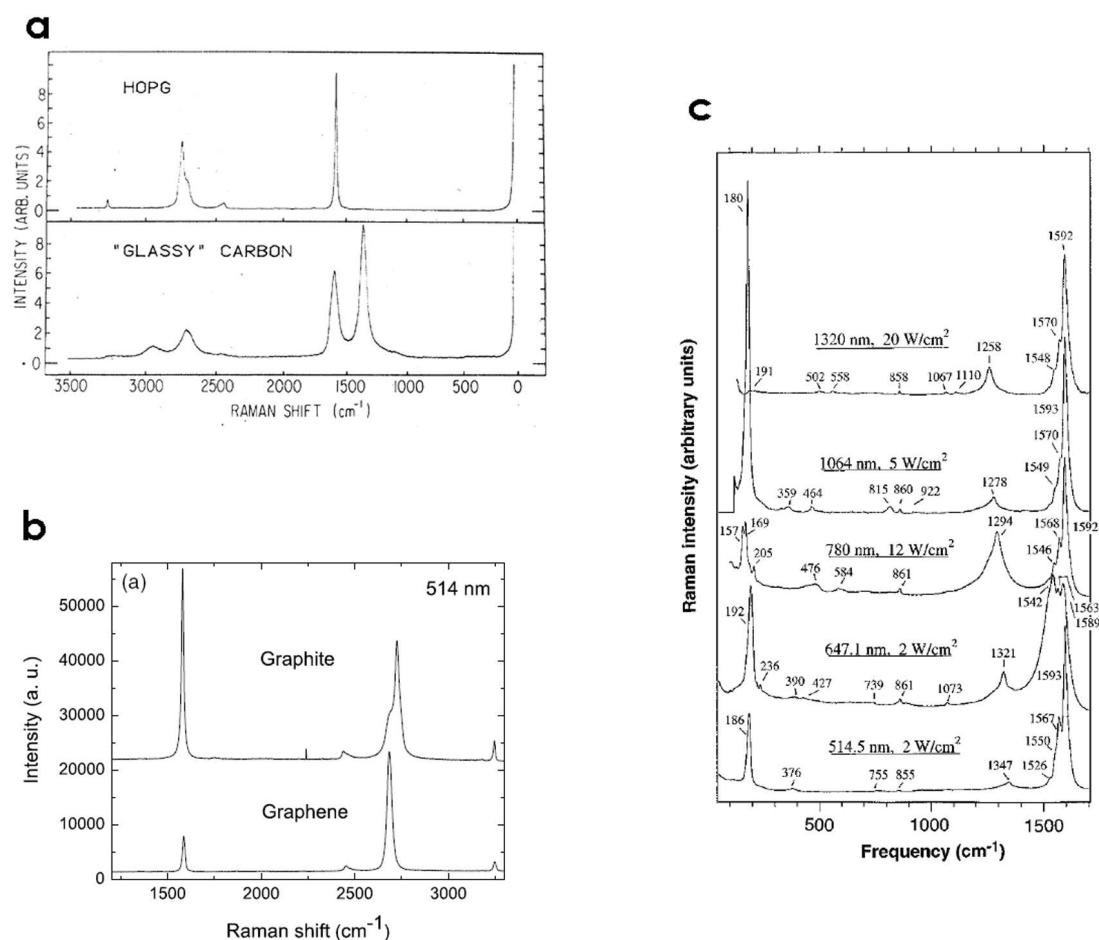


Figure **A9** Representative Raman spectra of carbon materials. a) First- and second-order Raman spectra of highly oriented pyrolytic graphite (HOPG) and "glassy" carbon, extracted from Ref. ²³, b) comparison of Raman spectra at 514 nm for bulk graphite and graphene. They are scaled to have similar height of the G' peak at $\sim 2700 \text{ cm}^{-1}$, extracted from Ref. ²⁴, c) Raman spectra for purified SWNTs excited at five different laser frequencies, extracted from Ref. ²⁵.

Raman analysis has proven to be a powerful, non-destructive technique, very helpful in the study of carbons. Its sensitivity to detect disorder, graphitization and stacking order of graphitic samples (see Figure A9a), plus the characteristic fingerprints of single-wall carbon nanotubes and graphene (see Figure A9 b and c), make of this technique a basic tool in the analysis of carbon materials.

Due to the importance of this characterization tool to analyze carbon structures, we have devoted a complete appendix to address the principles behind Raman scattering, focusing on carbon materials (see Appendix B).

References

- ¹ Translated from:
<http://bacterio.uc3m.es/docencia/profesores/herrerros/itts/ficheros/Arco.pdf>
- ² http://mrsec.wisc.edu/Edetc/SlideShow/slides/nanotubes/growing_arc.html
- ³ R. Saito, G. Dresselhaus, M.S. Dresselhaus. *Physical Properties of Carbon Nanotubes*. Chapter 5: Synthesis of Carbon Nanotubes. Imperial College Press. London, 1998
- ⁴ S. Iijima, T. Ichihashi. *Single-shell carbon nanotubes of 1-nm diameter*. *Nature* 363, 603-605, 1993
- ⁵ D.S. Bethune, C.H. Klang, M.S. de Vries, G. Gorman, R. Savoy, J. Vazquez, R. Beyers. *Cobalt-catalysed growth of carbon nanotubes with single-atomic-layer walls*. *Nature* 363, 605-607, 1993
- ⁶ A. Thess, R. Lee, P. Nikolaev, H. Dai, P. Petit, J. Robert, C. Xu, Y.H. Lee, S.G. Kim, A.G. Rinzler, D.T. Colbert, G.E. Scuseria, D. Tománek, J.E. Fischer, R.E. Smalley. *Crystalline ropes of metallic carbon nanotubes*. *Science* 273, 483-487, 1996
- ⁷ http://nano.mtu.edu/PulsedLaserVaporization_start.html
- ⁸ http://en.wikipedia.org/wiki/Chemical_vapor_deposition
- ⁹ H. Dai, A. G. Rinzler, P. Nikolaev, A. Thess, D. T. Colbert, R.E. Smalley. *Single-wall nanotubes produced by metal-catalyzed disproportionation of carbon monoxide*. *Chem. Phys. Lett.* 260, 471-475, 1996
- ¹⁰ J. Kong, A. M. Cassel, H. Dai. *Chemical vapor deposition of methane for single-walled carbon nanotubes*. *Chem. Phys. Lett.* 292, 567-574, 1998
- ¹¹ J. H. Hafner, M. J. Bronikowski, B.R. Azamian, P. Nikolaev, A. G. Rinzler, D. T. Colbert, K.A. Smith, R.E. Smalley. *Catalytic growth of single-wall carbon nanotubes from metal particles*. *Chem. Phys. Lett.* 296, 195-202, 1998

-
- ¹² S. Maruyama, R. Kojima, Y. Miyauchi, S. Chiashi, M. Kohno. *Low-temperature synthesis of high-purity single-walled carbon nanotubes from alcohol*. Chem. Phys. Lett. 360, 229-34, 2002
- ¹³ H.W. Zhu, C.L. Xu, D.H. Wu, B.Q. Wei, R. Vajtai, P.M. Ajayan. *Direct synthesis of long single-walled carbon nanotube strands*. Science 296, 884-886, 2002
- ¹⁴ K. Hata, D. N. Futaba, K. Mizuno, T. Namai, M. Yumura, S. Iijima. *Water-assisted highly efficient synthesis of impurity-free single-walled carbon nanotubes*. Science 306, 1362-1364, 2004
- ¹⁵ http://en.wikipedia.org/wiki/Electron_microscope
- ¹⁶ <http://www.unl.edu/CMRAcfem/em.htm>
- ¹⁷ http://en.wikipedia.org/wiki/X-ray_crystallography
- ¹⁸ Y. Saito, T. Yoshikawa, S. Bandow, M. Tomita, T. Hayashi. *Interlayer spacings in carbon nanotubes*. Phys. Rev. B 48, 3, 1907-1909, 1993
- ¹⁹ <http://www.nuance.northwestern.edu/KeckII/xps1.asp>
- ²⁰ T.I.T. Okpalugo, P. Papakonstantinou, H. Murphy, J. Mc Laughlin, N.M.D. Brown. *High resolution XPS characterization of chemical functionalized MWCNTs and SWCNTs*. Carbon 43, 153-161, 2005
- ²¹ <http://www.siliconfereast.com/edxwdx.htm>
- ²² <http://eels.kuicr.kyoto-u.ac.jp/eels.en.html>
- ²³ R. J. Nemanich, S.A. Solin. *First- and second-order Raman scattering from finite-size crystals of graphite*. Phys. Rev. B 20, 2, 1979
- ²⁴ A. C. Ferrari, J.C. Meyer, V. Scardaci, C. Casiraghi, M. Lazzeri, F. Mauri, S. Piscanec, D. Jiang, K.S. Novoselov, S. Roth, A.K. Geim. *Raman spectrum of graphene and graphene layers*. Phys. Rev. Lett. 97, 187401, 2006
- ²⁵ A. M. Rao, E. Richter, S. Bandow, B. Chase, P.C. Eklund, K.A. Williams, S. Fang, K.R. Subbaswamy, M. Menon, A. Thess, R.E. Smalley, G. Dresselhaus, M.S. Dresselhaus. *Diameter-selective Raman scattering from vibrational modes in carbon nanotubes*. Science 275, 187-191, 1997

APPENDIX B

Raman spectroscopy of sp^2 carbon materials

Raman scattering refers to the inelastic scattering of light. During a scattering event (1) an electron is excited from the valence energy band to the conduction energy band by absorbing a photon, (2) the excited electron is scattered by emitting (or absorbing) phonons, and (3) the electron relaxes to the valence band by emitting a photon. We generally observe Raman spectra for the scattered photon (light) whose energy is smaller by the phonon energy than that of the incident photon in accordance with the so-called Stokes process, discussed below. By measuring the intensity of the scattered light as a function of frequency downshift (losing energy) of the scattered light, which is what is plotted in Raman spectra, we obtain an accurate measure of the phonon frequencies of the material. Raman scattering can occur for phonon emission or by phonon absorption, and these two processes are called the Stokes process and anti-Stokes process, respectively¹.

The number of emitted phonons before relaxation of the lattice can be one, two, and so on, which we call, respectively, one-phonon, two-phonon and multi-phonon Raman processes. The order of a scattering event is defined as its number in the sequence of the total scattering events, including elastic scattering by an imperfection (such as a defect or edge) of the crystal. The lowest order process is the first-order Raman scattering process which gives Raman spectra involving one-phonon emission.¹

To run Raman spectroscopy experiments, lasers are used as a source of light, the excitation energy can be tuned by changing the laser wavelength in the visible range.

In order to interpret the Raman spectra of carbon nanostructures it is necessary to understand the phonon dispersion of graphene or 2D graphite.

The phonon dispersion relation shows interesting features in crystals with two or more atoms per primitive basis. For each polarization mode in a given propagation direction the dispersion relation ω versus K develops two kinds of branches, known

as the acoustical and optical branches. We have longitudinal LA and transverse acoustical TA modes, and longitudinal LO and transverse optical TO modes.

If there are p atoms in the primitive cell, there are $3p$ branches to the dispersion relation: 3 acoustical branches and $3p - 3$ optical branches.²

Since the unit cell of monolayer graphene contains two carbon atoms, A and B, there are six phonon dispersion bands, in which three are acoustic branches (A) and the other three are optic (O) phonon branches.³ For one acoustic branch (A) and one optic (O) phonon branch, the atomic vibrations are perpendicular to the graphene plane, and they correspond to the out-of-plane (o) phonon modes. For two acoustic and two optic phonon branches, the vibrations are in-plane (i). Traditionally, the directions of the vibrations are considered with respect to the direction of the nearest carbon-carbon atoms and, therefore, the phonon modes are classified as longitudinal (L) or transverse (T) according to vibrations parallel with or perpendicular to, respectively, the A-B carbon-carbon directions. Therefore, along the high symmetry ΓM and ΓK directions, the six phonon dispersion curves are assigned to LO, iTO, oTO, LA, iTA and oTA phonon modes, (see Figure B1).

Near the zone center (Γ point), the in-plane iTO and LO optic modes correspond to the vibrations of the sublattice A against the sublattice B, and these modes are degenerate at the Γ point. The phonon modes around the K point are especially important, since the D-band and the G'-band are related to phonon modes in the vicinity of the K point.

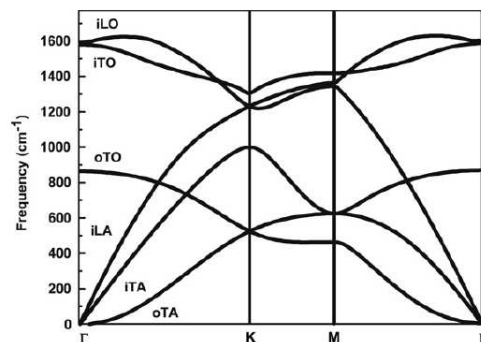


Figure B1 Calculated phonon dispersion relation of graphene showing the iLO, iTO, oTO, iLA, iTA and oTA phonon branches.³

To correctly describe the dispersion of the LO and iTO phonon branches near the Γ and K points, it is important to consider the renormalization of the phonon energies, associated with a process in which a phonon can create an electron-hole pair. This important electron-phonon coupling cannot be understood within the framework of the Born-Oppenheimer approximations, and gives rise to an interesting effect known as the Kohn anomaly.³ The Kohn anomaly is specially important for metallic SWNTs and for graphene and is responsible for a softening of certain Γ and K points phonons which increases the dispersive behavior of the D and G' bands, which will be explained in detail in future pages.

Resonance Raman spectroscopy

For a photo-excited electron, it will experience some processes before combining with a hole in the valence energy band. One of these processes is a scattering process by a quantized lattice vibration, known as a phonon with a phonon wave vector q . The electronic wave vector k is scattered to $k - q$ (phonon emission) or by $k + q$ (absorption), respectively, and the electron energy is shifted downward or upward by $\hbar\omega_q$, which is given by the observation of the scattered light and is known as the Stokes or anti-Stokes Raman shift. If a one-phonon scattering event occurs it is called a first-order Raman process. If either the initial k or the scattered $k \pm q$ electronic states is a real electronic state, the scattering amplitude is enhanced, and this is known as the incident or scattered resonance Raman process, respectively (see Figure B2, a1 and a2).

One important aspect of the Raman process in a crystal is that the photo-excited electron has to go back to its original k state to recombine with the hole at the k state. Because of this restriction, only a $q \sim 0$ phonon wave vector is selected in the first-order Raman process. Thus, in standard solid state textbooks, we see the statement that only the phonon energy at the center (Γ point) of the Brillouin zone, which is called the zone-center phonon mode, is observed by the Raman spectroscopy for solids.

We also expect second-order Raman processes to occur (Figure B2, c1 and c2), by emitting (1) two phonons with the same frequency or (2) two phonons with

different frequencies, which are called overtone or combination Raman modes, respectively. Another second-order process is given by one-phonon scattering and one elastic scattering process (Figure B2, b1-b4). Elastic scattering occurs in the presence of a defect in the crystal. In the latter case, the one phonon energy is observed in the second-order process. We refer to it as a one-phonon, second-order process.

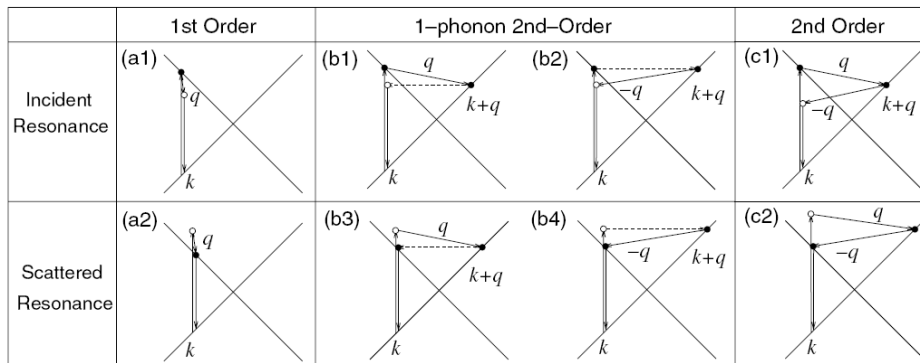


Figure B2 (a1, a2) First-order, (b1-b4) one-phonon second-order and (c1, c2) two-phonon second-order, resonance Raman spectral processes. Top panels: incident photon resonance; bottom panels: scattered resonance conditions. For one-phonon, second-order transitions, one of the two scattering events is elastic scattering (dashed line). Resonance points are shown as solid circles.⁴

In a second-order process, since an electron is represented by wave vectors q and $-q$, respectively, by scattering from and then by back-scattering to the original k state, non-zone-center phonon modes ($q \neq 0$) can be observed in the second-order Raman spectra. That is, (1) the electron is excited at k , (2) scattered to $k + q$, (3) scattered back to k and (4) recombined with a hole at k (see figure B2, b1-b4 and c1,c2). However, the probability for an electron to be scattered by a phonon is generally small, and thus the probability for the event occurring twice in a second-order process is much smaller. Thus, higher-order Raman processes in solids have not been considered much except for double resonance Raman spectroscopy.⁴

The double resonance effects occur when both the scattered intermediate state and the initial (or final) state are actual electronic states,⁵ and in this situation the Raman intensity can be increased by orders of magnitude.

In a double resonance process, the resonance enhancement results in Raman intensities that are almost of the same order as in the first-order resonance Raman spectra, and the corresponding q is selected by the resonance condition.⁴

The most outstanding features in the Raman spectra of carbon nanotubes are: the radial breathing mode (RBM) appearing in the range $100\text{ cm}^{-1} - 400\text{ cm}^{-1}$, that is a totally symmetric vibrational mode associated with the vibration of carbon atoms in a radial direction in relation to the nanotube axis; the G band appearing at $\sim 1580\text{ cm}^{-1}$ is associated with the highest-frequency optical phonon modes at the Γ -point in the Brillouin zone;⁴ and the G' band that appears in the high frequency region ($\sim 2700\text{ cm}^{-1}$), this band originates from a second-order process involving two iTO phonons near the K point³. In addition to these bands we see the defect-induced band (D band) at 1350 cm^{-1} when a certain amount of disorder or symmetry-breaking defects are present in the nanotube or in graphitic structures especially for spectra taken at the graphene edges. In some graphitic structures another defect-induced band appears at 1620 cm^{-1} . These bands originate from an intervalley and intravalley double resonance process, for the D and D' bands, respectively (see Figure B4).

First-order Raman scattering

In sp^2 -carbon materials the only first-order Raman feature that we observe is the G band; however, in the Raman spectra of single-wall carbon nanotubes we observe another first-order Raman mode at low frequencies, the so-called radial breathing mode. This feature is inherent to SWNTs and its observation in a Raman spectrum provides irrefutable evidence of the presence of SWNTs in the sample.

Radial Breathing Mode (RBM)

The RBM Raman features (appearing between $120\text{ cm}^{-1} < \omega_{\text{RBM}} < 250\text{ cm}^{-1}$ for SWNTs within $1\text{ nm} < d_t < 2\text{ nm}$) correspond to the atomic vibration of the C atoms in the radial direction, as if the tube were breathing (see Figure B3 a and c). These features are very useful for characterizing nanotube diameters through the relation

$\omega_{\text{RBM}} = 234 \text{ cm}^{-1}/d_t + 10 \text{ cm}^{-1}$ for samples in bundle. For $d_t < 1 \text{ nm}$, this relation is not expected to hold due to nanotube lattice distortions leading to a chirality dependence of ω_{RBM} . For large diameter tubes ($d_t > 2 \text{ nm}$) the intensity of the RBM feature is weak and is hardly observable⁶.

Because of its dependence on the nanotube diameter, the spectra of this mode are largely used for the characterization of the diameter distribution in a carbon-nanotube sample. The Raman intensity for the RBM is strongly enhanced when the incident or scattered light is in resonance with an excitonic transition. Thus, the Raman spectra of the RBMs for a sample composed of an ensemble of different nanotube chiralities is strongly dependent on E_{laser} because for each value of E_{laser} , the optical transition energies (E_{ii}) for different SWNTs are in resonance, and thus, the intensity of the RBM for these nanotubes is resonantly enhanced.⁷

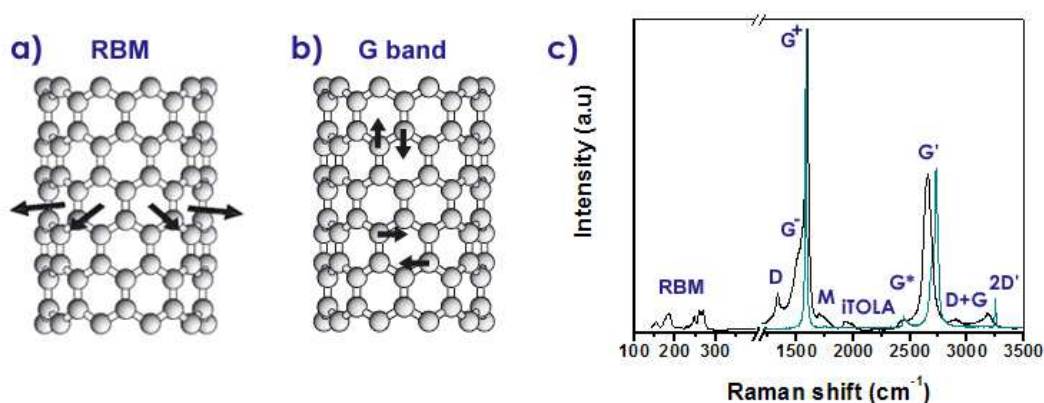


Figure B3 Schematic of the nanotube vibrations, a) RBM mode, and b) the G band atomic vibrations along the nanotube circumference and along the nanotube axis (extracted from reference 6) . c) Black line, Raman spectrum of a bundle of SWNTs synthesized by CVD⁸ with $E_{\text{laser}} = 2.41 \text{ eV}$, the labels name the first order, second order and combination Raman features; the light-blue line depicts the spectrum of HOPG for comparison.

At a fixed E_{laser} value, the RBM linewidth is found to increase with increasing nanotube diameter and as the energy difference $|E_{\text{laser}} - E_{ii}|$ between E_{laser} and the resonant interband energy E_{ii} increases. The smallest linewidths are, as expected, obtained under fully resonant conditions where $E_{\text{laser}} = E_{ii}$.⁹ If one interband energy E_{ii} and a nanotube diameter are specified, then its corresponding unique (n, m) indices can be identified from the Kataura plot (Figure 1.5).

It is clear that a single Raman measurement gives an idea of the tubes that are in resonance with that laser line, but does not give a complete characterization of the diameter distribution of the sample. However, by taking Raman spectra using many laser lines, a good characterization of the diameter distribution in the sample can be obtained.⁶

Tangential modes - G band

The graphite-like band (G-band) in carbon nanotubes is directly related to the G-band in graphite that is identified with an in-plane tangential optical phonon involving the stretching of the bond between the two atoms in the graphene unit cell, see Figure B3b. While the G-band in graphite exhibits a single Lorentzian feature at $\sim 1582\text{ cm}^{-1}$, the G-band of carbon nanotubes is composed of several peaks originating from the quantum confinement of the wavevector along the SWNT circumferential direction, and the folding of the graphite Brillouin zone into the SWNT Brillouin zone.⁷ The observation of these characteristic multi-peak features around $\sim 1580\text{ cm}^{-1}$ also provides a signature of carbon nanotubes. This multi-peak feature gives information about the metallic (or semiconducting) character of the SWNTs in resonance with a given laser line. The two most intense G peaks are labeled G^+ , for atomic displacements along the tube axis, and G^- , for modes with atomic displacement along the circumferential direction (see Figure B3 b and c), and the lowering of the frequency for the G^- mode is caused by the curvature of the nanotube which softens the tangential vibration in the circumferential direction.

The difference between the G band lineshape for semiconducting and metallic SWNTs is evident in the lineshape of the G^- feature, which is broadened for metallic SWNTs in comparison with the Lorentzian lineshape for semiconducting tubes, and this broadening is related to the presence of free electrons in nanotubes with metallic character.¹⁰

However, when multi-wall carbon nanotubes, HOPG, graphene or any other sp^2 carbon system is being analyzed, the G band shape is consistent with a single sharp Lorentzian peak, centered around 1580 cm^{-1} .^{11,12,13}

Second-order Raman scattering

In second-order double-resonance (DR) Raman processes for carbon materials, the electron (1) absorbs a photon at a k state, (2) scatters to $k + q$ states, (3) scatters back to a k state, and (4) emits a photon by recombining with a hole at a k state. The two scattering processes consist of either elastic scattering by defects of the crystal or inelastic scattering by emitting a phonon, as shown in Figure B2. Thus (1) one-elastic and one-inelastic scattering event and (2) two-inelastic scattering events are relevant to second-order Raman spectroscopy.¹

The most important second-order Raman features are the D band and the G' band, they originate from a second-order process involving two iTO phonons near the K point for the G' band and one iTO phonon and one defect in the case of the D band. Since the G' band is approximately twice the D band frequency ($\omega_{G'} \sim 2\omega_D$), some authors prefer to call it the 2D band. However this two-phonon band is allowed in the second-order Raman spectra of sp^2 -materials without any kind of disorder or defects (see spectrum of HOPG in Figure B3c). In order to prevent any misleading connection of this feature with disorder or defects, and to avoid confusion between the designation of "2D" to denote two dimensionality, we will use here the conventional notation of "G' band" as is used in the graphite and nanotube literature.³

In a DR Raman process, two resonance conditions for three intermediate states should be satisfied, in which the intermediate $k + q$ state is always a real electronic state and either the initial or the final k state is a real electronic state.¹ This DR mechanism is called an intervalley process because it connects points in circles around inequivalent K and K' points in the first Brillouin zone of graphene. On the other hand, the double resonance process responsible for the D' band is an intravalley process, since it connects two points belonging to the same circle around the K point (or the K' point), see Figure B4.³

Through history, the D and the G' bands have been very useful in the characterization of graphitic materials. For years the origin of the D band and its dispersion was not fully understood. In 1970 Tuinstra and Koenig¹¹ attributed the

presence of the D band in the Raman spectrum of graphite to particle size effects in which due to finite crystal size an A_{1g} mode of the lattice became active, they also correlated the intensity of this mode to the in-plane crystallite size L_a . The following experiments showed that the presence of the D band in the Raman spectra of sp^2 -carbon materials was also related to disorder features present in the material. In present days the ratio of the integrated areas (or the intensities) of the D band over the G band (I_D/I_G ratio) is a direct quantification of the degree of disorder or defects present in the material and is helpful in the determination in-plane crystallite sizes.¹⁴ Edges and crystal boundaries within a sample also contribute to the D band intensity.

In the Raman spectra of carbon materials, the presence of the G' band and most importantly of its doublet morphology represent a strong proof of 3D order or ABAB stacking achievement in a graphitic structure (see Figure 3.18b).

Recently the G' band has been used as a characterization tool of single-layer and few-layer graphene to determine the number of sheets, with ABAB... stacking, present in the sample.¹³

Disorder induced modes

In contrast to the first-order process, where only phonons near the Γ point of the Brillouin zone are probed, in second-order Raman spectra it is possible to probe features identified with phonons associated with interior points in the Brillouin zone, see Figure B4. This becomes possible because the selection rules for the second-order features are relaxed with respect to the first-order features.

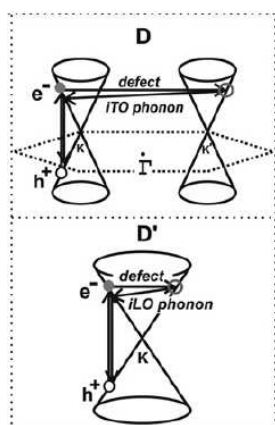
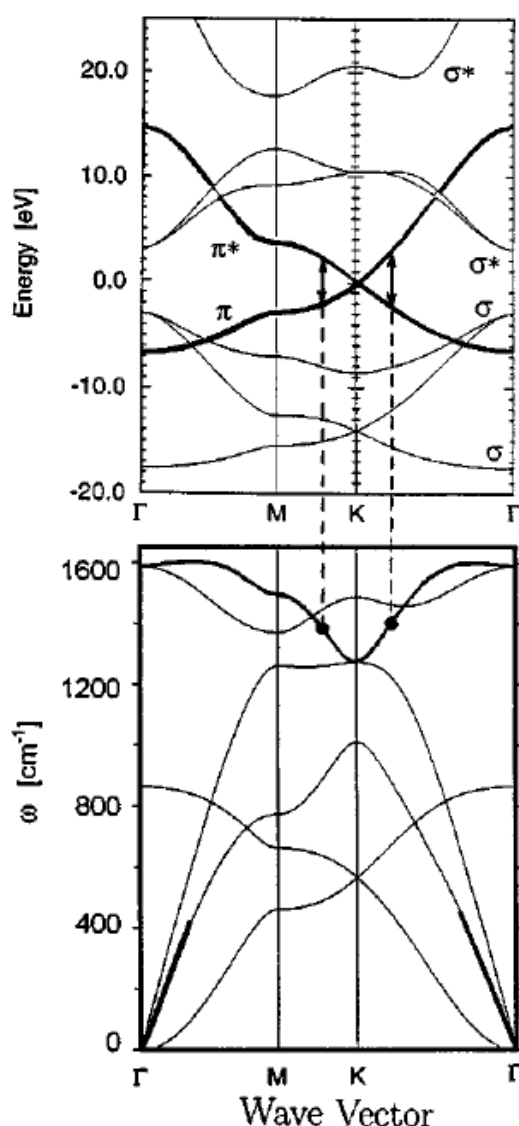


Figure B4 Top panel: one-phonon second-order double resonance process for the D band (intervalley process), and bottom panel: one-phonon second-order double resonance process for the D' band (intravalley process). (Adapted from reference 3)

The most common example of a second-order feature in the Raman spectra of carbon nanotubes is the disorder-induced band, observed in the $\sim 1300\text{-}1400\text{ cm}^{-1}$ range (D band). The D band common to all sp^2 -hybridized disordered carbon materials, originates from phonons close to the K point of the graphite Brillouin zone, and is activated by the presence of defects, such as impurities or missing atoms, finite-size effects and in the case of carbon nanotubes, molecules linked to



the nanotube sidewalls.⁷ Around 1620 cm^{-1} another disorder-induced feature appears and is called D' band and it originates from an intravalley second-order double-resonance process.

In carbon materials, there are several weak Raman signals whose phonon frequencies change with changing laser excitation energy which is called "dispersive" behavior.¹

Figure B5 Electronic energy bands of 2D graphite (top). Phonon dispersion curves of 2D graphite (bottom). Both the phonon branch that is strongly coupled to the electronic bands in the optical excitation, and the electronic bands near the Fermi level ($E = 0$) that are linear in k are indicated by heavy lines. (Extracted from reference ¹⁵)

A well-known dispersive spectral feature is the disorder-induced D band which appears at around 1350 cm^{-1} for laser excitation at about 2.41 eV . The D band frequency is highly dispersive and increases with increasing laser energy (E_{laser}) by

44-51 cm^{-1}/eV for various graphite and sp^2 materials and by 53 cm^{-1}/eV for SWNTs, respectively.⁵

Double resonance Raman theory, as discussed in this section, works well for explaining the dispersive phonon modes in which a non-zone-center ($q \neq 0$) phonon mode and a second-order Raman process are relevant to these weak spectral features.

As shown in Figure B5, the electronic structure of 2D graphite near the Fermi energy is linear in wave vector k , which is expressed by the crossed solid lines in Figure B2. The crossing point corresponds to the Fermi energy located at the K point of the Brillouin zone, this crossing point in graphene is called the Dirac point. When the laser energy E_{laser} increases, the resonance k vector for the electron moves away from the K point. In the DR process, the corresponding q vector for the phonon increases with increasing k , measured from the K point. Thus by changing the laser energy, we can observe the phonon energy $\hbar\omega(q)$ along the phonon dispersion relations (Figure B5). This effect is observed experimentally as a dispersion of the phonon energy as a function of excitation laser energy.¹

G' band

The most intense feature in the second-order Raman spectra of SWNTs (and of sp^2 -carbon materials) is the overtone of the D band feature discussed above, the so-called G' band, whose frequency is $2\omega_{\text{D}}$ (See Figure B3c) and its frequency dispersion is twice the D band frequency dispersion. While the D band originates from a double-resonance process involving a phonon and a defect, in the G' band, instead of a defect, another phonon is responsible for the momentum conservation in the double-resonance process, and the G' band is symmetry-allowed.

In systematic studies of heat treatments of carbonaceous materials^{16,17} it has been shown that in the graphitization process, when the ABAB stacking of graphitic layers is achieved, the G' peak evolves to a double-peak morphology. The explanation underlying the splitting observed on Figure 3.18b can be extracted from the article by Al-Jishi and Dresselhaus.¹⁸ These authors calculated the phonon density of states for hexagonal graphite. They found a number of peaks

relevant to this discussion, in particular, a strong one at 1345 cm^{-1} due to the extremum in the dispersion curves along the ΓK direction and a second line at 1365 cm^{-1} due to M point zone edge phonons. Thus, when the graphite is structurally well stacked (ordered), overtones could be expected in the second-order Raman spectrum at twice these frequencies. On the other hand, for the most poorly organized materials, one would expect these features to be less well defined and only an overtone corresponding to the average is observed experimentally. The appearance of the doublet in the ordered graphites is simply a manifestation of the sharpening of the features in the phonon DOS curves upon establishing good ABAB stacking.¹⁸

In 2008 Maciel and co-workers¹⁹ proved that the frequency of the G' band in the Raman scattering of SWNTs is dependent of the diameter distribution in the sample and that the observation of a second peak at lower frequencies is indeed not related to the diameter distribution of the samples, but there is actually a second feature at lower frequencies due to the presence of defects, which disappears under heat treatments. The observation of a two peaks G' band is due to the information coming from defect sites (G'_{Def}) and the higher frequency peak is associated with non-defective tube segments (G'_{Pris}).

The defect-induced nature of the G'_{Def} peak was demonstrated when the G' band spectra of pristine CVD-produced SWNTs was analyzed in the same work. The authors found that in the as-produced SWNTs, a weak G'_{Def} peak was observed, indicating the presence of defects in the structure (vacancies, structural heterogeneity). However, the G'_{Def} peak disappears after annealing of the sample at $200\text{ }^{\circ}\text{C}$, $400\text{ }^{\circ}\text{C}$ and $600\text{ }^{\circ}\text{C}$ in argon flow (see Figure B6). The defects were present only before the annealing step. These results are congruent with previously reported works on the low crystallinity (quality) of CVD-grown SWNTs when compared to their arc-discharge-produced counterpart. Properly heat treated CVD-grown SWNTs do not have disorder induced features.

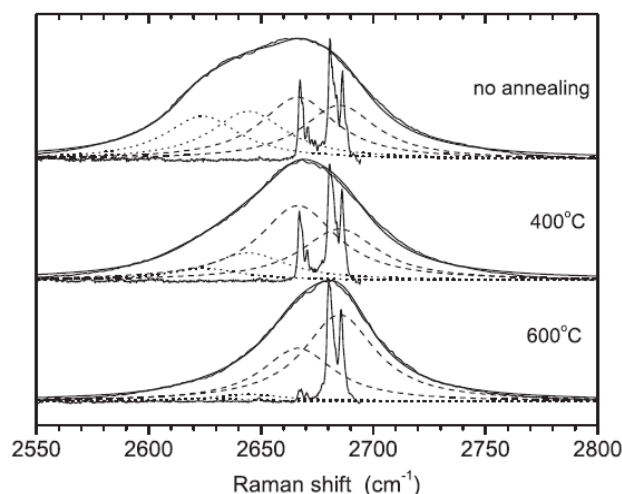


Figure B6 The G' features of CVD-SWNT samples before and after heat treatment at 400 °C and at 600 °C ($E_{\text{laser}}=2.41$ eV). The spectra were deconvoluted into four Lorentzian (dashed lines for G'_{Pris} and dotted lines for G'_{Def}) the corresponding RBM spectra were superimposed to the G' band (extracted from Reference 19).

Later in 2008, the same group proved that the G' band can be used to probe defects in the lattice of single-wall carbon nanotubes²⁰. These defects can be vacancies, Stone-Wales transformations or even foreign atoms inserted in the honeycomb structure (i.e. doping). Figure B7a is extracted from that report, where we see a plot of the G' band for different sp^2 carbon materials. The three upper curves are for single-wall carbon nanotubes prepared by different methods. The upper plot is for heat-treated undoped SWNTs and shows a single G'_P peak (P for pristine) centered at $\omega_{G'_P} = 2,676 \text{ cm}^{-1}$.

On doping, a new G' peak is observed at a lower/higher frequency for n/p doping. The spectra of graphene, highly oriented pyrolytic graphite (HOPG) and amorphous carbon are also presented in Figure B7a to clearly show that the new peak cannot be related to other forms of sp^2 carbon. This new peak, from now on is called the G'_{Def} peak (Def for 'defect'), and appears in the G' spectra of doped SWNTs.

The presence of a negatively charged defect provokes the renormalization effect on the local electronic and vibration structure, as discussed below.

The second-order symmetry-allowed G' Raman scattering process occurs in all sp^2 carbon materials, involving in-plane transversal optical (iTO) phonons near the K point in the hexagonal Brillouin zone, selected by the double-resonance process.

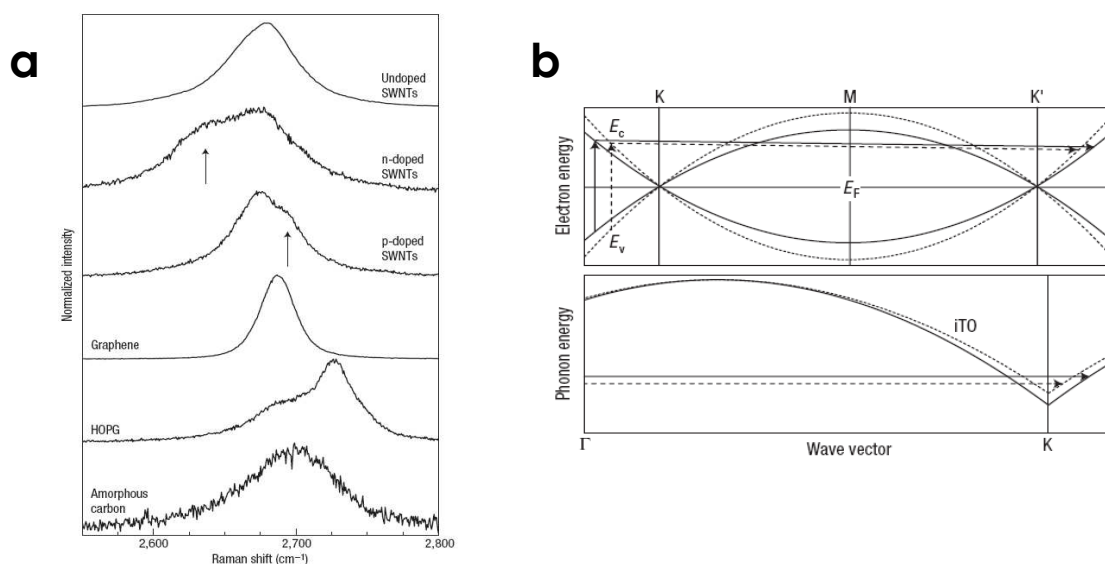


Figure B7 a) The G' band in different sp^2 carbon materials measured at room temperature with Elaser = 2.41 eV (514 nm). The arrows point to defect-induced peaks in the G' for doped SWNTs. The p/n doping comes from substitutional boron/nitrogen atoms, the nearest neighbours of carbon in the periodic table. The spectra of graphene, HOPG and amorphous carbon are shown for comparison. b) Schematic model showing the renormalization of electron and phonon energies near a negatively charged defect. The upper panel shows the dispersion of the π and π^* electrons along the KMK' direction in the hexagonal Brillouin zone, near the Fermi level (E_F). The lower panel shows the iTO phonon branch along the ΓK direction. The arrows in the upper panel indicate electron transitions by photon absorption (vertical arrows) and phonon scattering (nearly horizontal arrows). The arrows in the lower panel indicate the energies for the same phonons when they are scattering electrons in the upper panel. Dashed lines represent the renormalized structure near the defect sites. (Adapted from Reference 20)

An excited electron with wave vector k resonantly selects a phonon with wave vector $q \sim -2k$. This relation between k and q , together with the Dirac-Fermion behavior for high-speed electrons and the Kohn anomaly for phonons, makes the G' band strongly dependent on the particular electronic structure, thereby providing information about the electronic structure.

The excited electron with wave vector of modulus k is generated by resonance with the excitation laser

$$E_{\text{laser}} = E_c - E_v = 2\hbar v_F k \approx \hbar v_F q$$

where the subscripts v and c stand for the valence and conduction bands, respectively. Changing E_{laser} changes k linearly, and consequently q , so that the electronic structure can be probed using phonon measurements.

A schematic model showing the defect-induced renormalization of the electron and phonon energies and its influence on the double-resonance G' scattering process is shown in Figure B7b.

The two resonant processes, the optical absorption and the scattering of the excited electron by a phonon, are presented by the vertical and nearly horizontal arrows, respectively. The G'_{Pris} follows the unperturbed process (solid lines), whereas the G'_{Def} follows the process where electron and phonon energies are renormalized (dashed lines).²⁰

In the second-order Raman spectra of graphite and SWNTs there are other features worth mentioning. For example the M and iTOLA features²¹ located at 1700 cm^{-1} and 1950 cm^{-1} , respectively (iTOLA is the combination mode of the iTOLA + LA processes); the G^* band²² at 2450 cm^{-1} ; the D+G band (combination mode of the phonons that originate the D and G bands) located at 2900 cm^{-1} ; the 2G band (overtone of the G band) at 3180 cm^{-1} , and the 2D' band^{12,23} (overtone of the D' band) found at 3250 cm^{-1} .

References

- ¹ M.S. Dresselhaus, G. Dresselhaus, R. Saito, A. Jorio. *Raman spectroscopy of carbon nanotubes*. Physics Reports 409, 47, 2005
- ² C. Kittel. *Introduction to Solid State Physics*. 7th edition. Wiley. USA, 1996
- ³ L.M. Malard, M.A. Pimenta, G. Dresselhaus, M.S. Dresselhaus. *Raman spectroscopy in graphene*. Physics Reports 473, 51-87, 2009
- ⁴ R. Saito, A. Grüneis, G.G. Samsonidze, V.W. Brar, G. Dresselhaus, M.S. Dresselhaus, A. Jorio, L.G. Cançado, C. Fantini, M.A. Pimenta, A.G. Souza Filho. *Double resonance Raman spectroscopy of single-wall carbon nanotubes*. New Journal of Physics 5, 157.1-157.15, 2003
- ⁵ R. Saito, A. Jorio, A.G. Souza Filho, G. Dresselhaus, M.S. Dresselhaus, M.A. Pimenta. *Probing phonon dispersion relations of graphite by double resonance Raman scattering*. Phys. Rev. Lett. 88, 027401, 2002
- ⁶ A. Jorio, M.A. Pimenta, A.G. Souza-Filho, R. Saito, G. Dresselhaus, M.S. Dresselhaus. *Characterizing carbon nanotube samples with resonance Raman scattering*. New Journal of Physics 5, 139.1-139.17, 2003
- ⁷ A. Jorio, M.S. Dresselhaus, G. Dresselhaus, Editors. *Carbon nanotubes. Advanced topics in the synthesis, structure, properties and applications*. Springer. Berlin, Heidelberg, 2008
- ⁸ F. Lupo, J.A. Rodríguez-Manzo, A. Zamudio, A.E. Elías, Y.A. Kim, T. Hayashi, M. Muramatsu, R. Kamalakaran, H. Terrones, M. Endo, M. Rühle, M. Terrones. *Pyrolytic synthesis of long strands of large diameter single-walled carbon nanotubes at atmospheric pressure in the absence of sulphur and hydrogen*. Chem. Phys. Lett. 410, 384-390, 2005
- ⁹ M.S. Dresselhaus, G. Dresselhaus, A. Jorio, A.G. Souza-Filho, R. Saito. *Raman spectroscopy on isolated single wall carbon nanotubes*. Carbon 40, 2043-2061, 2002

-
- ¹⁰ A. Jorio, R. Saito, G. Dresselhaus, M.S. Dresselhaus. *Determination of nanotubes properties by Raman spectroscopy*. Phil. Trans. R. Soc. Lond. A 362, 2311-2336, 2004
- ¹¹ F. Tuinstra, J.L. Koenig. *Raman spectrum of graphite*. The Journal of Chemical Physics 53, 3, 1970. R. J. Nemanich, S.A. Solin. *First- and second-order Raman scattering from finite-size crystals of graphite*. Phys. Rev. B 20, 2, 1979
- ¹² Y. Kawashima, G. Katagiri. *Fundamentals, overtones, and combinations in the Raman spectrum of graphite*. Phys. Rev. B 52, 14, 1995
- ¹³ A.C. Ferrari, J.C. Meyer, V. Scardaci, C. Casiraghi, M. Lazzeri, F. Mauri, S. Piscanec, D. Jiang, K.S. Novoselov, S. Roth, A.K. Geim. *Raman spectrum of graphene and graphene layers*. Phys. Rev. Lett. 97, 187401, 2006
- ¹⁴ L.G. Cançado, K. Takai, T. Enoki, M. Endo, Y.A. Kim, H. Mizusaki, A. Jorio, L.N. Coelho, R. Magalhães-Paniago, M.A. Pimenta. *General equation for the determination of the crystallite size L_a of nanographite by Raman spectroscopy*. Appl. Phys. Lett. 88, 163106, 2006
- ¹⁵ M.J. Matthews, M.A. Pimenta, G. Dresselhaus, M.S. Dresselhaus, M. Endo. *Origin of dispersive effects of the Raman D band in carbon materials*. Phys. Rev. B 59, 10, R6585-R6588, 1999
- ¹⁶ P. Lespade, A. Marchand, M. Couzi, F. Cruege. *Characterisation de matériaux carbonés par microspectrométrie Raman*. Carbon 22, 4/5, 375-385, 1984
- ¹⁷ H. Wilhelm, M. Lelaurain, E. McRae, B. Humbert. *Raman spectroscopic studies on well-defined carbonaceous materials of strong two-dimensional character*. Journal of Applied Physics 84, 12, 6552-6558, 1998
- ¹⁸ R. Al-Jishi, G. Dresselhaus. *Lattice-dynamical model for graphite*. Phys. Rev. B 26, 8, 4514-4522, 1982
- ¹⁹ I.O. Maciel, M.A. Pimenta, M. Terrones, H. Terrones, J. Campos-Delgado, A. Jorio. *The two peaks G' band in carbon nanotubes*. Phys. Stat. Sol. (b) 245, 10, 2197-2200, 2008

-
- ²⁰ I.O. Maciel, N. Anderson, M.A. Pimenta, A. Hartschuh, H. Quian, M. Terrones, H. Terrones, J. Campos-Delgado, A.M. Rao, L. Novotny, A. Jorio. *Electron and phonon renormalization near charged defects in carbon nanotubes*. Nature Materials 7, 878-883, 2008
- ²¹ V.W. Brar, G.G. Samsonidze, M.S. Dresselhaus, G. Dresselhaus, R. Saito, A.K. Swan, M.S. Ünlü, B.B. Goldberg, A.G. Souza-Filho, A. Jorio. *Second-order harmonic and combination modes in graphite, single-wall carbon nanotube bundles, and isolated single-wall carbon nanotubes*. Phys. Rev. B 66, 155418, 2002
- ²² T. Shimada, T. Sugai, C. Fantini, M. Souza, L.G. Cançado, A. Jorio, M.A. Pimenta, R. Saito, A. Grüneis, G. Dresselhaus, M.S. Dresselhaus, Y. Ohno, T. Mizutani, H. Shinohara. *Origin of the 2450 cm⁻¹ Raman bands in HOPG, single-wall and double-wall carbon nanotubes*. Carbon 43, 1049-1054, 2005
- ²³ S.D.M. Brown, P. Corio, A. Marucci, M.A. Pimenta, M.S. Dresselhaus. *Second-order resonant Raman spectra of single-walled carbon nanotubes*. Phys. Rev. B 61, 11, 7734, 2000